Design and characterization of functional nanomaterials on surfaces

Tesis doctoral presentada por

Ana Sánchez Grande

Facultad de Ciencias

Departamento de Física de la Materia Condensada

Director de tesis:

Prof. David Écija

Madrid, Septiembre de 2020

UNIVERSIDAD AUTONOMA DE MADRID

instituto iMdea nanociencia

EXCELENCIA SEVERO OCHOA

Abstract

The urgent need for developing new strategies to afford the increasing energy demand remains a challenge for many research fields, such as material science or energy engineering. In this respect, the field of nanoscience has emerged as a powerful field towards the design of functional nanomaterials, synthesized from both organic and inorganic materials. This new scientific discipline has led to the design of novel materials and opened up new avenues for traditional compounds. For instance, transition metal oxides have been proposed as promising catalysts in the oxygen evolution reaction for water splitting, of crucial relevance in clean energy. Additionally, the development of organic electronics, focused on the study of the electronic properties of carbon-based materials, plays an important role in the synthesis and transformation of traditional electronics by designing low-cost, flexible and sustainable electronic devices.

In this thesis, we have grown and studied different nanomaterials on metallic surfaces related to energy efficiency, targeting to achieve global sustainability. First, we have studied the catalytic activity of CoO at the atomic scale towards the water splitting reaction. We have grown single bilayer CoO nanoislands, where the co-existence of two distinct phases has been observed. Such polymorphism has been rationalized due to the distinct lattice parameter and the registry with the substrate which induces the modification of its electronic properties, reactivity and, hence, of its catalytic activity. In addition, we have shown the capability to tune the phase by an electric field. Second, we have described the on-surface synthesis of new π-conjugated polymers with important applications in organic electronics. An innovative strategy towards the synthesis of low band gap π-conjugated polymers formed by acene or periacene units has been developed, which allows the control of their electronic structure, resonance form and topological quantum class by tuning the repeating unit size.

Our results shed light into the atomistic adsorption and dissociation of water on a CoO model catalyst. Furthermore, we introduced pathways for controlling the electronic properties and quantum topological class of one dimensional polymers on metallic surfaces.

Resumen

Durante las últimas décadas se ha producido un importante incremento en la demanda energética por parte de la sociedad, lo que ha llevado a que muchas investigaciones de diferentes campos se hayan centrado en el desarrollo de nuevas estrategias para satisfacer dicha demanda, como puede ser la ciencia de materiales o la ingeniería de la energía. En este sentido, el campo de la nanociencia ha adquirido un papel clave para el diseño de nuevos materiales funcionales. Por ejemplo, la viabilidad de los óxidos de metales de transición como catalizadores en la reacción de evolución de oxígeno para la división del agua ha sido extensamente estudiada, debido a su importancia en energías limpias. Por otra parte, el desarrollo de la electrónica orgánica, la cual se centra en el estudio de las propiedades electrónicas de los materiales formados a base de carbono, desempeña un papel clave en la síntesis y transformación de la electrónica tradicional hacia el diseño de dispositivos electrónicos de bajo coste, flexibles y sostenibles.

En esta tesis, hemos preparado y estudiado diferentes nanomateriales en superficies metálicas con posibles aplicaciones energéticas hacia la sostenibilidad global. Estos nanomateriales han sido caracterizados mediante microscopía de efecto túnel y microscopía de fuerza atómica sin contacto. En primer lugar, hemos estudiado la actividad catalítica del CoO a escala atómica hacia la división del agua. Observamos la existencia de diferentes fases de CoO con distintos parámetros de red y diferente registro con el sustrato, lo que induce la modificación de sus propiedades electrónicas, reactividad y, por lo tanto, de su actividad catalítica. Además, se muestra la transformación de dichas fases tras aplicar un campe eléctrico externo. Por otro lado, se propone la síntesis en superficie de nuevos polímeros π-conjugados con importantes aplicaciones en electrónica orgánica. Hemos desarrollado una nueva estrategia para sintetizar polímeros π-conjugados de bajo intervalo de banda prohibida formados por unidades de acenos o periacenos, a través de los cuales podemos controlar su estructura electrónica, forma resonante y fase topológica ajustando el tamaño de la unidad repetitiva.

Nuestros resultados contribuyen al estudio del CoO como catalizador, mostrando la adsorción y disociación del agua a nivel atómico. Además, se proponen caminos de reacción para controlar las propiedades electrónicas y la naturaleza topológica de polímeros π-conjugados unidimensionales en superficies metálicas.

Acknowledgments

Esta tesis ha sido posible gracias al esfuerzo de mucha gente que ha contribuido profesionalmente, personalmente o de ambas maneras. En primer lugar, quería agradecer y dedicar la tesis a todo el mundo que ha estado siempre ahí. Además, hay algunas personas a las que quiero agradecer especialmente su dedicación y esfuerzo.

En primer lugar, a mi director de tesis David Écija a quien le debo todo relacionado con la tesis. Sólo tengo palabras de agradecimiento por todo: por creer en mí, darme la oportunidad de realizar una tesis, trabajar diariamente sin descanso en ella, luchar y preocuparse por mí tanto personal como profesionalmente y siempre apoyarme. Gracias por hacerla posible ¡¡LO HEMOS CONSEGUIDO!!

En el día a día hay personas que han sido clave para poder haber llegado a este punto, por ello quiero agradecer especialmente al Dr. Koen Lauwaet, Dr. José Ignacio Urgel y Dr. Borja Cirera. Gracias por todo lo que me habéis enseñado y por todos los buenos momentos que he pasado con los tres, haciendo que el día a día en el laboratorio haya sido increíble y aún mejor fuera de él. He sido muy afortunada de poder compartir todo este tiempo con vosotros y espero poder seguir haciéndolo por muchos años más.

No puedo pasar por alto la contribución del Dr. Roberto Otero, Dr. José María Gallego y Prof. Rodolfo Miranda. Habéis contribuido al desarrollo de esta tesis con vuestros consejos, dedicación y tiempo. Ha sido una suerte poder encontrarme en el camino a personas tan apasionadas por la ciencia que consiguen transmitirla e inspirar a las nuevas generaciones.

Una parte importante de esta tesis es gracias al Prof. Pavel Jelínek y a todo su grupo, gracias por todo el esfuerzo, discusiones y dar sentido a nuestras medidas experimentales. También gracias por darme la oportunidad de realizar una estancia en Olomouc junto al Dr. Bruno de la Torre y por todo lo que aprendí durante ese tiempo. También quiero agradecer al Dr. Oliver Gröning y a la Prof. Nuria López por todo vuestro trabajo y lo que he podido aprender de vosotros. Gracias a todas las personas del A-LEAF y especialmente al coordinador J. R. Galán, junto a los cuales he compartido este camino

y de las que he aprendido mucho. Y por supuesto, gracias al grupo del Prof. Nazario Martín, cuyos esfuerzos y estrategias para diseñar nuevas moléculas han sido clave para el desarrollo de esta tesis. Finalmente, al Dr. Jonathan Rodríguez-Fernández por toda su contribución científica y su amistad.

No puedo olvidar a mis compañeros de superficies de IMDEA. He tenido la suerte de tener el mejor compañero de laboratorio que se puede tener, Dani, gracias por tu ayuda incondicional, apoyarme, escucharme y siempre estar ahí. Pablo, Cosme, Fabián, Manuela, Alberto, Juanje, Óscar, Sofía, Cristina y Kalyan gracias por el día a día y todas las risas que me habéis regalado. Por supuesto, aquí os incluyo a vosotras, Alba y Adriana, que habéis contribuido como las que más tanto a las risas como a encontrar un "estado zen" cuando nos hacía falta.

Hay una larga lista de personas que, aunque científicamente no hayan contribuido, han sido clave para que siguiera adelante. Quiero agradecer a todos mis amigos que me hacéis la vida tan feliz y divertida. A mis amigos del colegio que siempre habéis estado ahí, especialmente a Isa, María, Cris, Luis, Micky y Tito. A mis amigos más molestones que habéis dado sentido a todo en cada viaje, picnic, cumpleaños, casas rurales… A los friendes porque sois familia. Mis compañeras de aventuras: Anita, María, Iciar, Anuka y Maite. A Marta, Susa y Mónica con quienes la vida me juntó porque tenía que ser así. A mis compañeros de la universidad y mis queridas Natalia y Marina, quienes son las principales responsables de que yo haya llegado hasta aquí. Y a mis amigos de la tuna porque por muchas vueltas que de la vida siempre estaréis ahí.

Finalmente, quiero agradecer especialmente a mi familia. A todos mis primos y mis tíos que siempre me han apoyado, especialmente a mi padrino y a la Minina. A mi familia postiza: Jota, Mabel, Charo, Luis y María. A Cris Paniagua porque gracias a ella soy como soy. A Manu por todo su apoyo. A Cos por aguantarme siempre todo, ayudarme y hacerme sentir feliz. A mi Kubita por estar siempre conmigo. Y finalmente, a las personas más importantes y a quienes les debo todo en esta vida: a mis padres y a mi hermana. Esta tesis y todo lo que tengo en esta vida es gracias a vosotros, GRACIAS.

List of abbreviations

AM-AFM. Amplitude Modulation Atomic Force Microscopy

BLA. Bond Length Alternation

CB. Conduction Band

CT. Cold Trap

DFT. Density Functional Theory

DOS. Density of States

FFT. Fast Fourier Transform

FM-AFM. Frequency Modulation Atomic Force Microscopy

HOMO. Highest Occupied Molecular Orbital

IMDEA. Instituto Madrileño de Estudios Avanzados

LCAO. Linear Combination of Atomic Orbitals

LDOS. Local Density of States

LEED. Low Energy Electron Diffraction

LM. Lateral Manipulation

LT. Low Temperature

LUMO. Lowest Unoccupied Molecular Orbital

NADPH. Nicotinamide Adenine Dinucleotide Phosphate Hydrogenated

nc-AFM. Non-Contact Atomic Force Microscopy

OMBE. Organic Molecular Beam Epitaxy

PA. Polyacetylene

PAH. Polycyclic Aromatic Hydrocarbons

PEC. Photoelectrochemical Cell

QCM. Quartz Crystal Microbalance

QMS. Quadruple Mass Spectrometer

RT. Room Temperature

SPM. Scanning Probe Microscopy

STM. Scanning Tunneling Microscopy

STS. Scanning Tunneling Spectroscopy

TB. Tight Binding

TMP. Turbo Molecular Pump

TPD. Thermal Programmed Desorption

TSP. Titanium Sublimation Pump

UHV. Ultra-High Vacuum

VB. Valence Band

VM. Vertical Manipulation

XPS. X-ray Photoelectron Spectroscopy

List of Figures

List of tables

Contents

1. Introduction

This chapter introduces the development of nanoscience and nanotechnology during the last decades and its contribution to surface science, mainly through the invention of the STM. Next, we present some of the main motivations that have led us to carry out this work. Finally, the chapter concludes with an outline of the thesis.

1.1 Nanotechnology

Nowadays, nanotechnology has become one of the main fields under study and development. The concept of nanotechnology was introduced in 1959 by Richard Feynman (awarded with the Nobel Prize in physics in 1965) in his talk 'There is plenty of room at the bottom".[1] He suggested the possibility of manipulating and controlling the matter at the smallest scale, being the very first time that smallest scale meant nanoscale (Figure 1.1 shows a schematic comparison from centimeter to nanometer). This new concept was presented to the American Physical Society and it redirected much of the scientific progress of the century, being considered nowadays as the next technological revolution. Now in 2020, many of the predictions proposed by Feynman have been realized, such as the resolution enhancement in electron microscopies,[2] the atom manipulation by scanning probe microscopies[3] or the on-going miniaturization of devices.[4]

Nanotechnology opened plenty of new applications in the fields of physics, chemistry, and materials science, due to the strong, and sometimes unexpected, variation of the physico-chemical properties of materials when reducing their dimensionality.[5] The understanding and rationalization of all these new physical and chemical phenomena led to the emergence of nanoscience. Nanomaterials are defined as materials exhibiting at least one dimension in the range of 1-100 nm. The higher surface area of nanomaterials compared to their bulk counterparts, together with the quantum effects arising in such dimensions, are the keys of their chemical reactivity, optical, electronic and magnetic properties.

One of the main tools employed in nanoscience are Scanning Probe Microscopes. This family of microscopes was triggered by the invention of the Scanning Tunneling Microscopy (Nobel Prize in Physics in 1986 to Gerd Binning and Heinrich Rohrer).[6] Only a few years after, the Atomic Force Microscope was also developed.[7] Both microscopes steered different techniques of measurement that can be classified under the general scope of Scanning Probe Microscopy (SPM). In its easiest implementation, a scanning probe microscope acts based on the physical movement of a small probe above a surface while monitoring and recording specific magnitudes between the probe and the surface (e.g.: current, magnetism, electric field, light, elasticity, force interactions…), which finally are plotted in a XY graph displaying the recorded magnitude.

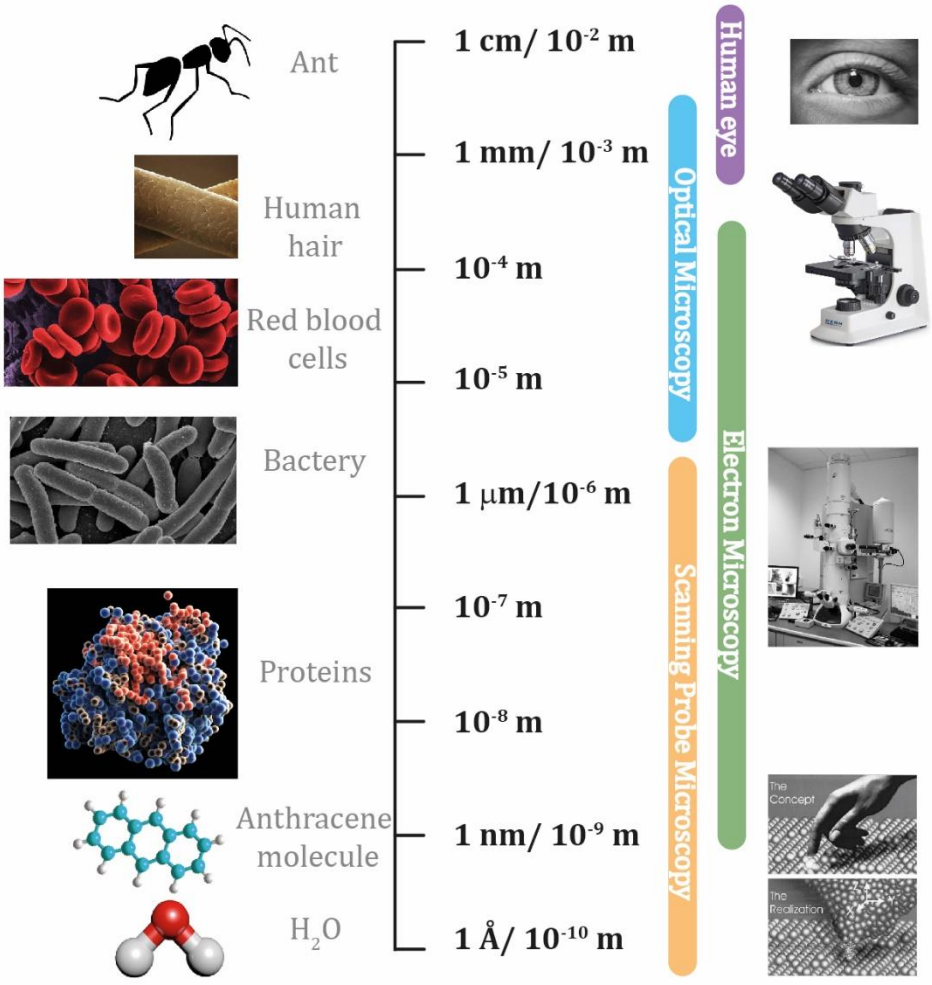

Figure 1-1. Comparison of scales: from centimeter to nanometer

SPM techniques have importantly contributed to the development of nanotechnology and nanoscience.[8] Scanning probe microscopes allow us to image and manipulate matter at the atomic scale. In addition, they help us to inspect fundamental properties of metals, semiconductors or insulators down to the atomic scale and revealing information about the magnetic, electronic or mechanical properties.

As a result of fundamental nanoscience investigations of the past XX century, now real applications are arising related to nanotechnology with promising benefits to the society. We can find applications in different sectors, such as information technology, energy, medicine or environmental science. For instance, some examples of the impact of nanotechnology in modern society are: the miniaturization of transistors with a size below 10 nm,[9] the diagnostics and treatments of diseases[10] and more efficiently fuel production employing better catalysts.[11]

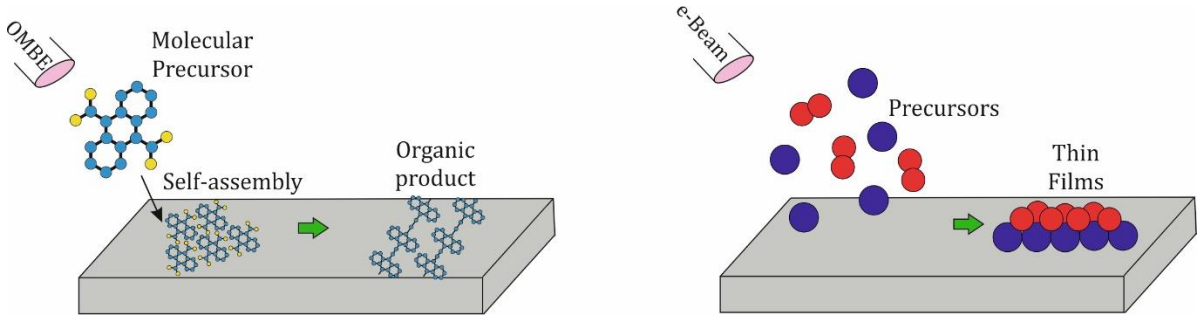

Figure 1-2. Schematic representation of bottom up techniques employed

In this work, we have employed surface science and scanning probe techniques to develop and study new nanomaterials from a fundamental point of view, in order to contribute to the nanoscience research with promising applications in different sectors related to energy efficiency, targeting to achieve global sustainability. In particular, we have focused our attention on two distinct nanomaterials: i) All-carbon-based nanostructures and ii) Cobalt-based oxides nanoislands. Such nanomaterials show different applications towards organic electronics and water splitting catalysis, respectively; however both of them present a common target: global sustainability. To synthesize such nanomaterials on surfaces, bottom-up strategies were followed including on-surface synthesis and physical vapor deposition (see Figure 1.2), both under ultra-high vacuum (UHV) conditions.

1.2 Global sustainability

Nowadays, the increasing energy demand leads us to reconsider the main energy sources to supply the requirements of the society.[12] We can find two main challenges towards the design of more efficient energies: the wise use of finite energy sources and the development of new abundant and biodegradable energy sources. Hereby, we have studied two different types of nanomaterials: cobalt oxides and all-carbon-based polymer nanostructures.

On one hand, cobalt is a 3d transition metal with plenty of applications, mainly towards energy storage. For several years, commercial Lithium ion batteries (2019 Nobel Prize in chemistry) included a positive electrode based on cobalt ($LiCoO_2$-CoO_2 corresponding to discharged and charged electrode, respectively).[13] Certainly, Cobalt shows a wide range of applications: forming superalloys with unique properties, batteries, catalysis, magnets, etc. However, this element also has some intrinsic limitations. Cobalt is of relatively low abundancy in earth crust and, in addition, the largest cobalt reserves are concentrated among a few countries (near half of the reserves are located at DR Congo). This irregular distribution together with its importance towards a sustainable planet lead us to consider the cobalt a critical raw material.[14] Although cobalt is a bio essential element for bacteria, plants, animals and humans (acquired by humans as Vitamin B12), it presents some health and environment hazards. Therefore, an entire industry towards the analysis of cobalt risk, engineer and administrative controls have been implemented. In conclusion, cobalt is essential for sustainable developments, and its unique properties make this element indispensable for many process.[15] Therefore, a strategical use of such material has to be taken into account. Cobalt based oxides have been proposed as anode to be integrated in a Photoelectrocatalytic device (PEC) in order to generate and store energy from abundant and clean sources (solar energy and water).[16] Here, we will study model systems of such cobalt oxide catalyst providing atomistic insights.

On the other hand, organic electronics has emerged as a field of materials science with revolutionary applications in electronic technology.[17] Organic electronics studies the synthesis and characterization of carbon-based nanostructures with tunable electronic and optical properties. These new materials possess desirable properties and are eco-

alternatives to inorganic semiconductor materials. Inorganic semiconductors imply an expensive and long waste management and some of them are scarce. Under this scenario, organic electronics is a powerful substitute that provides more sustainable materials, expanding the functionalities of the inorganic compounds and reducing considerably the costs. In addition, they offer the feasibility of being flexible and biocompatible materials. Organic electronics includes the development of carbon-based semiconductors and metallic structures with important applications in optoelectronics, transistors or organic solar cells.[18] In this technological world, the design of eco-materials, that also implies cost reductions, contributes to a sustainable world based on cleaner and sustainable energies. Following this paradigm, here we have developed a strategical on-surface design of one-dimensional π-conjugated polymers featuring unique electronic properties, including nearly-metallic electronic structure, topological non-trivial insulators, and diradical molecular wires, with promising applications in organic electronics.

1.3 Thesis outline

The organization of the thesis is as follows:

Chapter **2** introduces a theoretical background needed for the understanding of the thesis. First, fundamental concepts related to surface science are provided. Second, the SSH model together with its extension towards π-conjugated polymers based on acenes and periacenes are explained. Finally, the theoretical background behind the employed experimental techniques is given.

In chapter **3** a more detailed explanation about the methods and the experimental set-up is provided. Some common components of the four employed ultra-high vacuum systems are introduced. Then, the recently mounted low temperature nc-AFM/STM located at IMDEA is described, together with its supporting instruments.

Chapter **4** presents the study of the structure of CoO at the atomic scale and its properties towards catalyzing the water splitting reaction. We observe two distinct phases for the CoO nanoislands on Au(111): the moiré pattern region (incommensurate area) and the β-region (commensurate area). Both of them exhibit a hexagonal lattice, but the interatomic distances from β-region are shorter. Remarkably, we demonstrate that this

slight compression alters completely the electronic structure of the oxide, and hence, its reactivity. Notably, tip-induced voltage pulses irreversible transform moiré regions into β-phases.

Chapter **5** introduces a new strategy towards the synthesis of π-conjugated polymers by thermal activation at 500 K of molecular precursors functionalized with CBr_2 functional groups. First, we present the on-surface synthesis of polymers based on acene or periacene units. Interestingly, these polymers show a competition between resonance forms, namely between the ethynylene-bridged aromatic structure and the cumulene-linked quinoid form. We observe that the increasing of the number of fused rings at the acene or periacene unit leads to an increase of the quinoid/cumulene character of the π-conjugated polymer. Importantly, we show that these two resonance forms are associated to distinct topological quantum phases that implies a topological transition taking place from a trivial to a non-trivial phase as a function of the size of the central unit. Finally, further thermal annealing at 600 K of the cumulene-bridged bisanthene polymer produces the ladderization of the polymer forming pentalene-bridged polymers that includes the formation of non-benzenoid rings.

Chapter **6** and **7** include the main conclusions of the results and the perspectives related to the experiments performed, in English and Spanish, respectively.

Finally, chapter **8** presents the list of publications and chapter **9** includes the references to the information sources.

2. Theoretical fundamentals

This chapter introduces fundamental concepts for the understanding of the experiments carried out in this thesis. The introduction begins with the description of basic concepts of solid-state physics that will appear throughout the thesis. The second section deals with a theoretical approach to the Su, Schrieffer and Heeger (SSH) model[19] and its extension towards the π-conjugated polymers synthesized in this work.[20] The chapter concludes with an explanation of the Scanning Probe Microscopy (SPM),[21,22] followed by a more detailed explanation of the main techniques employed: Scanning Tunneling Microscopy (STM)[6] and non-contact Atomic Force microscopy (nc-AFM).[7,23]

2.1 Generic concepts on solid-state physics

Solid-state physics studies crystal solids in which large number of atoms are chemically bound. Therefore, understanding the behavior of electrons in an atom is crucial to describe the properties of 3D crystals. The simplest model to describe the distribution of electrons on a 1D system is "The Free-Electron Gas".[24,25] This model assumes that electrons are confined in a 1D infinite square-well potential and occupy each N states known as orbitals. Furthermore, this model neglects any interaction between electrons and assumes the Pauli Exclusion Principle. This principle demands that there cannot be two electrons with the same quantum numbers per state and it is crucial to define the electronic occupation of the orbitals. The wave function of an electron in an orbital n and its eigenenergy are defined by Equations 2.1 and 2.2, respectively:

$$\psi_n = A \sin\left(\frac{2\pi}{\lambda_n} x\right) \tag{2.1}$$

$$\varepsilon_n = \frac{\hbar^2}{2m}\left(\frac{n\pi}{L}\right)^2 \tag{2.2}$$

Where λ_n is the wavelength of the electron ($\lambda_n = 2L/n$), L the length of the square-well potential in the horizontal axis, m is the mass of the electron and $\hbar$ the reduced Planck constant.

The two quantum numbers that are taken into consideration are n and m_s; n corresponds to the energy level and m_s is defined as the magnetic quantum number. Since m_s can only take two values ($m_s, = \pm$ ½) , each orbital (ψ_n) can be occupied by two electrons with opposite spins. The orbitals are filled from the lowest electronic level ($n = 1$) onwards. Considering an even number of electrons (N), the highest occupied energy level is $n_F = N/2$. The Fermi energy (ε_F) is the energy of the highest filled level in the fundamental state of a system of N electrons and is defined as:

$$\varepsilon_F = \frac{\hbar^2}{2m}\left(\frac{N\pi}{2L}\right)^2 \tag{2.3}$$

Following the same principles, "The Free-Electron Gas" model can be extended to a 3D system, where the electrons are confined in a cube of side L. Assuming periodic boundary conditions, the wave function for a free electron can be written as:

$$\psi_k(\vec{r}) = e^{i(\vec{k}\cdot\vec{r})} \tag{2.4}$$

where the wave vector $\vec{k}$ is composed by k_x, k_y and k_z, following the constrain of the periodicity where $k = \frac{2n\pi}{L}$. Here, n is a positive or negative integer number depending on the direction of the intrinsic angular momentum of the electron (m_s). Hence, the possible energy states in k-space are:

$$\varepsilon(k) = \frac{\hbar^2}{2m}(k_x^2 + k_y^2 + k_z^2) \tag{2.5}$$

Each state has a volume of $V_k = (2\pi/L)^3$ in the k-space. Being the volume of the Fermi sphere $4\pi k_F^3/3$, and taking into consideration the double occupation of the orbitals, the total number of occupied states $N(\varepsilon)$ at energies ≤ ε is given by:

$$N(\varepsilon) = \frac{V}{3\pi^2}\left(\frac{2m\varepsilon}{\hbar^2}\right)^{3/2} \tag{2.6}$$

where V is the volume of the Fermi sphere with radius L. Finally, the number of occupied states per unit energy – known as density of states (DOS) – can be obtained deriving Equation 2.6 with respect to the energy.

$$D(\varepsilon) \equiv \frac{dN}{d\varepsilon} \tag{2.7}$$

Although "The Free-electron gas" model describes some properties in metals, such as the specific heat capacity, it cannot explain fundamental optical and electronic properties of semiconductors and insulators. Here, we assume that in "The Free electron gas" model the electrons are confined in an infinite 1D square-well potential, neglecting any interaction between them. A more suitable model is given by the Band Theory. Band Theory postulates the existence of energy bands formed by the overlap of atomic orbitals. These bands cover the range of allowed discrete energy levels in which the electrons within the solid can be. In the same way, it defines the "forbidden" bands as the energy ranges where electrons cannot be, introducing the concept of "band gap" in solids.

Crystals, according to this model, can be considered as a periodic lattice of atoms where orbitals are close enough to overlap. It is then necessary to consider the periodicity of the potential created by these periodic atoms. The periodicity of the crystal lattice can be expressed as the function $u_k(\vec{r})$ and leads to the solution of the one-electron Schrödinger equation for a plane wave (Equation 2.4):

$$\psi_k(\vec{r}) = u_k(\vec{r})\ e^{i(\vec{k}\cdot\vec{r})} \tag{2.8}$$

Equation 2.8 is known as the Bloch wavefunction of an electron and considers the periodic potential of the crystal. The energy eigenvalues derived from this wavefunction reveal the existence of forbidden energy ranges and in turn the band structure of the material.The electronic occupation given by the band structure of a solid define its electronic properties. Figure 2.1 shows the classification of solids according to their energy band gap and the movement of electrons between the valence band (occupied states) and the conduction band (empty states).

When the conductive and the valence band overlap there are a large number of free electrons at RT, and the solid is a conductor. On the contrary, if there is a large energy gap between the bands, the movement of the electrons is blocked. As a result, these materials cannot conduct electricity and are called insulators. Finally, when a small energy gap exists, some of the electrons in the valence band can gain enough thermal energy to reach the energy levels in the conduction band. This creates holes in the valence band which increases the conductivity of the solid. These materials are known as semiconductors, although due to the need of thermal energy to conduct electricity they behave as insulators at 0 K.

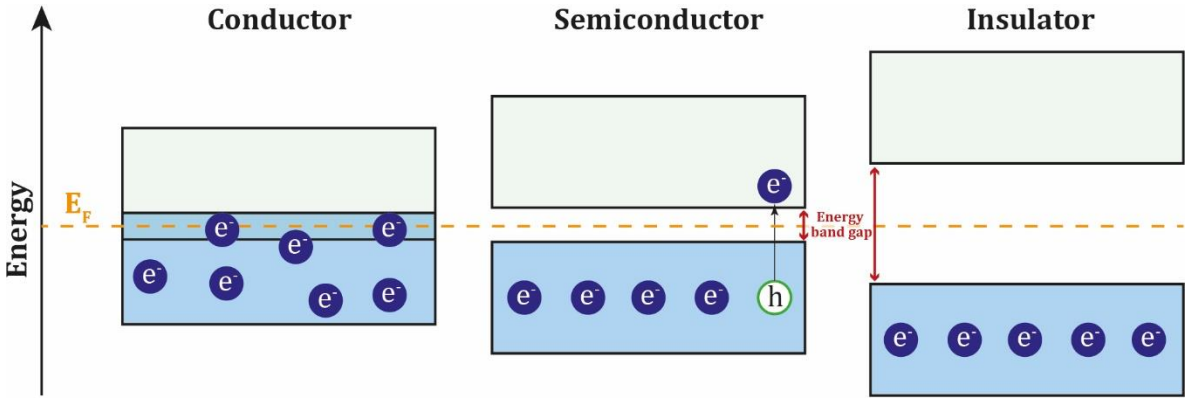

Figure 2-1. Schematic representation of the electronic occupation of the allowed energy bands of a conductor, a semiconductor and an insulator

This is a generic classification of the solid crystals based on their band structures. However, in the 80´s there was a revolution in our understanding of the classification of materials. Topological band theory entered into play, revealing a new taxonomy. This theory predicted the existence of non-trivial topological materials (bulk insulator with metallic boundaries when they are next to a vacuum or a trivial insulator).[26,27] David Thouless, Duncan Haldane and Michael Kosterlitz were awarded with the Nobel Prize in Physics in 2016 for the development of topological band theory.[28] Non-trivial topological quantum phases have been identified in 1D,[29,30] 2D[31] and 3D systems.[32] In the following section a more detailed explanation about 1D topological insulators is given.

2.2 Topological theory in 1D systems

As mentioned above, the band structure defines accurately in many occasions the electronic and optical properties of materials. There are distinct formalisms to infer the band structure in condensed matter physics. In particular, tight binding (TB) model is an approximation used to calculate the band structure of a material by linear combination of atomic orbitals (LCAO).[33] Exploiting such methodology, the Su-Schrieffer-Heeger (SSH) model gives insight into the electronic behavior of 1D polymers.[19] This section provides a general introduction to topological insulators, followed by a description of the topological predictions performed by TB method for the on-surface synthesized linearly linked polyacene and polyperiacene polymers in chapter 5.[20]

2.2.1 Su-Schrieffer-Heeger Model

The Su-Schrieffer-Heeger (SSH) model successfully describes the electronic behavior of polyacetylene polymer.[34–37] Polyacetylene is the simplest 1D π-conjugated polymer formed by $(C_2H_2)_n$ repeating units. It exists in two isomeric forms, altough *trans*-polyacetylene isomer is more favorable at RT[38] and thus it is the one considered in the SSH model. Importantly, *trans*-polyacetylene can exhibit two resonance forms as can be seen in Figure 2.2. Though at first sight they appear electronically equivalent, a deeper study of this system using the SSH model will reveal that they belong to distinct topological quantum phases.

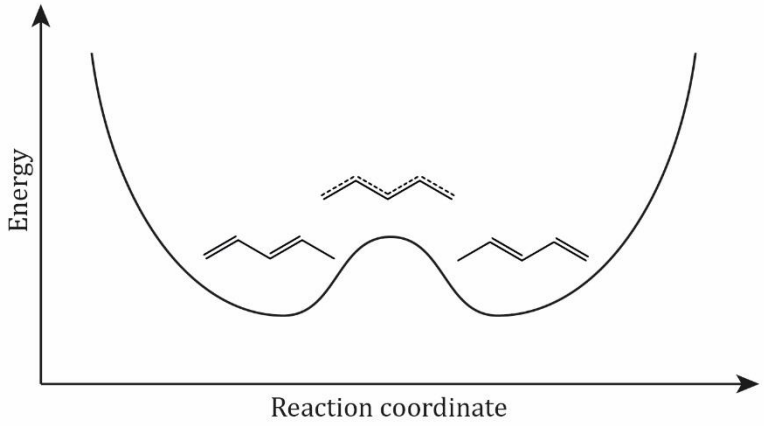

Figure 2-2. Energy landscape versus the reaction coordinate of polyacetylene showing two energetically more favorable forms

TB approximation considers the electron hopping between the nearest neighbors (NN) independently of their spin. When orbitals are close enough to overlap they create a crystal lattice, where the electrons are delocalized hopping from one atom to another (t is the hopping parameter between NN). This way, the motion of one electron can be described with the Hamiltonian:

$$H = -\sum_{ij} t_{ij} |i\rangle\langle j| \tag{2.9}$$

where $-t_{ij}$ is the overlap integral between the NN at positions i and j. In this case, an equal overlapping between all the consecutive atoms in the lattice is considered (where $t_{ij} = t_{ji}$ as exemplified in Figure 2.3) and no interactions between the second nearest neighbors are included ($t_{ii'} = 0$). Therefore, by resolving Equation 2.9 we obtain the band dispersion described by Equation 2.10:

$$\varepsilon(k) = -2\cos ka \tag{2.10}$$

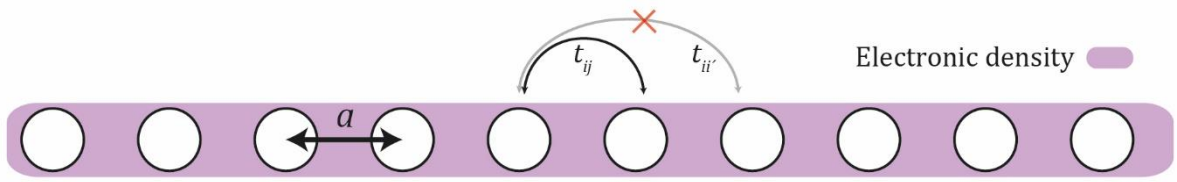

Figure 2-3. Scheme of one dimensional tight binding Hamiltonian with equal orbital overlap within consecutive atoms

However, this approach does not consider the Peierls distortion on the lattice. Actually, we cannot consider an equal overlapping between all the consecutive atoms in the lattice due to the dimerization of the atoms coming from the Peierls distortion, which results in a more energetically favorable final lattice with two possible resonance forms (see Figure 2.2). Therefore, we define two subbands named A and B, a lattice constant of $2a$ and two different hopping parameter per lattice: t_1 and t_2, which correspond to the intra-cell coupling strength and the inter-cell coupling strength, respectively. Importantly, the Peierls distortion gives rise to resonance forms that display inherent chiral symmetry if only first NN hopping is allowed.

Now, the SSH model describes the motion of one valence electron per atom on a two site (A and B) 1D lattice, whereby the electron can only hope between the nearest neighbors:

$$H = t_1 \sum_{n=1}^{N} (|n,B\rangle\langle n,A| + h.c.) + t_2 \sum_{n=1}^{N} (|n+1,A\rangle\langle n,B| + h.c.) \qquad (2.11)$$

where $h.c$ means Hermitian conjugation.

From Equation 2.11, assuming periodic boundaries (only the bulk part of the chain) and considering the two subbands sites (A and B) the matrix form of the band Hamiltonian can be found:

$$H(k) = \begin{pmatrix} \varepsilon_A & t_1 + t_2 e^{-ik} \\ t_1 + t_2 e^{ik} & \varepsilon_B \end{pmatrix} \qquad (2.12)$$

The diagonal terms ε_A and ε_B are zero since only first neighbors hoppings are considered. From the Hamiltonian in Equation 2.12 we can extract the Eigenvalues $\varepsilon(k)$:

$$\varepsilon(k) = \sqrt{t_1^2 + t_2^2 + 2t_1 t_2 \cos k} \qquad (2.13)$$

The dispersion of the bands depends on the relation between the hopping parameters t_1 and t_2. The behavior of Equation 2.13 with respect to t_1 and t_2 is depicted in Figure 2.4a. These graphs show that the band structure evolves from flat bands in the case of $t_1 = 0$ into dispersive bands for $t_1 > t_2$, where the band gap becomes smaller till its closure for $t_1 = t_2$. Then, the band gap reopens for $t_1 < t_2$ forming a dispersive insulator that evolves towards flat bands for larger t_2.

Similar behavior for the gapped situations $t_1 > t_2$ and $t_1 < t_2$ can be assigned from Figure 2.4a. However, this rationalization is uncomplete. In order to understand the band structure the eigenvectors need to be solved. The band Hamiltonian in Equation 2.12 is a two dimensional matrix that can be expressed as the following Equation using Pauli´s matrices:

$$H(k) = \vec{h}(k)\,\hat{\sigma} = h_x(k)\hat{\sigma}_x + h_y(k)\hat{\sigma}_y + h_z(k)\hat{\sigma}_z \qquad (2.14)$$

Since ideal polyacetylene has chiral symmetry, which physically implies that all coupling between sites are off-diagonal, the directions of the vector $\vec{h}(k)$ are:

$$\begin{aligned} h_x(k) &= t_1 + t_2 \cos k \\ h_y(k) &= t_2 \sin k \\ h_z(k) &= 0 \end{aligned} \qquad (2.15)$$

The trajectory of $\vec{h}(k)$ in the first Brillouin zone for the five distinct relations of t_1 and t_2 is depicted in Figure 2.4b.

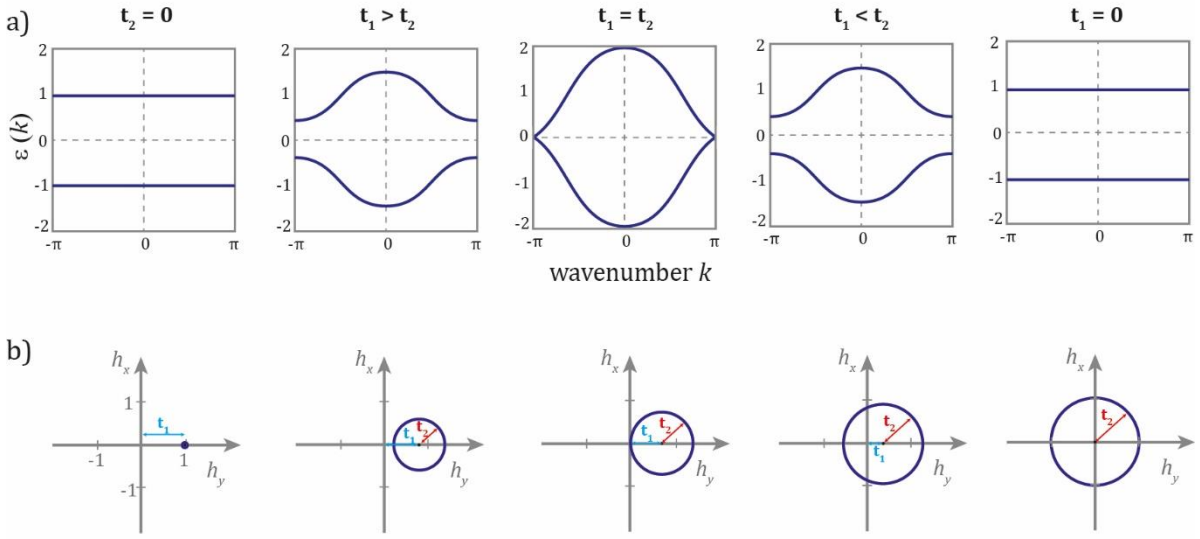

Figure 2-4. Dispersion relation of the bands for different hopping terms with their corresponding $\vec{h}(k)$

a) *Energy bands diagrams and* ***b)*** *Trajectories of $\vec{h}(k)$ over the Brillouin zone for different relations of the hopping parameters.*

Since the vector $\vec{h}(k)$ is on the plane (h(z) = 0), it can be observed from Figure 2.4b that there is no way we can move from $t_1 > t_2$ to $t_1 < t_2$ without crossing the origin, which implies to cross through a metallic state. According to topological band theory, when moving from a gapped insulator A to an insulator B closing the band gap, then there is a change in the topological class. Although it is beyond the scope of this thesis, it is worth to specify that the calculation of the Zak phase of the Hamiltonian actually reveals that

the situation $t_1 > t_2$ belongs to the topologically trivial class (Z=0), whereas $t_1 < t_2$ is a topological insulator class (Z=1).

In fact, a detailed analysis of a finite chain for both topological classes displays the physical consequences on the charge, which can not only be analyzed theoretically, but measured, as illustrated in next chapters. Figure 2.5 shows the fully dimerized cases ($t_2 = 0$ or $t_1 = 0$) for a chain with *N*=10. An insulating bulk structure is expected in both cases, however in the dimerized limit at $t_1 = 0$ there are open boundaries with two single sites at the ends (considering one valence electron per atom). The energy of these states should be zero, since each electron is totally localized at the site at the edge. When $t_1 < t_2$ and $t_1 \neq 0$ the presence of states at the edges is also expected, although the electron could be delocalized between the closest neighbors. In conclusion, the topological transition leads to the emergence of in-gap edge states at the ends of the topological non-trivial polymer, although trivial and non-trivial insulators present similar insulating bulk structure.

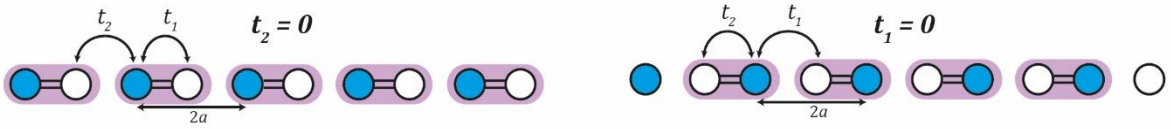

Figure 2-5. Fully dimerized limits of polyacetylene for $t_2 = 0$ and $t_1 = 0$

2.2.2 Topological approach towards linked polyacenes and polyperiacenes

In this work, we have extended the SSH model for more complex π-conjugated linear polymers[20]. It is important to note that this approach is a first approximation to the SSH model with evidently differences. First, it is necessary to define the unit cell dictated by the termination of the polymer. Figure 2.6a shows the asymmetric unit cell of the anthracene polymer (section 5.3) which can be extended for all the polymers connected through an ethynylene/cumulene bridge (Figure 2.6b). The unit cell is formed by a blue and a red block, which correspond to the intracell coupling block (t_1) and the intercell coupling block (t_2), respectively. In the previous subsection we have demonstrated that the relation between these two parameters provides the topological nature of the π-

conjugated polymer, therefore the topological phase can vary depending on the central unit R.

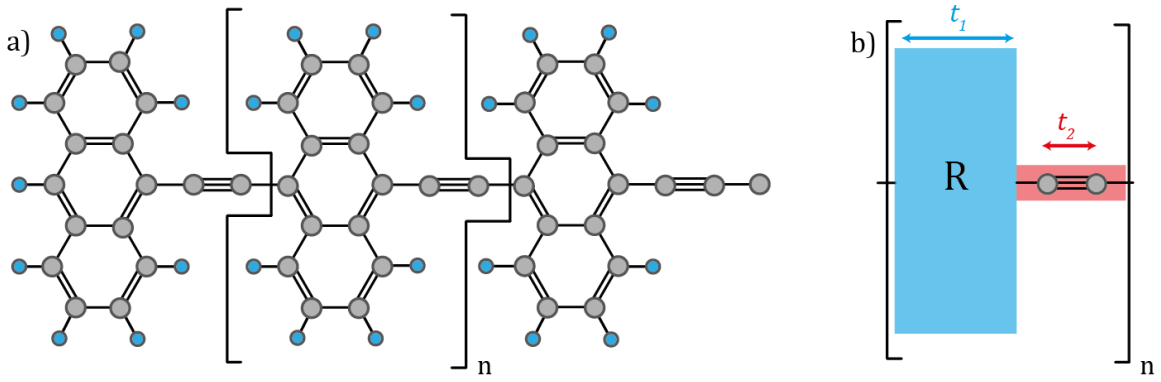

Figure 2-6. Schematic presentation of the unit cell and the hopping parameters

a) *Asymmetric unit cell of ethynylene-bridged anthracene polymer.* ***b)*** *Unit cell for an arbitrary central backbone R.*

Dr. Oliver Gröning performed at *Empa Materials Science and Technology* in Switzerland the tight binding (TB) calculations of the ethynylene-bridged acenes and periacenes polymers by numerically solving the nearest-neighbor hopping (NN) Hamiltonian for the $2p_z$ orbitals of the carbon atoms. The value of the hopping parameters depends on the bond nature between the sites.[39] Here, the intracelll coupling depends on polyaromatic unit ($t_1 = t_{ar} = -3.05\ eV$) and the intercell coupling is related to the triple bond of the ethynylene bridge ($t_2 = t_{tr} = -4.45\ eV$). Considering these values, the TB Hamiltonian introduces two extra parameters related to the polyaromatic unit, which will define the topological nature of the system.

The numerical calculation of the topological invariant (Z) in a discrete k-space was performed using the method of Cao et al.[40] It is worth to highlight that the invariant phase depends on the selected unit cell, which is determined by the termination of the polymer. According to the unit cell depicted in Figure 2.6b, the ethynylene-bridged anthracene polymer structure is Z=0 topological trivial, whereas the ethynylene-bridged pentacene and bisanthene polymers are metallic and the peripentacene polymer belongs to the Z=1 topological region.

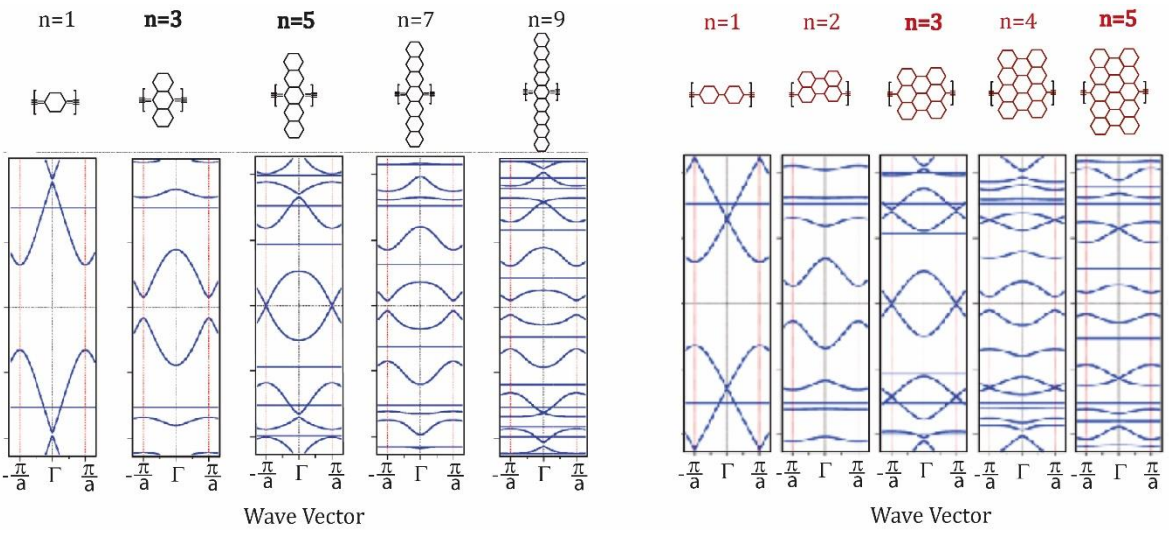

Figure 2-7. Band diagrams for the ethynylene-bridged acene (left) and periacene (right) polymers with increasing size obtained from TB calculations

Figure 2.7 shows the band diagrams for the ethynylene linked acene (left panel) and periacene (right panel) polymers obtained from these TB calculations. Both polymer families present a topological transition, seen by a change in the Zak phase, which implies the closure of the band gap for the pentacene and the bisanthene polymers.

2.3 Scanning Probe Microscopy

Solid-state surfaces and their properties can be studied by means of Scanning Probe microscopies (SPMs) at the atomic scale. The fundamental working principle shared by all scanning probe techniques is based on the measurement of a specific interaction between the target sample and an atom-terminated probe.[21,22] Physical and chemical properties can be measured between a probe and the target surface. Figure 2.8 illustrates the basic components of a SPM where a sample (inset 1) is measured with a tip (inset 2). This tip is attached to a piezoelectric scanner (inset 3) for *x, y, z* movements with atomic level precision. The gap distance between the tip and the sample is controlled by a feedback system that operates controlling the vertical movement of the tip. The data acquired at each individual point of the surface (*x,y*) are recorded and represented as a graphical image by the computer system (inset 4). This computer system allows to set the scanning parameters, control the approaching or retracting of the tip and record the acquisition data.

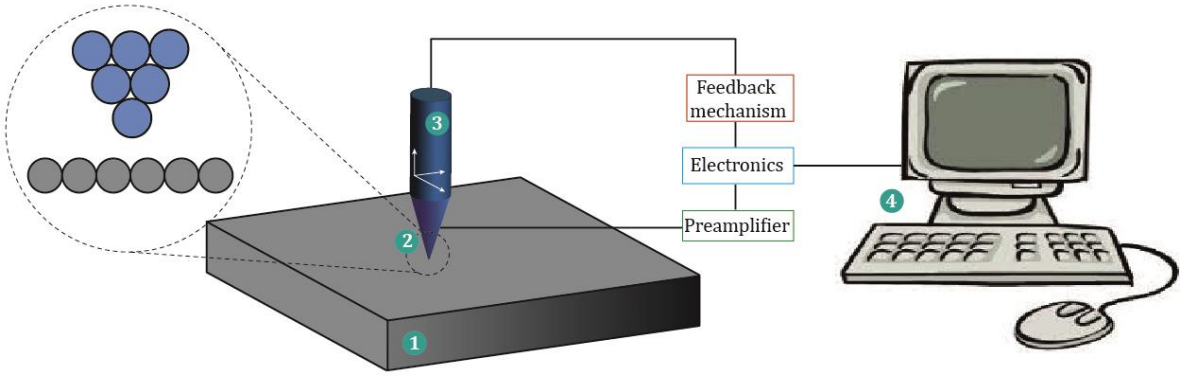

Figure 2-8. Sketch of basic components of SPM

1. Sample. 2. Atom-terminated tip. 3. Piezoelectric scanner. 4. Computer system.

The systems presented in thesis have been characterized by means of Scanning Tunneling Microscopy (STM) and non-contact Atomic Force Microscopy (nc-AFM). These two techniques are described in more detail in section 2.4 and 2.5, respectively.

2.3.1 Working Principles

SPM techniques offer tools to characterize and manipulate the surface samples at the atomic scale.[3,41–44]

Operation modes

When characterizing a surface *via* SPM the images can be acquired following two different operation modes depending on which parameter is fixed and which one is being monitored. The two operation modes employed are described in the following:

- **Constant-height mode**. This mode consists in a constant tip height while scanning the surface in *x* and *y* axes (non-variation of the tip in the *z* axis are observed). The initial tip height is defined by setting specific scan parameters with close-feedback loop (e. g. in STM a bias voltage for a specific current). Then the feedback loop is open and the tip scans the surface recording the specific interaction measured (tunnel current, frequency shift, oscillation amplitude, etc) which results from the variation in the tip-sample distane, *d.* This scanning mode is employed in flat areas with roughness of a few picometers in order to avoid tip crashes with the surface.

- **Constant-interaction mode.** A feedback loop control is employed while scanning at constant-interaction mode. The feedback loop controls the tip height, adjusting it at each single point (pixels of the SPM image) in order to keep the specific interaction measured constant (e.g. in the case of STM is the tunneling current and in nc-FM-AFM the amplitude). This way, the tip-sample distance is changing at each point depending on the differences between the recorded data and the setpoint. The variation in the tip height is performed by applying a specific voltage, V_z, to the piezoelectrics connected to the tip. The V_z applied at each point is recorded in order to constitute the topographic image. This mode is the most common due to the safety conditions provided by the feedback loop.

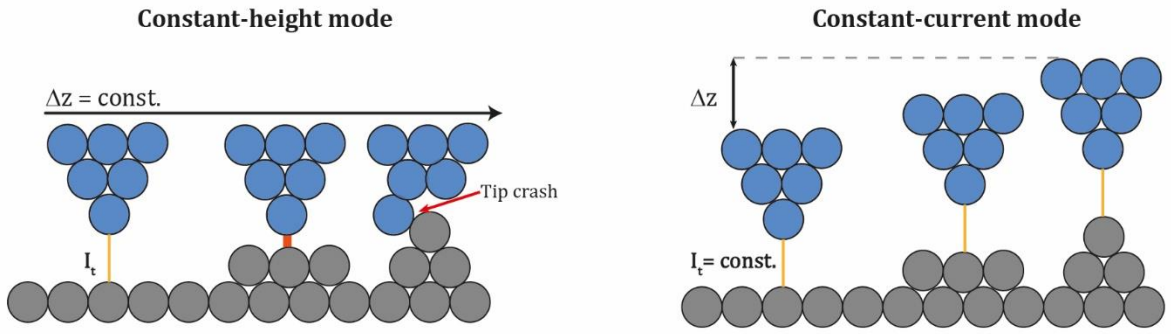

Figure 2-9. Sketch of the operation modes in STM

Left panel: constant-height mode where the tip height is constant and the tunnel current is measured. Right panel: constant-current mode where the tunnel current is constant and the tip-sample distance variations are measured as a function of the V_z applied to the piezoelectric controlling the tip height.

Atom manipulation

One of the advantage intrinsic to SPM is the possibility of manipulating the matter at the atomic scale. There are two possible modes of atomic manipulation:

- **Lateral Manipulation (LM).** SPM allows the manipulation of single atoms or molecules. LM consists on the displacement of the target atom/molecule parallel to the surface (Figure 2.10). The most common way to induce this movement consists the following steps: first, the tip is stabilized on top of the target with standard parameters, and approached towards the surface in order to induce interactions between the tip and the target (a single atom or molecule). Then, the

tip is displaced parallel to the surface resulting in the target movement under the influence of the tip. Finally, the parameters are changed back to scanning conditions.

Depending on the nature of the interaction, three different modes of movements can be induced: i) "*pulling*" mode, where attractive interaction is taking place between the tip and the target; ii) "*pushing*" mode, based on the repulsion forces between the tip and the target; iii) "*sliding*" mode, where weak bonds are formed between the tip and the target resulting in simultaneous movement of both.

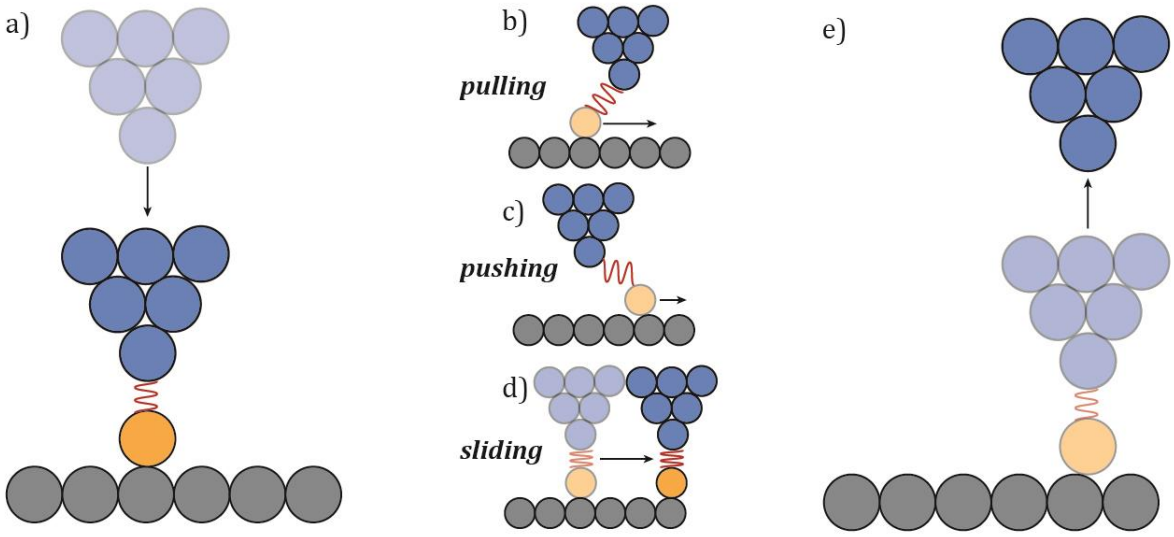

Figure 2-10. Schematic representation of Lateral Manipulation (LM)

a) *Tip approached to the surface inducing tip-atom interaction.* ***b)*** *"Pulling" mode.* ***c)"****Pushing" mode.* ***d)*** *"Sliding" mode.* ***e)*** *Tip retracted and parameters changed to scanning condition.*

- **Vertical manipulation (VM).** Using this manipulation technique atoms and molecules can be picked up and dropped. This can be achieved by changing the scanning parameters to produce the variation of the tip height and induce an electric field (Figure 2.11). In this thesis, this technique has been employed to functionalize the tip apex with CO molecules in order to attain submolecular resolution.[45]

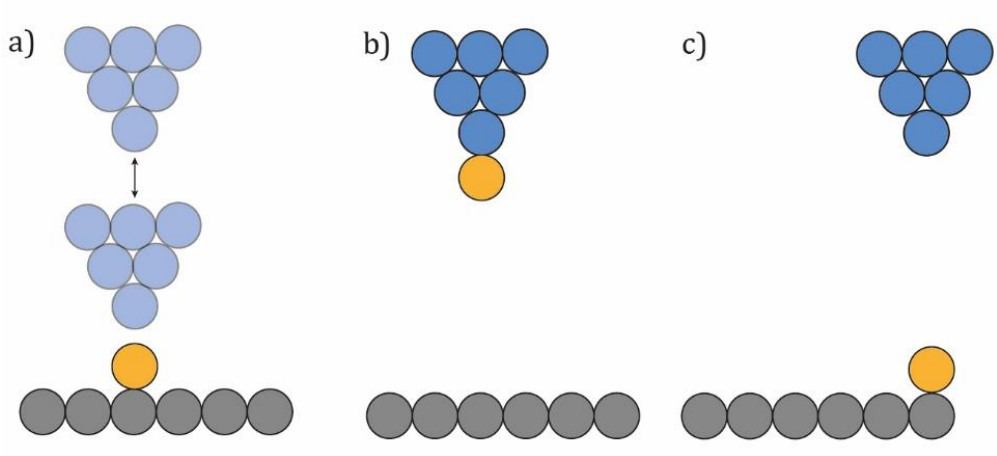

Figure 2-11. Schematic representation of Vertical Manipulation (VM)

a) *Tip height variations.* ***b)*** *Picked up atom.* ***c)*** *Dropped atom.*

2.4 Scanning Tunneling Microscopy

In 1981, Gerd Binnig and Heinrich Rohrer developed the first working STM in IBM Zurich Research Laboratories in Switzerland.[6] The invention of STM allows to image the surface of conductive and semiconductive surfaces at small scale, down to atomic resolution.

The STM is formed by a conductive and sharp tip and a metallic sample separated by a potential barrier of a few Ångström of vacuum. The STM functioning is based on the quantum tunneling effect, which is described in the next section 2.4.1. Briefly, upon applying a bias voltage between the tip and the sample, a tunneling current is produced. The great spatial resolution of the STM is due to the exponential relation between the tip-sample distance and the tunneling current for a constant bias voltage.

2.4.1 Tunnel effect

Quantum mechanics describe the behavior of light and matter at the atomic and subatomic scale. The "wave-particle duality" was one of the revolutionary postulates that changed the understanding of the behavior of a particle. The behavior of electrons confined in an infinite potential well is explained in section 2.1. However, if the potential has now a finite height U_0 the electrons can escape the potential well. In addition, if this potential barrier has a narrow width, electrons could potentially cross it. This is known as tunneling effect which is explained in the following.[46,47]

In order to explain the tunneling effect, we consider a particle with total energy E that is moving in a potential step function energy region with a potential well of height U_0, as described in the next function:

$$U(x) = \begin{cases} 0 & x < 0 \\ U_0 & x > 0 \end{cases} \qquad (2.16)$$

From a classical physics point of view, the speed of such particle of energy E moving in this energy region is defined by $v = \sqrt{2E/m}$ for $x < 0$. When the particle reaches $x = 0$, its behavior depends on the relation between U_0 and E. Figure 2.12 illustrates the two resulting possibilities:

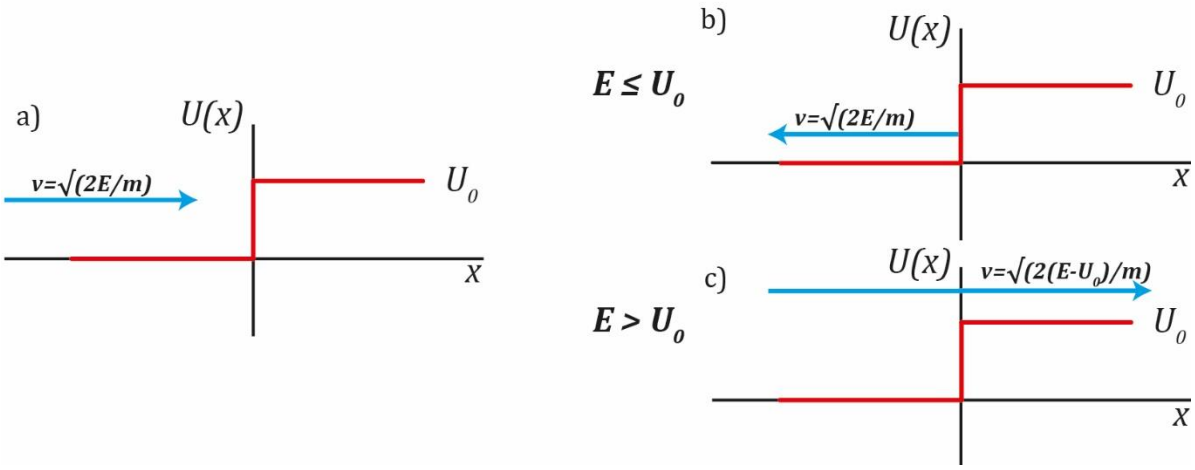

Figure 2-12. A particle moving in a step function energy range from a classical mechanic point of view

a) *Scheme of a classical particle with kinetic energy E moving towards a potential barrier.* ***b)*** *and* ***c)*** *Outcome of the scattering event depending of the relation between potential energy U_0 and kinetic energy E. The red line corresponds to the potential function described using Equation 2.16 and the blue line to the trajectory of the particle.*

Therefore, classical physics postulates that the probability of electron spill-out through the potential barrier for $E \leq U_0$ is zero.

However, the behavior of a particle moving in this potential is different from the point of view of quantum mechanics.[48] As mentioned above, quantum mechanics considers the wave-particle duality nature of a particle (e.g. an electron). This duality nature leads to a non-zero probability of spill-out electron effect through the potential barrier, even if $E \leq U_0$ as demonstrated below. As mentioned in section 2.1, a particle behavior is described

by wave functions derived from Schrödinger Equation. In this case, the wave function can be derived from the time-independent Schrödinger equation (Equation 2.17), which only depends on the position of the particle:

$$-\frac{\hbar^2}{2m}\frac{d^2\psi(x)}{dx^2} + U(x)\psi(x) = E(x) \tag{2.17}$$

Here, m is the mass of the particle, $\hbar$ the reduced Planck constant, U the potential barrier and E the energy of the particle. The solution of Schrödinger Equation for a free particle moving in a 3D system is described in Equation 2.4. Now, considering a linear movement towards this potential in x, the two possible solutions for $\psi(x)$ are:

$$\psi(x)\begin{cases}\psi(0)e^{-i\sqrt{\frac{2m(E-U)}{\hbar^2}}x} = \psi(0)e^{\pm ikx} & E > U \\ \psi(0)e^{-\sqrt{\frac{2m(U-E)}{\hbar^2}}x} = \psi(0)e^{-kx} & E < U\end{cases} \tag{2.18}$$

On one hand, if $E > U$, the wave vector suffers a drastic change from $k_1 = \sqrt{2mE/\hbar^2}$ to $k_2 = \sqrt{2m(E-U)/\hbar^2}$ and part of the wave will be reflected and the other part transmitted. On the other hand, when $E < U$, the wave function suffers an exponential decay as shown in Figure 2.13a. The wave function crosses a short range of the "forbidden" area at $x > 0$ and then it is entirely reflected.

For $E < U$, the wave is transmitted with an exponential decay through the potential barrier. Therefore, if the barrier shows a finite and short thickness the probability of detecting the particle on the other side of this one-dimensional potential barrier is non-zero (Figure 2.13b). This phenomenon is known as quantum tunneling effect, and it is very sensitive to the width and the height of the potential barrier.

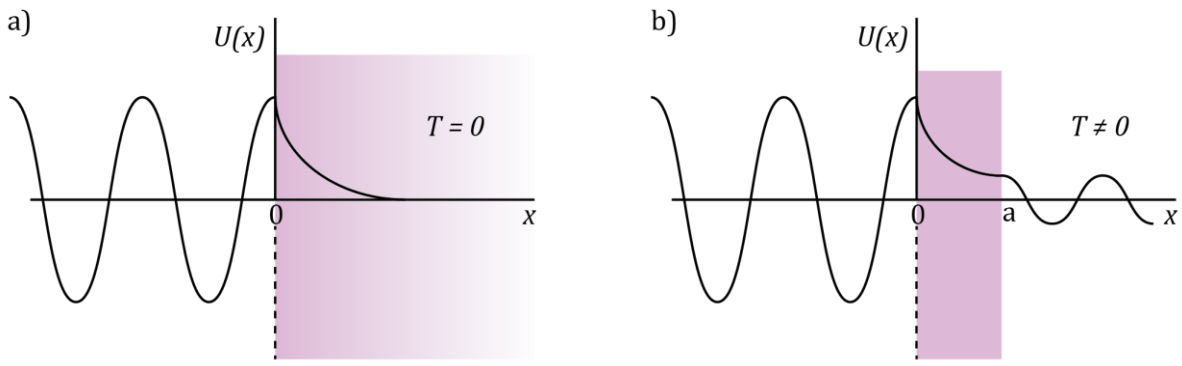

Figure 2-13. Scheme of quantum tunneling effect through a potential barrier

a) *Exponential decreases of the wave function considering a wide barrier.* ***b)*** *Tunnel effect where the particle could tunnel through a narrow barrier. T is the transmission coefficient, defined as the ratio of transmitted current density.*

The density of probability - $\Gamma(x)$ - of a particle to tunnel through a narrow potential barrier is described by Equation 2.19 and depends on the energy difference $(U - E)$ or work function (Φ), and corresponds to the minimum energy needed to remove an electron from a solid surface.

$$\Gamma(x) = |\psi(x)|^2 = |\psi(0)|^2 e^{-2\sqrt{\frac{2m\Phi}{\hbar^2}}x} \qquad (2.19)$$

In STM the particles are electrons, the potential barrier is the vacuum and the two electrodes are the tip and the sample. When a small bias voltage (V_b) is applied, all electrons in occupied states between Fermi level (E_F) and E_F-V_b are considered to be able to tunnel from tip to sample or *vice versa*. Figure 2.14 shows the energy diagrams of the tunnel junction in a sample-vacuum-tip depending on the bias voltage applied. At the initial stage non-bias voltage is applied between the tip and the sample ($V_b = 0$), resulting in a thermodynamic equilibrium with their Fermi levels aligned. Then, when applying a bias voltage to the sample with the tip grounded two scenarios are possible: i) For $V_b < 0$: the energy levels of the sample are shifted up, leading to a tunneling current from the occupied states of sample towards the tip. ii) For $V_b > 0$: the energy levels of the sample are shifted down and the tunneling current goes from the tip to the unoccupied states of the sample.

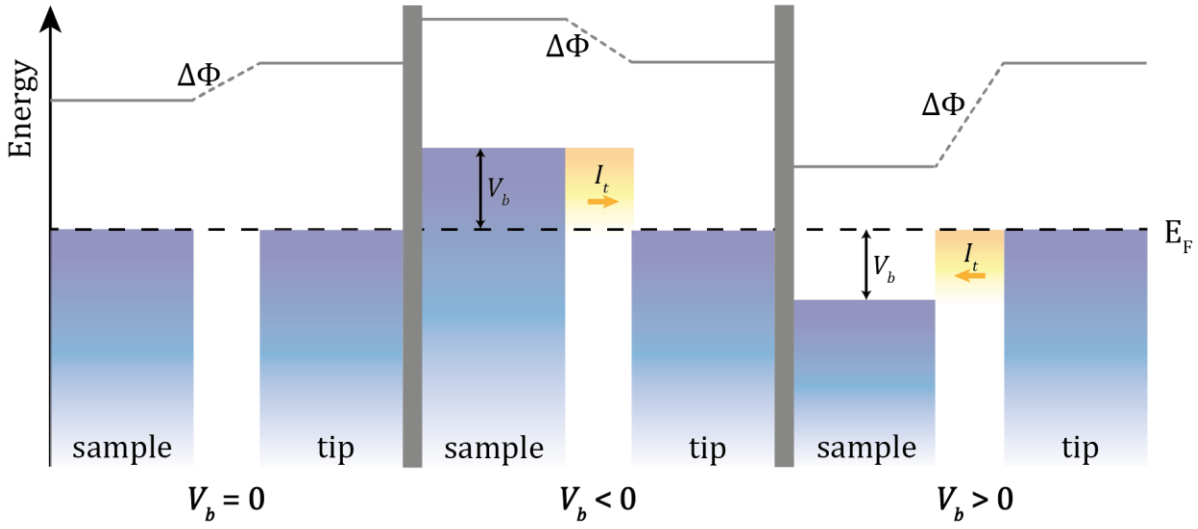

Figure 2-14. Energy diagram of the tunneling sample-vacuum-tip junction

Three different scenarios depending on the bias voltage are shown: left panel: $V_b = 0$, medium panel: $V_b < 0$ and right panel: $V_b > 0$.

From Equation 2.19 - probability of one electron crossing the finite energy barrier - the tunneling current is defined as the electrons flow from the states between E_F and $E_F - V_b$:

$$I_t \propto \sum_{E_F - V_b}^{E_F} |\psi(x)|^2 \propto V_b \rho_s(0, E_F) e^{-2\sqrt{\frac{2m\Phi}{\hbar^2}}x} \tag{2.20}$$

Where I_t is the tunneling current, V_b the bias voltage, x the tip-sample distance and ρ_s the local density of states (LDOS) of the sample surface.

A better approximation was obtained by Nobel Laurate Prof. John Bardeen, who calculated the tunnel matrix between two electrodes of a metal-insulator-metal junction.[49] This approximation considers independent wave functions for each of the two electrodes and finds the overlap between these two wave functions (restricted only to electron with same energy levels). Bardeen´s formalism takes several assumptions: negligible interaction between the electrons, negligible electronic coupling between the two electrodes and only elastic tunneling processes.

Then, Tersoff and Hamann extended the method of Bardeen´s formalism for a 3D-tip model with negligible wave function angular dependence (s-wave).[50] They calculated an expression for the tunneling current in a STM, considering independent wave functions for the tip and the sample (ψ_t and ψ_s, respectively):

$$I_t = \frac{2\pi e}{\hbar}\int_{E_F}^{E_F+V_b} \rho_s(E - eV_b)\rho_t(E)|M_{st}|^2 dE \tag{2.21}$$

Where the tunneling matrix element (M_{st}) is defined as:

$$M_{st} = \frac{\hbar^2}{2m}\int (\psi_s^* \nabla\psi_t - \psi_t^* \nabla\psi_s) dS \tag{2.22}$$

On a surface S, which is considered as an infinitesimal surface in the vacuum barrier between tip and sample. Finally, for a small bias voltage applied Equation 2.21 can be derived into the following expression of the tunneling current:

$$I_t \propto V_b e^{-2\sqrt{\frac{2m\Phi}{\hbar^2}}R} \rho_t(E_F)\rho_s(E_F, r_0) \tag{2.23}$$

Where $r_0 = R + d$ (R is the radius of curvature of an s-wave tip and d is the tip-sample distance) and Φ is the local barrier height. From these equations it can be concluded that the tunnel current depends on the LDOS of the sample and the tip (ρ_s and ρ_t),[51] the shape of the tip (R),[52] the bias voltage (V_b) and the tip-sample distance (d). Therefore, the images acquired by STM are a convolution between the electronic structure of both sample and tip, the topography of the sample, and the shape of the tip.

2.4.2 Scanning Tunneling Spectroscopy

STM is a powerful technique to resolve the electronic structure of metallic surfaces with subnanometer spatial resolution. Equation 2.21 shows the dependence of the current with the LDOS of the sample and the tip (ρ_s and ρ_t) and with the tunneling matrix element (M_{st}). Considering that M_{st} and ρ_t are independent of the bias voltage applied, the derivative of Equation 2.21 reveals:

$$\frac{dI}{dV} \propto \rho_s(eV_b)\rho_t(0) \tag{2.24}$$

Thus, the differential conductance provides information about the electronic structure of the sample, being able to probe both unoccupied ($V_b > 0$) and occupied ($V_b < 0$) states.[21] STS allows the determination of the frontiers orbitals of molecules (HOMO and LUMO)[53] and the onsets of the conduction and valence bands (VB and CB) of solids,[54] as well as being able to reveal magnetic features.[55]

Typically and in this thesis, the *I*-*V* curves are acquired by stabilizing the tip on top of a specific point, switching off the feedback loop and applying a bias voltage ramp while recording the tunneling current in the junction with a lock-in amplifier using a fixed voltage modulation (V_{rms}). Other parameters to be set are the acquisition time per input signal (time raster) and the sensitivity of such signal. The lock-in amplifier makes a convolution of the input signal – this is, the tunneling current - with the internal AC reference signal, whose frequency and phase are fixed. From this convolution, the lock-in extracts a signal from the first or second order, which corresponds to the first or second derivative of the tunneling current (I_t) with respect to the bias voltage V_b.

In addition, this powerful technique allows to resolve the appearance of the molecular orbitals of the sample with spatial resolution by acquiring dI/dV maps. First, the specific energies of the frontiers orbitals or bands have to be detected in the dI/dV spectra recorded. Next, the bias voltage is set at this specific energy and the lock-in output signal at every single pixel (*x*,*y*) is acquired. This can be done with the feedback loop on (constant-current dI/dV maps) or keeping constant the tip-sample distance (constant-height dI/dV maps).

2.5 Non-contact Atomic Force Microscopy

The first Atomic Force Microscope (AFM) was developed in 1986 by Gerd Binnig, Calvin Quate and Christoph Gerber.[7] The AFM emerged as a powerful technique to complement the STM, finding applications in a wide range of fields due to the ability to characterize and manipulate conductive, semiconductive and insulating samples. The working

principle of AFM is based on the force interaction between a sharp tip attached to a cantilever and the surface of the sample. There are three main operation modes of AFM: contact mode (physical contact between the sample and the tip), non-contact mode (tip oscillates although the tip does not contact the surface) and tapping mode (tip oscillates contacting intermittently the surface).[56]

The AFM work presented in this thesis was performed under the non-contact mode (nc-AFM). This allowed to characterize on-surface reactions and chemical and geometric properties of the prepared materials with submolecular resolution. All the nc-AFM measurements were performed in UHV, at 4 K and with a CO-functionalized tip for enhanced resolution. Single CO molecules were attached to the apex of the metallic tip, allowing for submolecular resolution and real visualization of chemical bonds.[57]

Nc-AFM offers two different operation modes: Amplitude modulation (AM-AFM)[58] and frequency modulation (FM-AFM).[59] At the initial stage of both modes the tip oscillates about its own eigenfrequency and at an amplitude of a few tens of picometers. The tip vibration can be described as a driven damped harmonic oscillator characterized by the eigenfrequency (f_0), the spring constant (k_0) and the quality factor (Q).

In AM-AFM the cantilever oscillates at an off resonance frequency ($f_{drive} \neq f_0$). The forces vary with the tip-sample distance, which produces a change in the frequency oscillation (frequency shift or Δf) and, as consequence, an amplitude variation in the tip oscillation amplitude. The cantilever amplitude is read and used by the feedback loop in order to keep constant the frequency shift by correcting the tip-sample distance.

Differently, when using FM-AFM the tip oscillation is always excited at an on resonance frequency (f_0), while keeping constant the tip-sample distance. In this mode, the frequency shift (Δf), which is the change in the frequency resonance of the sensor, provides direct information related to the tip-sample interaction. The feedback keeps the tip excited at its resonance frequency (f_0). Furthermore, an additionally feedback keeps the amplitude of the resonance constant.

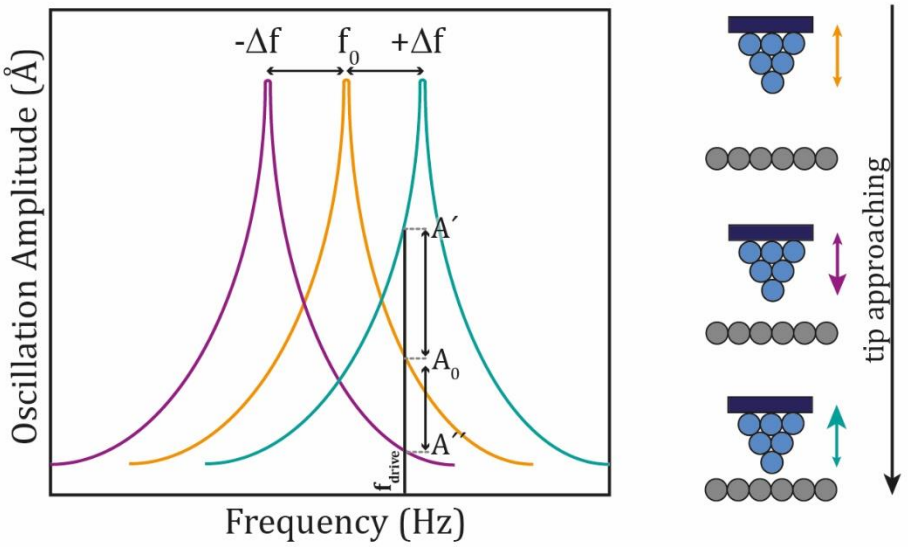

Figure 2-15. Resonance curves of nc-AFM cantilever

The orange line shows the resonance frequency when the tip is far away from the sample, the purple line corresponds to an attractive force between the tip and the sample and the green line corresponds to a repulsive force between the tip and the sample.

The nature of the force interactions between the sample and the tip can be attractive or repulsive, depending on the tip-sample distance. When approaching the tip, attractive forces act between the tip and the sample first, which causes a frequency shift towards negative values and larger amplitude oscillation. Then, when the tip approaches surface further, repulsive forces act between the tip and the sample producing a frequency shift towards positive values and the decrease of the amplitude oscillation. Figure 2.15 summarizes the tip-sample dependence with the frequency shift and the amplitude.

The work in this thesis was completed using the FM-AFM mode only, since in UHV conditions the cantilever oscillator has a high quality factor.[23] In addition, this mode provides information about non-conservative forces.

2.5.1 Theoretical background

The relation between the parameters of oscillation of the cantilever and the tip-sample gradient force ($\frac{\partial F_{ts}}{\partial z}$) can be derived following a series of mathematical steps.[60–62]

The cantilever can be considered a harmonic oscillator sensitive to external stimuli, such as force interactions. Far from the sample the cantilever is excited on resonance at an eigenfrequency (f_0) :

$$f_0 = \frac{1}{2\pi}\sqrt{\frac{k_0}{m}} \tag{2.25}$$

Where k_0 is the spring constant and m the effective mass. However, under certain external forces the eigenfrequency of the oscillation changes and this signal is recorded as the frequency shift (Δf). A linear response of the external force on the frequency shift due to the small values of amplitude can be approximated as a linear equation:

$$\Delta f = f - f_0 \sim \frac{1}{2\pi}\left(\sqrt{\frac{k_{ts}+k_0}{m}} - \sqrt{\frac{k_0}{m}}\right) \tag{2.26}$$

Where k_{ts} is an additional spring constant coming from the potential energy created between the tip and the sample and originated from external forces. The square root can be approximated in the limit $k_{ts}<k_0$ and using Taylor expansion Equation 2.26 derives into:

$$\Delta f \sim \frac{1}{4\pi}\frac{k_{ts}}{\sqrt{k_0 m}} \tag{2.27}$$

Rearranging Equation 2.25 into $\frac{1}{\sqrt{m}} = \frac{2\pi f_0}{\sqrt{k_0}}$ and substituting it in Equation 2.27 we arrive to the following equation:

$$\Delta f \sim \frac{1}{2}\frac{f_0 k_{ts}}{k_0} \tag{2.28}$$

As previously mentioned, a linear dependence of the force with the tip-sample distance is considered, where $k_{ts} = -\frac{\partial F_{ts}}{\partial z}$. Finally, a direct relation of the frequency shift and the forces between the tip and the sample can be derived:

$$\Delta f \sim \frac{1}{2}\frac{f_0}{k_0}\left(-\frac{\partial F_{ts}}{\partial z}\right) \tag{2.29}$$

This small amplitude approximation gives a direct relation between the frequency shift and the gradient forces valid for all the nc-AFM measurements presented in this thesis.

2.5.2 Forces contribution

In this section a brief explanation about the forces and the frequency shift dependence with the tip-sample distance is given.

The interactions between the tip and the sample are mainly composed by three different types of forces: Van der Waals, electrostatic and chemical.[63–66] The total force and its main components dependence with the tip-sample distance are described in Figure 2.16a. In addition, Figure 2.16b shows a scheme of the frequency shift dependence with the tip height and reveals that approaching the tip towards the surface we can move from the attractive regime to the repulsive regime which implies crossing a minimum frequency shift.

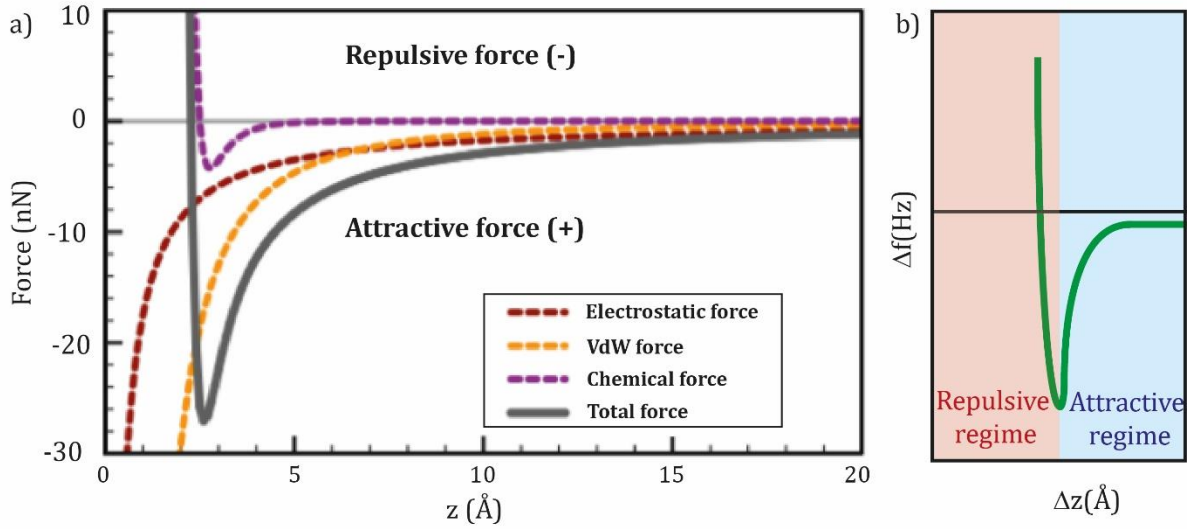

Figure 2-16. Forces contribution in nc-AFM

a) *Force and* ***b)*** *frequency shift dependence with the tip-sample distance. Adapted from reference* 67.

- **Van der Waals force**: It is a long-range force based on inter-molecular electrostatic interaction between dipoles. They can be induced by: i) two permanent dipole moment (Keesom forces), ii) an induced-dipole moment and a permanent dipole (Debye forces) and iii) two induced-dipoles (London dispersive force, which is an inter-molecular force always present). Its contribution decays exponentially with the tip-sample distance. The Van der Waal force between a sphere and an infinite 2D plane at a specific distance is:

$$F_{VdW} = -\frac{HR}{6z^2} \tag{2.30}$$

Where z is the tip-sample distance, R the radius of the tip and H the combined Hamaker constant of the sample and the tip. Sharp tips contribute to reduce the Van der Waal force contributions because the total value of the force and the radius of the tip (the sphere) are directly proportional, as shown in Equation 2.30.

- **Electrostatic force**: It is originated from the different work function between the tip and the sample (Φ_t and Φ_s), creating an electric potential gradient. They are long-range forces with attractive character. This force is used as the working principle of KPFM (Kelvin Probe Force Microscopy). The electrostatic force behaves like a capacitor with two electrodes at a specific distance where a bias voltage is applied between the electrodes:

$$F_{elec} = \frac{1}{2}\frac{\partial C}{\partial z}(V_b - V_{CPD}) \tag{2.31}$$

V_{CPD} corresponds to the contact potential difference originated from the distinct work functions between tip and sample. Equation 2.31 reveals the direct dependence of the electrostatic force on the bias voltage.

- **Chemical bonds**: They are short range forces between tip and sample originated from the overlap of the electronic orbitals. They are based on the Pauli Exclusion Principle, and thus are named Pauli repulsive forces. The interaction is stronger for higher density of electrons and provides information about the chemical

nature of the sample. Its behavior as a function of the tip-sample distance can be described by differentiating the Lennard-Jones potential:

$$F_{LJ} = \frac{12E_{bond}}{z_0}\left[\left(\frac{z_0}{z}\right)^{13} - \left(\frac{z_0}{z}\right)^{7}\right] \quad (2.32)$$

E_{bond} is the energy of the bonded tip-sample junction and z_0 the equilibrium distance where the potential of Lennard Jones reaches a minimum.

All of these contributing forces provide detailed information about the sample surface and they all depend on the tip-sample distance

2.5.3 Force spectroscopy

This nc-AFM technique allows to detect the forces between the surface and the tip at a specific point by measuring the frequency shift variation *versus* the tip-sample distance.[68–70] In this thesis, force spectroscopy was employed to elucidate tentative heights (avoiding electronic contributions) and the bond order of the systems under study. Such measurements were performed by stabilizing the tip on top of the target position. Then, the feedback loop was switched off in order to fix a common z_{start} between the different spectra acquired (assuming that the z-plane was previously detected). The *Δf(z)* spectra acquisition consists in recording the frequency shift while the tip approaches towards the sample following a z_{ramp} previously fixed. The comparison of the tip height at the frequency minimum of two force spectra acquired at different positions allows the extraction of the height difference between such positions.

This technique has also been extended to get information about the height and the minima frequency shift with spatial resolution. To do so, several constant-height frequency shift nc-AFM images were acquired at different heights (which correspond to the z_{ramp}). The minima frequency shift was extracted at each of the pixels. Finally, the tip height at the minima frequency shift were represented in an image (z_{map} and f_{map}, respectively) that reveals the roughness of the area. Unfortunately, an important limitation of such approach is that these measurements can only be performed in areas with a low corrugation, due to the required constant-height operation mode.

3. Experimental set-up

State-of-the-art ultra-high vacuum systems have been employed in order to develop new strategies towards the design of functional nanomaterials for sustainable energy applications. Whereas in the previous chapter we introduced the theoretical concepts behind the used measurement techniques, here we will describe the experimental methods and instrumentation employed to achieve the goals of the thesis.

The experiments were performed in four distinct ultra-high vacuum systems, each of them customized for a specific purpose, namely:

1. The Aarhus XPS-STM system from *Specs*, hosted at surface science laboratory (LASUAM) of *Universidad Autónoma de Madrid*, designed for fast grow and characterization with variable temperature STM of samples (100-400 K), while allowing X-Ray Spectroscopy.[71,72]

2. A *Createc* nc-AFM/STM set-up, hosted at the *Regional Center of Materials* in Olomouc (Czech Republic), in collaboration with Dr. Bruno de la Torre and Prof. Pavel Jelínek.

3. The *Omicron* LT-STM system at *IMDEA Nanoscience*, focused on low temperature microscopy/spectroscopy.[73,74]

4. The recently deployed Omicron low-temperature nc-AFM/STM at IMDEA Nanoscience, which combines two powerful surface techniques.

The four ultra-high vacuum systems are composed of the same main building blocks and some shared components, which are showed in Figure 3.1. It is worth to highlight that the four of them operate under UHV conditions, therefore they comprise different pumping stages (inset 7 in Figure 3.1), which contribute to reach a base pressure of $\sim 10^{-10}$ mbar.

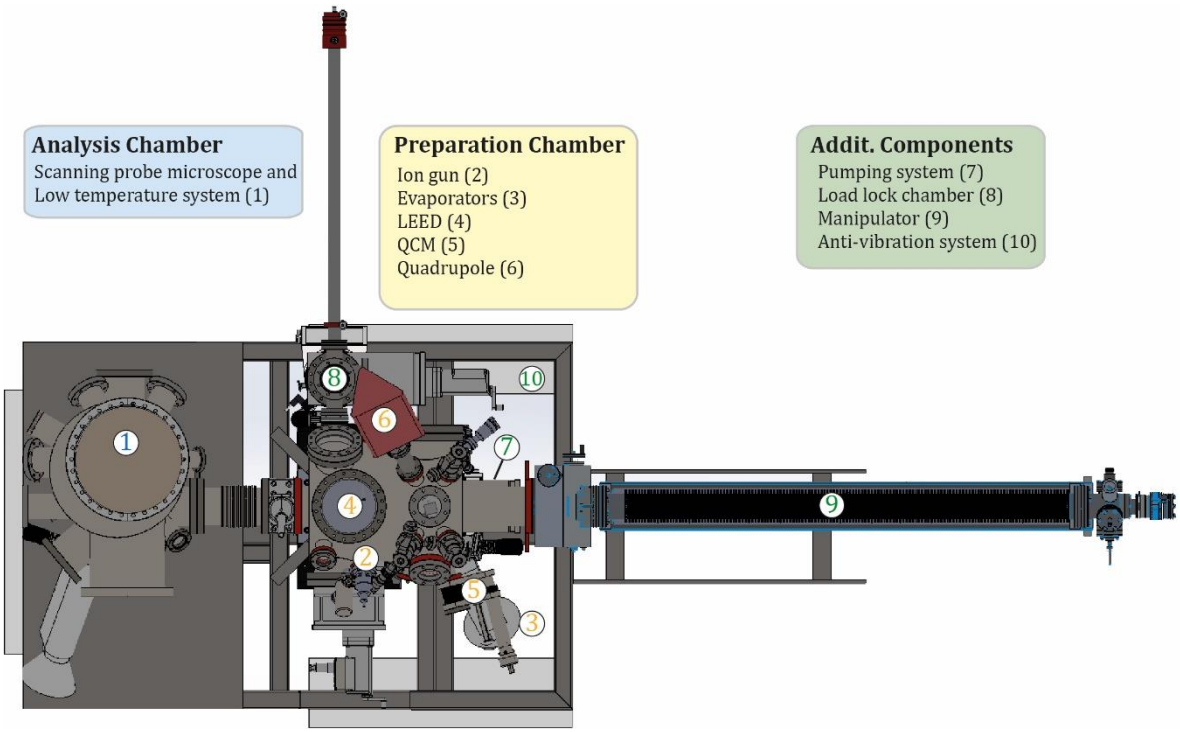

Figure 3-1. Scheme of a UHV system hosting a low temperature scanning probe microscope

Image courtesy of Dr. Koen Lauwaet.

These UHV systems are comprised by two main chambers: the preparation chamber and the analysis chamber (marked in yellow and blue in Figure 3.1, respectively). The preparation chamber is equipped with all the required instruments for preparing the desired samples and some additional characterization techniques. The analysis chamber hosts the scanning probe microscope and the cooling down system (inset 1 in Figure 3.1). The prepared sample is transferred to the analysis chamber using the manipulator (inset 9 in Figure 3.1), which is also equipped with a sample heater. Finally, these systems contain some additional components, as the load lock chamber (inset 8 in Figure 3.1) with its own pumping system in order to introduce or extract samples without breaking the ultra-high vacuum. In addition, all the systems are equipped with anti-vibration instrumentation (inset 10 in Figure 3.1), which is required in order to achieve the highest resolution as possible.

As mentioned above, all these components are present in the four UHV systems employed for the thesis. Then, a more detailed technical description of all these components is given for the newly mounted nc-AFM/STM located at IMDEA.

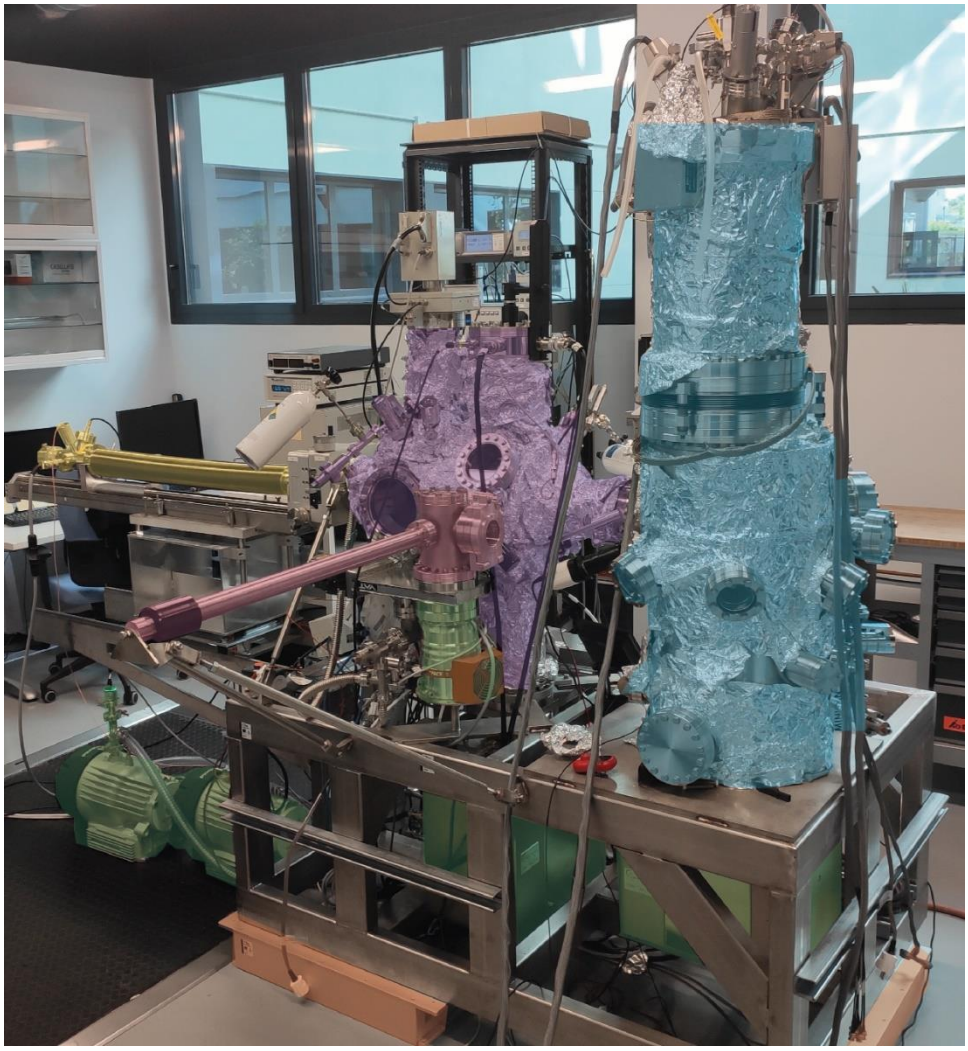

Figure 3-2. Photograph of the LT nc-AFM/STM set-up

The LT nc-AFM/STM comprises the preparation chamber, the manipulator, the analysis chamber, the load-lock chamber, the anti-vibration system and the pumping system, which are highlighted in purple, yellow, blue, red, orange and green, respectively.

3.1 Low temperature nc-AFM/STM

Figure 3.2 shows a photograph of the LT nc-AFM/STM set-up located at IMDEA. We can distinguish in the photograph the two main components: the preparation chamber (highlighted in purple) and the analysis chamber (highlighted in blue). The samples are transferred between the chambers using the manipulator (highlighted in yellow). In addition, it is observed the load lock chamber with its transfer bar (highlighted in red) and its own pumping system (highlighted in green).

3.1.1 Pumping system

All the experiments in this thesis were performed in UHV conditions due to the need to preserve the sample at the cleanest condition as possible.[75] Pressures of around 10^{-10} mbar are achieved in order to avoid the presence of adsorbates or contaminants, which can alter the physical and chemical properties of the target samples, before or during the measurements. Such ultra-high vacuum environment is obtained by means of a three-stage pumping system formed by three distinct pumps which are continuously working: the scroll pump, the turbo molecular pump (TMP) and the ion pump.

To achieve a pressure of 10^{-10} mbar range, it is first necessary to pump down the system from atmospheric conditions with a scroll pump (*Leybold SCROLLVAC 7 plus*), which supplies a pressure range $\approx 10^{-3}$ mbar. One of the main advantages of these pumps is that they are oil-free, avoiding any risk of contamination of the UHV chamber. The two main parts of the scroll pumps are two co-wound spiral scrolls located in a vacuum compartment with an input valve and an exhaust valve at the center of the scroll. The gas that enters is trapped between the spirals, as the free spiral moves the gas is transported and compressed towards the center of the scroll where it leaves through the exit valve. When the spiral moves back to initial position, the difference in pressures favors the entry of new gases and the restart of the pumping process.

The TMP employed for pumping the nc-AFM/STM system is a *Pfeiffer HiPace 300 H* model, which is connected to the preparation chamber through an electro-pneumatic UHV gate valve, which automatically closes if a cut in the power supply is detected. The TMP requires a force-vacuum for a proper operation, which is provided by the scroll pump. Therefore, both the scroll pump and the TMP are connected in series. The TMP can pump down the system up to a pressure of 10^{-10} mbar by transferring momentum to the gas molecules that collide with the rotors. The gas molecules are compressed in the TMP and transferred to the scroll pump. This turbo pump shows the highest compression rate of H_2, which is the most difficult gas to remove of a UHV chamber.

The third stage of pumping is provided by two ion pump from *Gamma Vacuum* located in the preparation and the analysis chamber in order to maintain the UHV pressure, and

even pump down to 10^{-11} mbar. The ion pump is constituted by a cathode-anode-cathode configuration with steel tubes forming the anode and titanium plates the cathodes. A strong electric potential is applied between them, resulting in an electric discharge from the Ti plates to the steel tubes producing the ionization of residual gases, which are redirected towards the cathodes and buried.

Additionally, the pumping system can include two other mechanisms for preserving the UHV conditions: Titanium sublimation pump (TSP) and a cold trap (CT). The TSP consists in a titanium rod located in the ion pump (which is also from *Gamma vacuum*). Titanium is first sublimated by applying high currents, and then these Ti atoms cover the walls of the chamber and can react with contaminants removing/burying them. The CT consists in a nitrogen refrigerated system that favors the condensation of contaminants of the chamber. In our system, the cryostats of the analysis chamber act as a cold trap.

Finally, the pressure in the chamber is measured with a Bayard-Alpert hot cathode ion gauge from *Agilent*, which is composed by 3 electrodes (collector, filament and grid). The electrons emitted from the filaments are accelerated towards the grid by applying high voltage between them, producing the ionization of the residual gases. The ionized residual gases are redirected against the collector, therefore the current measured at the collector provides a direct relation of the amount of contaminants in the chamber.

In order to preserve the UHV conditions in the preparation chamber, a smaller chamber (load lock chamber) equipped with an individual pumping system (a scroll pump and a TMP) is connected to the preparation chamber. The load lock allows to insert and extract new samples or tips without venting the preparation chamber.

3.1.2 Preparation chamber

The main goal of this chamber is the preparation of samples by cleaning the crystals and the growth of nanomaterials. The preparation chamber hosts additional equipment in order to complement the characterization of the samples. A brief description of the main instrumentation is given in the following:

Sample cleaning

All the experiments carried out in this thesis were performed on a Au(111) surface. The monocrystal is mounted on a sample holder with a specific design from *Omicron* where it is welded with a tantalum foil (see Figure 3.3a).

The cleaning of the Au(111) monocrystal is performed by repetition of sputtering and annealing cycles. The *sputtering* process consists in removing atomic layers from the Au(111) crystal by Ar^+ bombardment. First, we expose the chamber to 2.1 x 10^{-6} mbar of Ar through a leak valve. Then, the inert argon gas passes through the sputter gun, installed in the preparation chamber, ionizing the gas into Ar^+ by electron impact. These ions are accelerated at 1.5 keV against the Au(111) surface at normal incidence for ≈ 10 mins. The measured incoming current from the sample is typically 7-15 μA.

Once the *sputtering* is finished the sample is annealed at 700 K for 15 minutes in order to promote surface diffusion and prepare a clean and flat monocrystal. The substrate is annealed with a heater supplying the specific DC voltage and current to run it in radiative mode. The tentative temperature of the substrate is measured with a type N thermocouple attached to the sample holder as closest as possible. These sputtering and annealing cycles are repeated 2 or 3 times in order to achieve a clean substrate.

The manipulator is commercial from *UHV design* and allows to anneal the samples and rotate them towards the ion gun or the evaporators (rotation range from 0º to 360º). The manipulator can be moved along the chamber (in X, Y and Z) and allows to transfer the prepared sample to the analysis chamber. The head of the manipulator is mainly equipped with a yttria coated tantalum foil heater, a LN_2 tank connected to a refrigeration system, a type N thermocouple and a sample carrier specially designed for *Omicron* sample holders, which is electrically isolated allowing e-Beam heating mode (Figure 3.3b shows the schematic design).

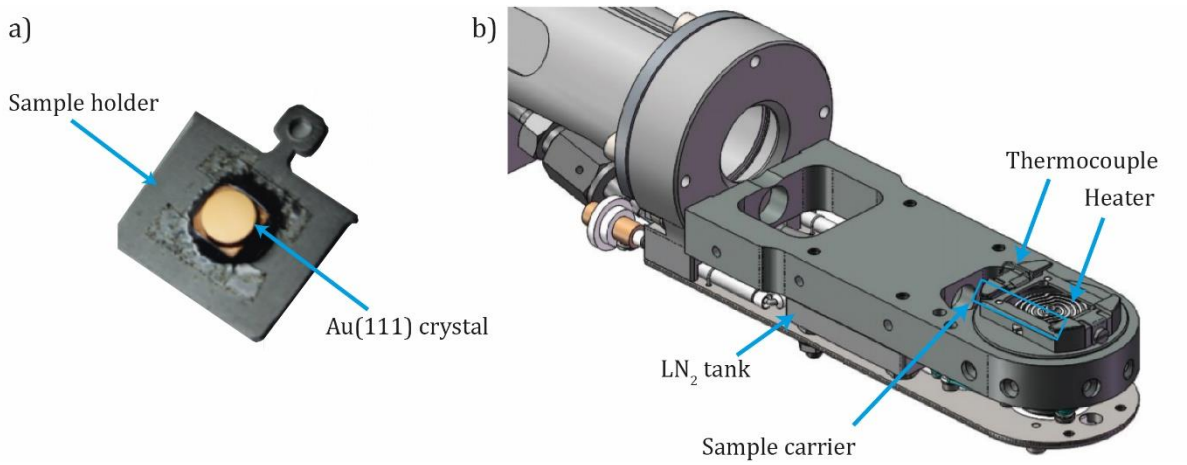

Figure 3-3. Photograph of Au(111) single-crystal welded to a sample holder and schematic image of the manipulator head

Evaporators

The samples are prepared after cleaning the substrate. Due to the variety of samples explored in the thesis, we have installed two different evaporators in the preparation chamber:

- **Metal Evaporator.** We have employed a QUAD evaporator from *MANTIS DEPOSITION LDT.* (see Figure 3.4a). Metals are evaporated by means of electron beam evaporation providing a vapor flux of the desired metal. This evaporator is equipped with 4 cells and it allows co-deposition of various metals from different cells at the same time. The evaporator admits the metal source to be either in the form of powder or a rod, the latter option being used by us. Every cell contains its own filament located close to the target metal. A specific DC voltage and current flows through the filament, which generates thermally emitted electrons from the filament that are accelerated against the metal rod by applying a potential difference between them, heating it up and leading to a controllable evaporation rate.

- **OMBE.** The organic precursors were evaporated by means of Organic Molecular Beam Epitaxy (OMBE), using a *KENTAX* TCE-BSC (see Figure 3.4b). This evaporator is equipped with 3 cells and allows the co-deposition of two precursors at the same time. The molecular precursors are usually in powder

form which are stored in quartz crucible specially designed for the KENTAX TCE-BSC model. The crucibles are introduced in the cells where the molecules will be sublimated by heating them up till they reach the sublimation temperature.

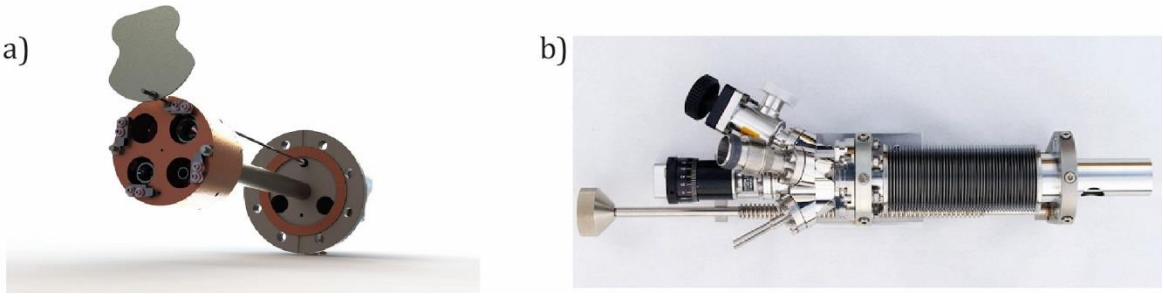

Figure 3-4. Electron Beam epitaxy evaporator and Organic Molecular Beam Epitaxy evaporator ***a)*** *E-Beam evaporator from Mantis.* ***b)*** *TCE-BSC OMBE evaporator from KENTAX.*

Quartz Crystal Microbalance (QCM)

The preparation chamber is equipped with a QCM from *INFICON*. It is composed by a single sensor quartz crystal that is oriented towards the evaporators in order to calibrate the evaporation rates and maximize the control over the prepared samples. The quartz crystal oscillates at a specific frequency, which is altered when small amounts of mass are deposited over it, providing direct information about the evaporation rate.

Quadrupole Mass Spectrometer (QMS)

The quadrupole provides information related to the residual gases present on the chamber. We have employed a 3F PIC quadrupole from *Hiden Analytical*. This technique allows to detect the presence of contaminants in the chamber and follow some reaction mechanisms detecting the products desorbed from the sample. Furthermore, this quadrupole model presents some extra advantages, as very low detection limit, large energy resolution and allows for ionization threshold scans to discern between compounds. It is designed with a special shroud to reduce indirect signal during thermal programmed desorption (TPD) measurements.

Low Energy Electron Diffraction (LEED)

The preparation chamber contains a BDL800IR-MCP2 electron diffractometer to perform low energy electron diffraction (LEED) from *OCI Vacuum Microengineering*. This technique gives information related to the crystallinity of the sample surfaces by means of bombardment with low energy electrons which are diffracted against a fluorescent screen where are observed as spots. The sample has to be orientated perpendicular to the LEED for a normal incidence of the electrons and with a working distance of 15 mm. In addition, this LEED model is equipped with two microchannel plates that enhance its sensitivity allowing operation conditions at lower emission currents and therefore avoiding damage to the samples.

3.1.3 Analysis chamber

The analysis chamber hosts a commercial *Omicron* LT nc-AFM/STM, comprising mainly the scanning probe microscope, the cryostats to cool down the sample to liquid helium temperature and a parking stage to host up to six samples.

Cryostats

All the results presented in this thesis were performed at 4 K due to the significant advantages of working at very low temperature. This set-up configuration allows to cool down the sample and the tip reducing the thermal broadening and increasing the energy resolution. Furthermore, the diffusion of most adsorbates is blocked at such temperatures.

The cryogenic set-up is based on two cryostats: the inner cryostat and the outer cryostat; with the outer cryostat concentric to the inner one. The inner cryostat is filled with liquid helium and it is in direct thermal contact with the sample. In addition, the outer cryostat is filled with liquid nitrogen for thermal insulation of the inner cryostat from RT, reducing the He evaporation from the inner cryostat. Importantly, each cryostat counts with a movable thermal shield to allow the insertion and removal of the samples from the STM sample stage and thermal insulate the STM head during the measurements. Figure 3.5 (insets 1 and 2) shows the inner cryostat with its corresponding shield, respectively.

Vibration Isolation System

The scanning probe measurements are very sensitive to vibrations. Therefore, the STM head includes an insulation system designed by *Omicron*. The STM system counts with 3 different positions: thermal contact (for cooling down the sample), stand-by and measurement position. At the measurement position the STM is suspended by three springs insulating the system from low frequency noises and from vibrations originated from the evaporation of the cryogenic liquids (inset 3 from Figure 3.5). The vibration of the STM stage hanging from the springs is damped by an eddy current mechanism (inset 4 from Figure 3.5), formed by the copper fins on the bottom of the STM stage and permanent magnets mounted inside the LHe heat shield (inset 2 from Figure 3.5).

It is important to notice that the scroll pumps are connected to the turbo pumps using flexible plastic hoses that contribute to reduce the transmission of the vibrations coming from the pumps, instead of using metal hoses. This allows to perform STM measurements with the primary pumps operating.

Finally, the whole system is insulated against external vibrations coming from building vibrations, persons or machines. To this aim the entire UHV system is supported by three AVI400-M/3/LP damping units from *HWL Scientific Instruments GmbH* that uses a feedback of stabilization from piezoelectric force motors.

STM Head

The samples are inserted in the STM stage (inset 5 from Figure 3.5), where they are supported by two rails. The sample holder has to be oriented with the welded facing the STM tip. The inner and outer shields are operated with a magnetic wobble stick, which also allows to insert and remove the samples.

Two different types of tips have been used in this thesis depending on the purpose of the measurements. i) The STM tips are prepared using tungsten wires of 0.25 mm of diameter by an electrochemically etching procedure, following the indications in the LT STM User´s Guide provided from *Scienta Omicron* (inset 8 of Figure 3.5). The so-prepared tip is inserted in the tip carrier tube, taking into account that the maximum length of the

tip outside the tip carrier should be 1.5 mm. ii) The Q-plus sensor tips are provided from *Scienta Omicron*, and consists of a quartz tuning fork sensor with a W tip attached (inset 7 of Figure 3.5). It is worth to highlight that a quartz tuning fork (Q-plus sensor) allows to acquire simultaneously in STM and nc-AFM mode.[76] The tuning fork system is mounted on a ceramic support and the attached W tip is electrically connected to the tip holder through a gold wire, allowing to measure the tunneling current.

The tip carrier (either of the STM tip or the Q-plus sensor) is magnetically attached by three legs on the sensor that are fixed on top of the piezoelectric tube (inset 6 from Figure 3.5). This piezoelectric tube is responsible of the fine movement of the tip while scanning. It is formed by a central electrode which allows the fine movement in *z*, allowing a *z*-resolution better than 0.01 nm. Four electrodes are surrounding the central tube in a cross-like geometry, which enables to control the fine movement of the tip in *x*,*y*. Applying certain values of voltage (controlled by the software) to the piezoelectric tube results in the compression or expansion of it due to the transformation of electric energy into mechanical energy.

The course motion allows the macroscopically movements of the tip. It consists of a slip-stick piezomotor located below the piezoelectric tube. The coarse motion in *Z* enables to approach or retract the tip with respect to the sample. The X_c and Y_c motions allow to scan different areas of the sample.

Finally, the set-up counts with a heater connected directly to the sample stage, since some experiments require measurements at variables temperatures.

Figure 3-5. Photographs of the Analysis Chamber components

1. Inner cryostat. 2. Inner shield. 3. Springs for vibrational insulation. 4. Damping Eddy current mechanism. 5. Sample stage. 6. Piezoelectric tube. 7. Q-plus sensor tip. 8. Etched W tip.

4. Nanostructured cobalt oxides

This chapter introduces the study of the geometry and the electronic structure of cobalt oxides nanoislands on Au(111) by means of STM and nc-AFM. Hereby, the cobalt oxide is presented as an anode model to be implemented in a photoelectrochemical cell for catalyzing the water splitting reaction. This work has been developed in the framework of the Artificial-Leaf project.[16] In addition, the obtained results are supported by DFT calculations performed by Prof. Núria López at *Institut Català d'Investigació Química* and the growth of the cobalt oxides has been performed thanks to a collaboration with Prof. Jeppe Lauritsen at *iNANO* (Aarhus, Denmark).

4.1 Photoelectrochemical cell: clean and renewable energy

The urgent need for designing novel sustainable alternatives to fossil fuels has led us to the development of new energy sources.[77] Nowadays, a great challenge for the society is to reproduce in a laboratory the photosynthesis process, being able to produce H_2 and solar fuels using the energy of the sun.[78]

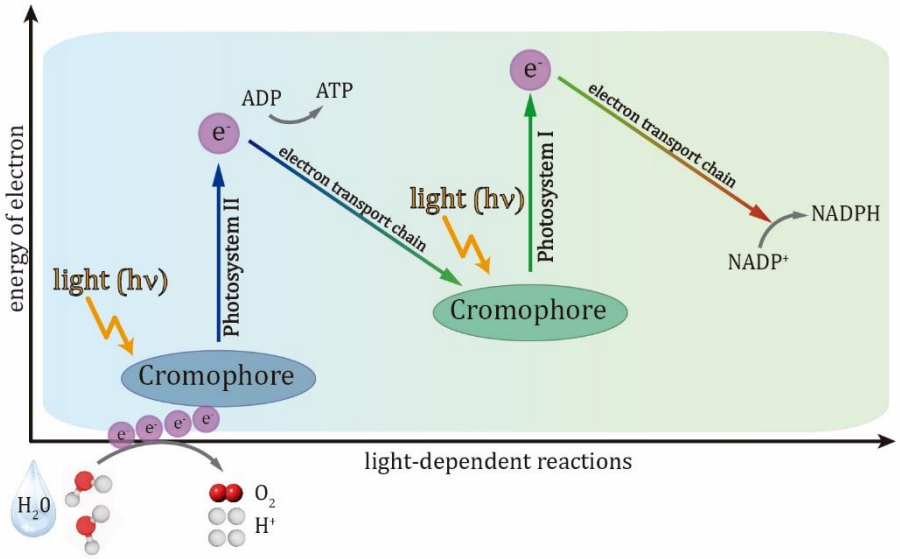

Figure 4-1. Photosynthesis scheme

A simplify scheme of the photosynthesis process is shown in Figure 4.1, where the chromophore of photosystem II absorbs the sunlight, boosting an electron to a higher

energy level initializing a charge transfer reaction, where energy is delivered. The electron is replaced by dissociating a water molecule, where in addition, O_2 and H^+ are generated. When the initial boosted electron arrives to the photosystem I, it replaces an electron that was previously boosted by energy absorption and was transferred to an acceptor molecule initializing a second electron transfer chain generating NADPH, which is used as chemical energy.[79] In conclusion, during the photosynthesis process, the solar energy is converted into chemical energy using the energy of the sun and water, which is the fundamental concept for the design of a photoelectrochemical cell (PEC) device.[80,81]

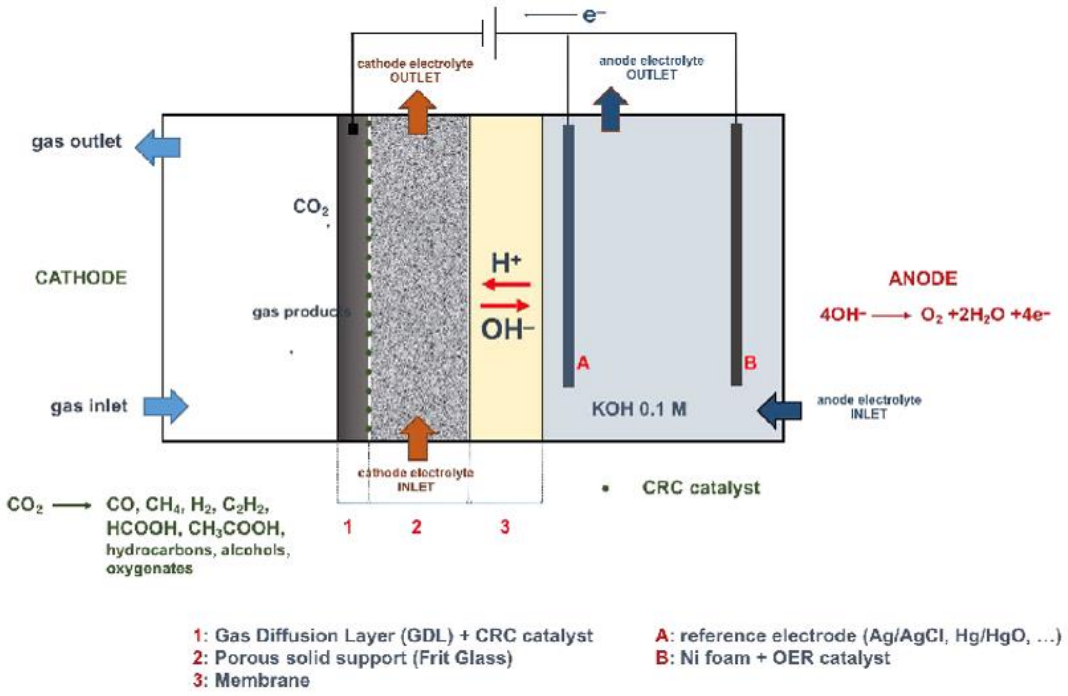

Figure 4-2. Photoelectrochemical cell prototype from A-Leaf

Based on the photosynthesis process, the Artificial-Leaf project is focused on the development of a PEC for direct transformation of water and CO_2, through the adsorption of solar energy, into O_2[82,83] and organic matter.[84,85] Figure 4.2 shows the design of the prototype presented by co-workers from the A-Leaf, where the H_2O is oxidized at the anode in an alkaline medium, delivering electrons transferred to the cathode and used for the reduction of CO_2 into fuels. The protons generated during the water splitting reaction flow to the cathode where the reduction reaction takes place using the

transferred electrons and producing H_2. The electrodes are separated by the electrolyte, which is an ionic conductor.

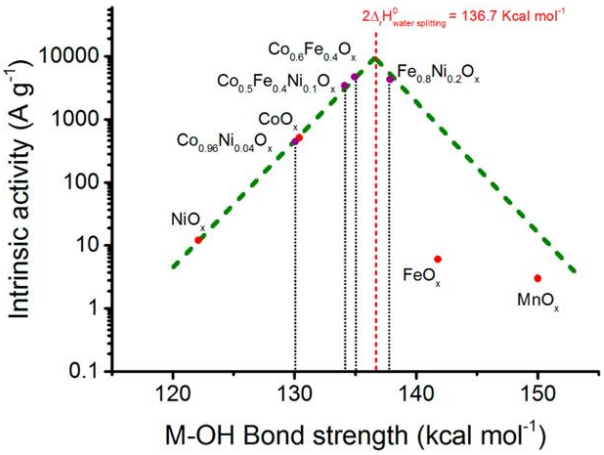

Figure 4-3. Volcano plot representing the intrinsic activity of TMO vs. the M-OH Bond Strength

Extracted from reference 86.

The design of the cell is divided into the different research groups participating in the A-Leaf project. Our role in this project is the development and study of an anode, from a fundamental point of view. The main requirements that the anode have to meet are: be stable in neutral to alkaline conditions and reduce the costs with respects to previous oxides employed (RuO_2 and IrO_x).[87–89] Following these requirements, 3d transition metal oxides (TMO) are considered promising candidates for catalyzing the water splitting reaction. Previous publications compare the intrinsic catalytic activity of different materials using the M-OH bond strength,[86] defined as the sum of the bond dissociation energies of a metal hydroxide, which is directly associated to the intrinsic energy of the oxy-hydroxide metal (the active phase of the oxide anode in electrochemical conditions for the water splitting).[90,91] In Figure 4.3 the volcano plot is shown, where the intrinsic activity of different transition metal oxides vs. the M-OH bond length is represented, revealing potential applications in catalysis for oxides based on Co, Ni and Fe.[86,92] The bond energy of these materials is similar to the energy necessary to dissociate two molecules of water. The purpose of study in this chapter is the cobalt oxide. We have explored the electronic properties and the atomic structure of this oxide and its catalytic activity at the atomic scale.

4.2 Cobalt oxide phases

Cobalt is a 3d transition metal with electron configuration: [Ar]$3d^7$ $4s^2$. Along the history, cobalt has been extensively used due to its characteristic blue color. Nowadays, it is mainly used in catalysis with important applications in the efficient and selective synthesis of important organic materials.[93] Furthermore, cobalt-based oxides present a wide variety of applications for energy storage,[94] where the oxidation state of cobalt can be tuned forming complex structures with a large variety of applications.[95]

Table 4-1. Cobalt oxide bulk phases

Cobalt oxide phases: spinel,[96] rock-salt,[97] wurzite,[97] corundum[95] and $LiCoO_2$.[98]

Structure	Composition	Cobalt	Oxygen
Spinel	Co_3O_4	¼ h_t Co^{2+} and ½ h_o Co^{3+}	O^{2-} (fcc)
Rock-salt	c-CoO	h_o Co^{2+}	O^{2-} (fcc)
Wurtzite	h-CoO	½ h_t Co^{2+}	O^{2-} (hcp)
Corundum	Co_2O_3	2/3 h_o Co^{3+}	O^{2-} (hcp)
LT-$LiCoO_2$	CoO_2	Co^{3+} (Li^+)	O^{2-} (cubic spinel structure)
HT-$LiCoO_2$	CoO_2	Co^{3+} (Li^+)	O^{2-} (rhombohedral stratified layers)

Different cobalt oxide phases containing Co^0, Co^{2+}, Co^{3+} or a mixture of them are known. Table 4.1 summarizes the most common cobalt oxide structures, where the most thermodynamically stable phases are Co_3O_4[96] and c-CoO.[97,99] The versatile properties of cobalt oxides rest in their atomic structures.

In this chapter, we have studied the atomic structure and the electronic properties of the prepared cobalt oxide nanoislands on Au(111), as model systems, employing different surface techniques.

The growth of the sample was carried out following a recipe consisting in the evaporation of cobalt from an outgassed rod of 4 mm by means of electron beam evaporation on a pristine Au(111) surface held at 360-380 K under an oxygen atmosphere.[100,101] The most sensitive parameters during the growth of the sample are: i) the temperature of the substrate and ii) the oxygen environment.

(i) On one hand, over-heating the sample during the growth of CoO implies the partial desorption of the oxygen, forming cobalt clusters.[102] On the other hand, if the temperature is below to 360 K the atoms are not able to diffuse over the surface and form large islands, therefore small nucleation centers on the surface are observed.

(ii) The oxygen atmosphere plays a crucial role in the oxidation state of the cobalt.[103] Tuning this parameter, we are able to control the stoichiometry. The XPS measurements together with the STM images in Figure 4.4 reveal the presence of two main type of islands: maintaining the oxygen pressure around 10^{-6} mbar the Co^{2+} predominates forming CoO bilayers; at oxygen pressures of 10^{-5} mbar we observe how partial amount of cobalt is oxidized to Co^{3+} growing Co_2O_3 islands (trilayers) and multilayers combining Co^{2+} and Co^{3+} which suggests the growth of spinel structures.

XPS measurements of metallic cobalt on Au(111) were acquired as reference (black spectrum in Figure 4.4). As mentioned above, higher oxygen pressure during the growth of the sample implies higher oxidation state of the cobalt.[103] Figure 4.4 shows two distinct samples at oxygen atmosphere of 10^{-6} mbar (red spectrum) and at 10^{-5} mbar (blue spectrum). We observe the emergence of characteristic satellites related to the presence of Co^{2+} at binding energies of 786 eV and 804 eV[104] for the sample at $P_{O2} = 10^{-6}$ mbar grown, which, together with the STM images, confirms the formation of the CoO phase. It is worth to mention that the positions of the peaks have not been

extensively investigated due to the effect of the substrate interacting with the cobalt oxide islands that could shift the values of the binding energy with respect to bulk or thin films oxides.[105]

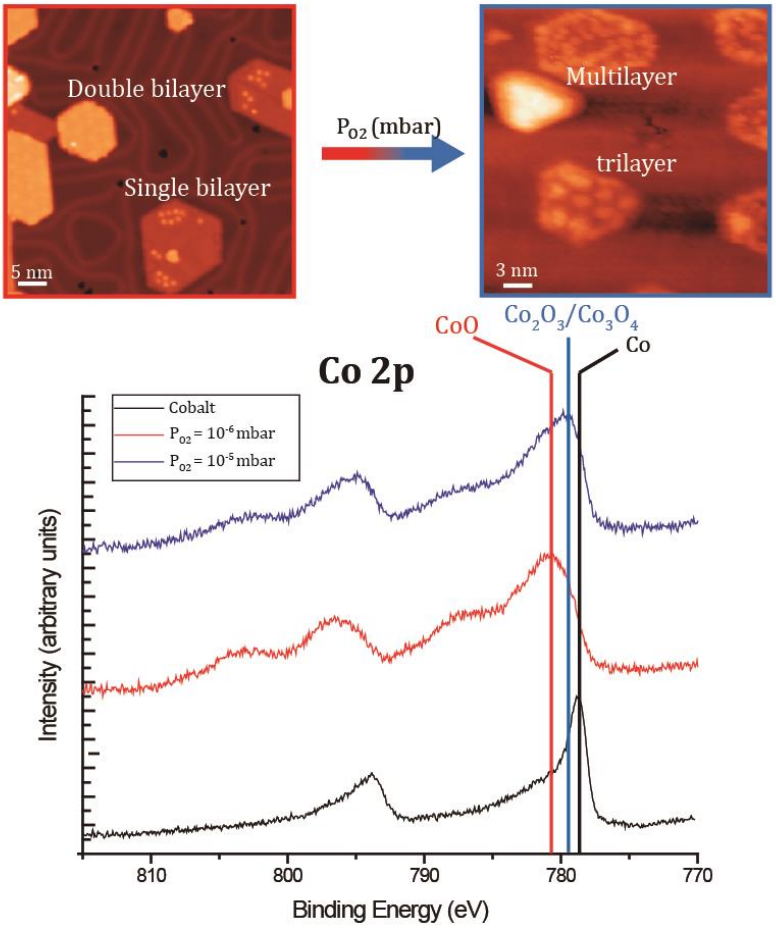

Figure 4-4. XPS measurements of Cobalt oxides grown under different oxygen atmospheres

We find that samples prepared at higher oxygen pressures give rise to more irregular islands with a mixture of phases, where islands with hexagonal or triangular shape and different thickness are observed. Multilayer islands show large thickness and are difficult to study by STM, where conductance between sample and tip is needed. In addition, at lower oxygen pressure, CoO bilayers are formed with a cobalt-oxygen layered structure from bottom to top. The simplest structure of this CoO is the single bilayer structure (Au-Co-O),[101,103,106] which is the predominant phase observed at lower oxygen pressure. The single bilayer phase presents advantages for the water splitting reaction due to the

affinity of water to the upper oxygen layer, inducing the water splitting reaction and the formation of oxy-hydroxyl cobalt (III) (the active phase).[107]

Finally, the metallic substrate employed for this experiments is Au(111), which favors the hexagonal lattice growth of the c-CoO (111). In this work we have investigated the well-known synergy effect between the cobalt oxide and the gold at the atomic scale, which has been reported in electrochemical conditions with promising results, though its nature is still unknown.[108,109]

4.3 Single bilayer CoO islands on Au(111)

The prepared nanoislands of CoO on Au(111) show a diameter ranging from 10 to 20 nm. Hereby, we observe the presence of a predominant structure: the single bilayer. It is formed by a cobalt layer covered by an oxygen layer (as previously reported).[95,101] Figure 4.5a shows an overview image where a majority of single bilayer islands is clearly observed, presenting a characteristic moiré pattern better visualized at negative bias voltages (Figure 4.5c). In addition, some islands present brighter areas that correspond to a double bilayer structure (Co-O-Co-O). Figure 4.5d shows a STM image of a double bilayer CoO island.

Here, we have focused on the study of the single bilayer. As mentioned above, such structure features a characteristic moiré pattern with a periodicity of (34 ± 2) Å. It is worth to mention that the presence of bright lines are typically observed in the single bilayer structures (highlighted with a blue circle in Figure 4.5a-c), which are assigned to atoms raw dislocations caused by an excess of oxygen. These dislocations induce a local change in the lattice, from hexagonal to tetragonal.[110]

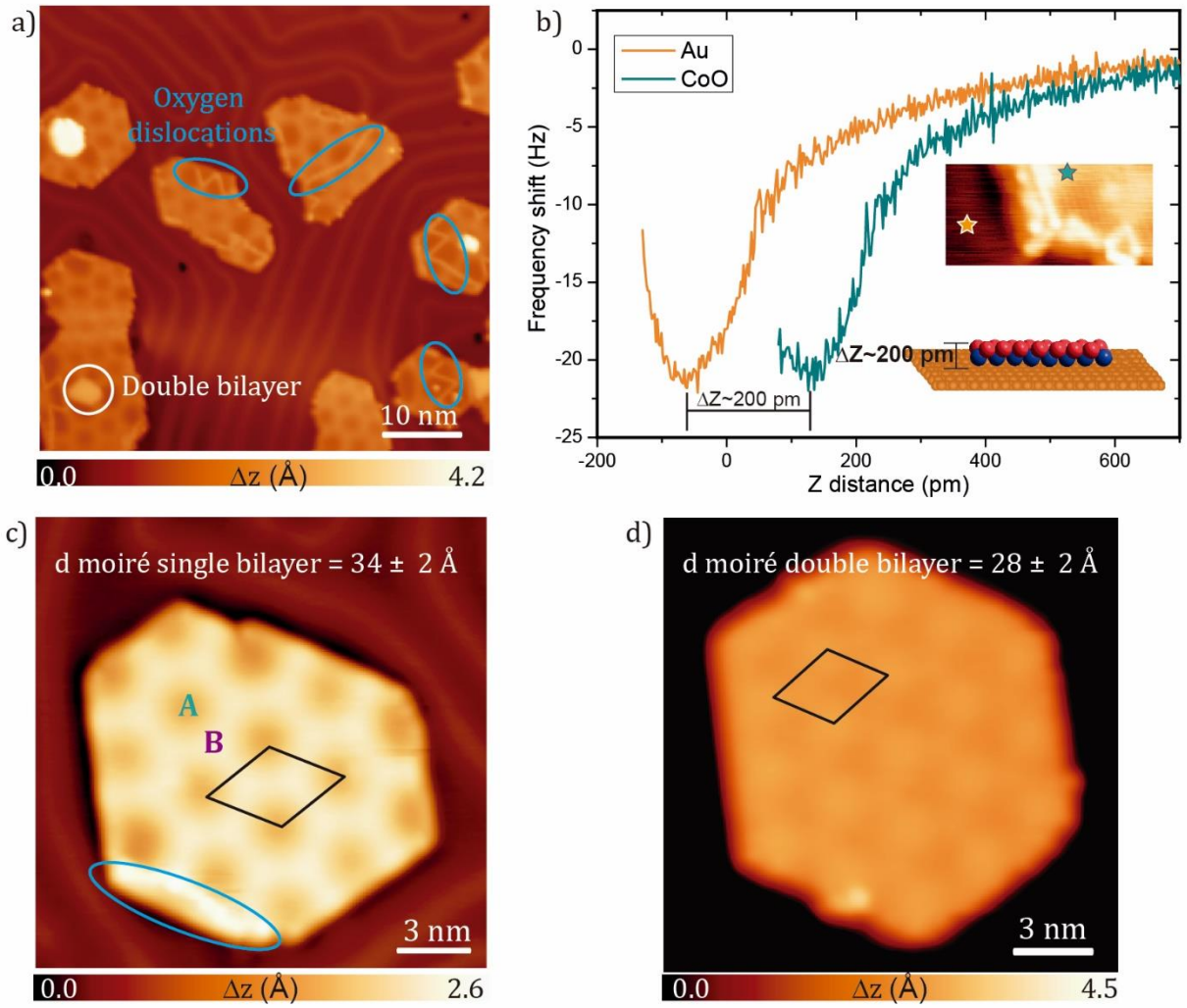

Figure 4-5. STM images of CoO nanoislands on Au(111)

a) *STM overview image of CoO single bilayer islands on Au(111) (V_b = -1.0 V and I_t = 100 pA).* ***b)*** *Force Spectroscopy measurements taken at the Au(111) (orange line) and the Top moiré of the CoO (green line).* ***c)*** *High resolution STM image of a single bilayer showing the presence of the moiré pattern (V_b = -1.0 V and I_t = 100 pA).* ***d)*** *STM image of a double bilayer island (V_b = 1.0 V and I_t = 100 pA).*

Importantly, two different areas are distinguished within the moiré pattern at negative bias: a dark and a bright area, which are termed as moiré region A and moiré region B, as we will explain latter.

Previous works reporting the formation of this phase were performed by STM.[100,101,103,106] These works reveal the existence of different structures (single and double bilayer, trilayer and multilayer) and their chemical composition. However, there is a lack of knowledge related to the electronic properties of these oxides and their geometry.

To complement STM, atomic force microscopy has emerged as a powerful technique to study metal oxide surfaces, being capable to provide information related to the chemical composition, defects or roughness.[111] Here, we have exploited such technique to investigate the heights of the CoO islands *via* force spectroscopy. In Figure 4.5c the force spectra acquired on top of Au(111) (orange line) as reference and on top of a CoO island (green line) are represented. The height of the cobalt oxide with respect to the substrate (Δz) is obtained by measuring the distance between the minima frequency shift values of the two spectra, which results in a single bilayer CoO height of Δz = (200 ± 20) pm. Such result is in agreement with the heights of other metal supported oxides, such as FeO[112] or ZnO.[113]

In order to inspect the atomic periodicity of the CoO surface, Low Energy Electron Diffraction (LEED) was performed. Figure 4.6a shows a LEED image of a CoO island on Au(111). Two different hexagonal lattices are found: the large pattern corresponds to the Au(111) and the short one to the CoO. The relation between such patterns provides the inverse of the relation between the Au(111) and the CoO lattices in real space, and hence, an average value of the interatomic distance of the CoO can be calculated. The relation factor between the CoO lattice and the substrate is $\frac{d_{CoO}}{d_{Au(111)}} = 1.2 \pm 0.3$. Therefore, we obtain an average value of d_{CoO} of (3.4 ± 0.3) Å, considering $d_{Au(111)}$ = 2.89 Å.

Next, we have investigated the structure of the CoO at the atomic scale by means of STM. Figure 4.6d shows a high-resolution constant-current STM image with atomic resolution that reveals a bond length of (3.3 ± 0.2) Å, which perfectly matches with the LEED value and previous STM experiments.[103]

It is worth to highlight that the moiré pattern periodicity is misaligned with respect of the high symmetry directions of the CoO. Therefore, the nature of the moiré pattern is the superposition of two different lattices with different orientations. The moiré pattern region corresponds to an incommensurate area with respect to the metallic substrate. Though the angle rotation seems to be really small, it can be measured in the STM images due to the magnification effect of the periodicity of the moiré pattern. Figure 4.6b reveals an angle of the moiré with respect to CoO of $\varphi_{CoO,moiré}$ = (5 ± 1)°. As mentioned above,

the rotation of the moiré with respect the CoO implies also a misalignment between the CoO and the Au(111). Such a misalignment cannot be detected in the LEED measurements because of the small value of the angle, resulting the LEED pattern in a single convoluted spot. However, we can calculate such value by exploiting the reciprocal space, taking advantage of the relation of the reciprocal vectors:[114]

$$\vec{k}_{moiré} = \vec{k}_{Au(111)} - \vec{k}_{CoO} \tag{4.1}$$

Importantly, Equation 4.1 can be approximated into Equation 4.2 due to the small values of the rotation angles ($\varphi_{CoO,moiré}$ and $\varphi_{CoO,Au}$):

$$\varphi_{CoO,Au} = \frac{k_{\mathrm{CoO}} - k_{\mathrm{Au(111)}}}{k_{\mathrm{CoO}}} \varphi_{CoO,moiré} \tag{4.2}$$

where $K_x = \frac{2\pi}{d_x}$.

Taking into account the obtained experimental values, we can determine a rotation angle between the oxide and the substrate of $\varphi_{CoO,Au} = 0.5°$.

Next, combining these results, we are capable to replicate an atomistic model of the c-CoO(111) on Au(111), which is displayed in Figure 4.6e. Such model is partially in agreement with the one proposed by M. Li and E. I Altman, which includes the same number of atoms per unit cell of the moiré pattern.[115] Our model is the result of the superposition of: i) Au(111) layer with a bond length of 2.89 Å, ii) the CoO layer with unit parameter of 3.17 Å, iii) and the rotation of the CoO layer 0.5º with respect to the Au(111).

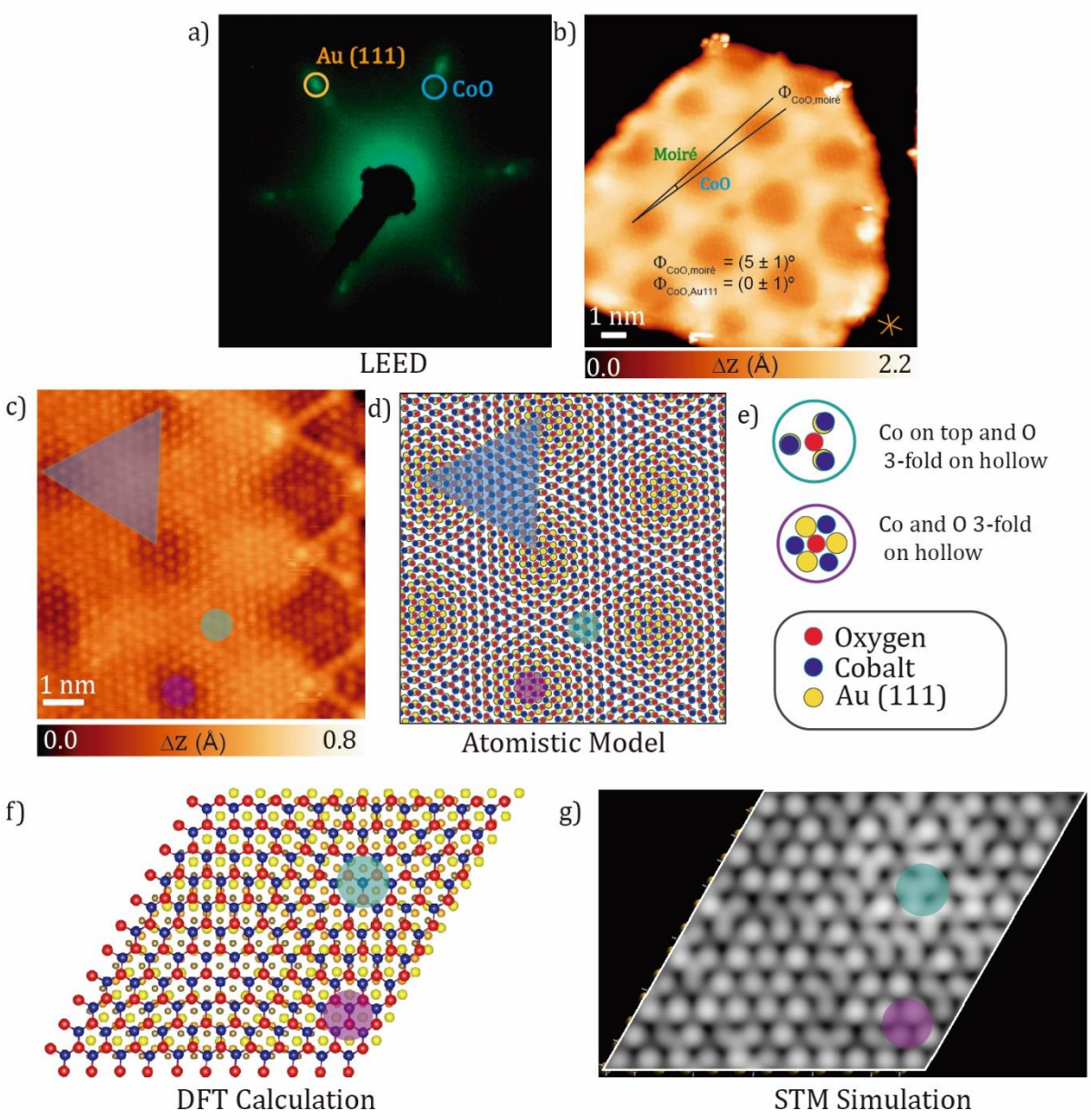

Figure 4-6. Characterization of the atomistic structure of moiré pattern

a) *LEED image acquired at energy = 58.1 eV.* ***b)*** *High-Resolution STM image showing the misalignment between the CoO high symmetry direction and the moiré pattern periodicity (V_b = -1 mV, I_t = 750 pA).* ***c)*** *High-Resolution STM image with atomic resolution of the CoO single bilayer. Blue and purple circles correspond to the moiré region A and moiré region B, respectively (V_b = -1 mV, I_t = 700 pA).* ***d)*** *Atomistic model of CoO single bilayer on one layer of Au(111) based on experimental results.* ***e)*** *Amplification of the atomic structure of the different moiré areas.* ***f)*** *and* ***g)*** *DFT simulation showing the relaxed model and the simulated constant-current STM image of the occupied states.*

We observed minor differences in the bond length of the moiré region B and the moiré region A in the high-resolution STM images (Figure 4.6c shows the moiré region B and the moiré region A in purple and cyan highlighted, respectively). Similarly, these variations were found in the DFT calculations and allow us to assign the local structures

to the areas found in the moiré pattern. Comparing these variations between the regions A and B of the moiré in the DFT calculations (Figure 4.6g) and experimental STM images (Figure 4.6h), we find that the region A corresponds to the structure with the Co on top of the Au atoms and the oxygen in 3-fold hollow positions (green circle in Figure 4.6), and the region B to Co and O atoms in 3-fold hollow positions with respect the Au (purple circle in Figure 4.6). The experimental values, DFT calculations and the local structure are summarized in Table 4.2.

Table 4-2. Comparison of the bond lengths of the top and bottom moiré areas obtained by DFT calculations and experimental results

DFT Calculations (Å)	**Experimental Data** (Å)	**Moiré area**	**Local Structure**
3.20	3.30	Moiré region A	
3.16	3.25	Moiré region B	

Next, we have studied the roughness of the moiré pattern of the CoO islands in order to investigate the role of the substrate and its interaction with the CoO nanostructures. Previous works make a direct relation between the roughness and the interaction with the substrate that is taking place, such as graphene on iridium[116] (weak interaction) or graphene on ruthenium (strong interaction mediated by covalent bonds).[117] Hereby, we have inspected the roughness of the moiré pattern of the CoO *via* force spectroscopy, in order to unravel topographic and electronic effects. In Figure 4.7a force spectra acquired on top of different positions of the moiré are represented (positions depicted in Figure 4.7c). Such spectra evidence the variation of the tip height (Δz) at the frequency shift minima between the different areas, which suggests a corrugation of the moiré pattern of ≈ 30 pm. However, the obtained roughness following this protocol that requires constant-height operation is within the reported intrinsic error value.

In order to overcome such limitation, N. J Van der Heiden and coworkers proposed an alternative to investigate the chemical composition and geometry using nc-AFM.[118,119] It

is worth to mention the existence of different works oriented to explore the possibilities offered by nc-AFM.[120,121] Motivated by such works, we have acquired several constant-height frequency shift AFM images at 5 pm, increasing tip-sample distance from -110 to -285 pm (marked in the blue square in Figure 4.7a). The values of Δf obtained in every single pixel of the images at different heights were fitted to a quadratic function. Extracting the values of the frequency shift minima and its tip height we can represent Δz_{min} (Figure 4.7d) and Δf_{min} (Figure 4.7e) maps. Drawing a height profile in Δz_{min}, we can extract the variation of the tip height for the minima values of frequency shift with spatial resolution. Figure 4.7b shows the height profiles draw in the same area in the STM image (Figure 4.7c) and in the Δz_{min} map. As mentioned above, the heights measured by STM are a convolution between LDOS and topography, consequently the blue height profile represents apparent heights, which strongly depends on the acquisition parameters of the image, mainly on the bias voltage. The red height profile acquired by the nc-AFM technique allows us to discern more realistic heights, revealing a roughness of $\sim$ 0.3 Å, which matches well with the force spectroscopy measurements. Here, to be fair, we have to consider that nc-AFM measurements over moiré patterns could be affected by a variation of the nature of the forces within the moiré, inducing some degree of error in our measurements,[111] though in any case, they are more precise than STM profiles.

Interestingly, when measured at negative bias voltage, the moiré region A (brightest area at $V_b < 0$) appears higher than the moiré region B (darkest area at $V_b < 0$), even though nc-AFM measurements reveal that it is topographically lower. Later, we will discuss the nature of this effect related to the electronic structure of the moiré pattern.

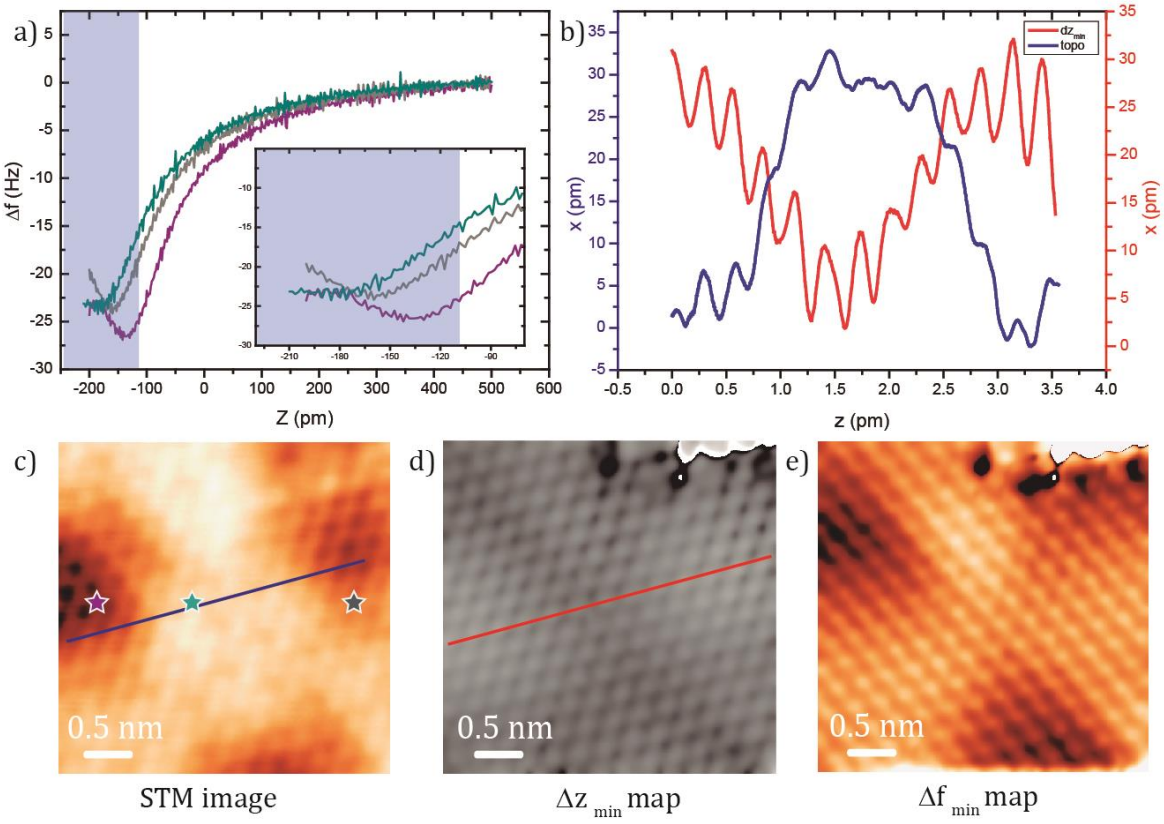

Figure 4-7. Corrugation of the moiré pattern

a) *Δf(z) curves obtained over the positions indicated in* ***c)***. ***b)*** *Height profiles along the blue line in* ***c)*** *showing the apparent height by STM and along the red line in* ***d)*** *revealing the corrugation of the moiré.* ***c)*** *STM image of the moiré pattern of CoO/Au111 (V_b= 5 mV, I_t= 5 pA).* ***d)*** *Its corresponding Δz_{min} map.* ***e)*** *Its corresponding Δf_{min} map.*

The real corrugation measured for the oxide provides indirect information related to the hybridization of the CoO with the Au(111), where small deviations lead to stronger or weaker interactions. As mentioned before, such interactions alter the electronic properties and, as a consequence, the catalytic activity of the oxide towards the water splitting. Here, the electronic properties of the single bilayer island and the effect of the moiré pattern were investigated by means of STS measurements, where dI/dV spectra at 4 K on top the highest (moiré region B) and the lowest (moiré region A) areas of the CoO were acquired. The spectra plotted in Figure 4.8a reveal a slight difference in the LDOS between these two areas. The blue arrows indicate the increase in the density of states found close to the Fermi energy in both areas (spectra are vertical plotted for better visualization).

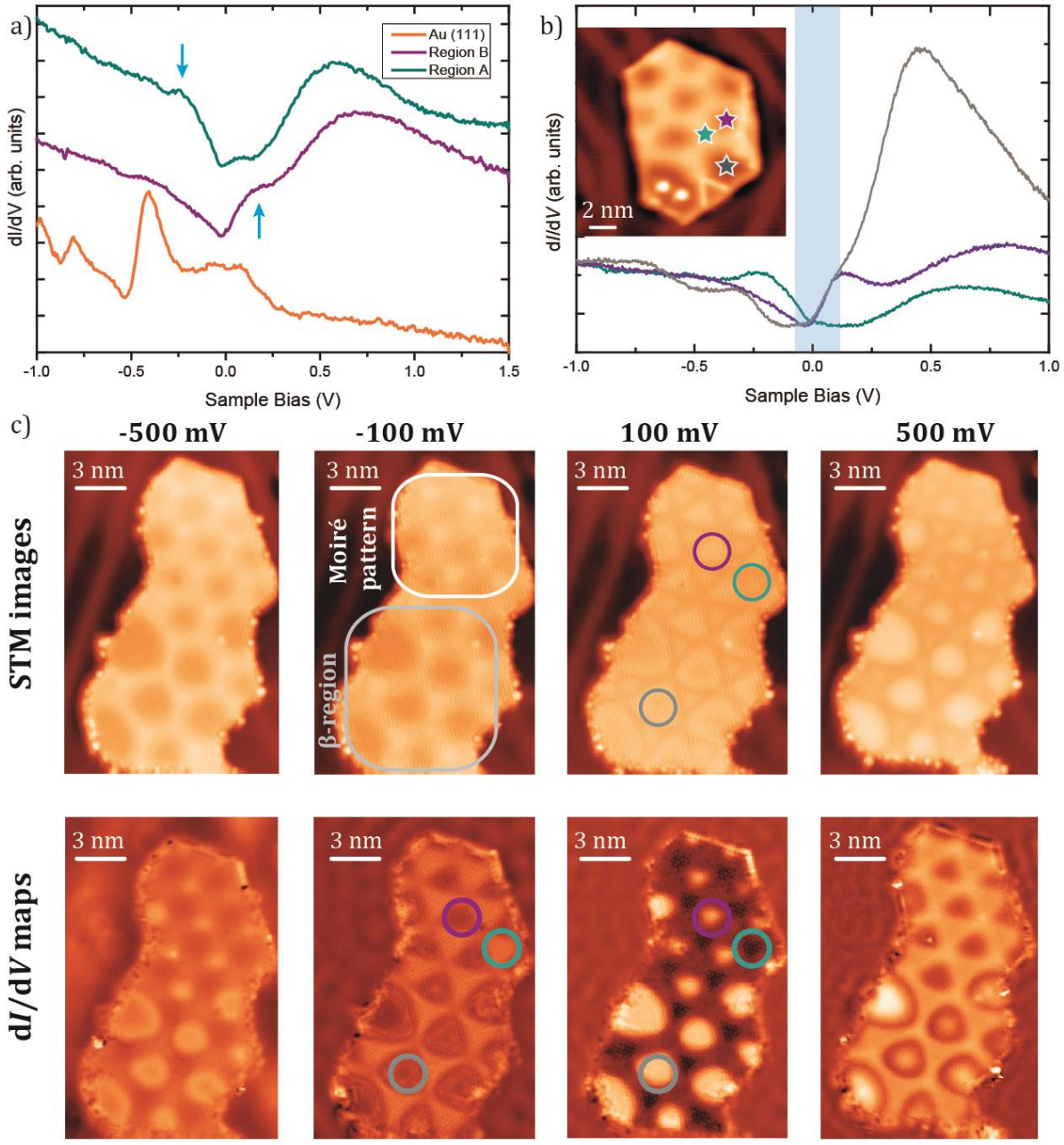

Figure 4-8. Electronic properties of CoO single bilayer islands on Au(111)

a) *dI/dV curves acquired on STM on top of the region B (purple curve) and region A (green curve) (vertical translation for better visualization).* ***b)*** *dI/dV curves acquired on the positions depicted in the inserted STM image for comparison of β-region and moiré areas.* ***c)*** *STM images and corresponding dI/dV maps at -500 mV, -100 mV, +100 mV and +500 mV, respectively. The moiré region B is marked in a purple circle, the moiré region A in a green circle and the β-region in a gray circle.*

The periodically modulated electronic structure of the moiré pattern is better visualized in the constant-current dI/dV maps displayed in Figure 4.8c. These maps were acquired with a CO-functionalized tip, which enhances the resolution resolving the atomistic

structure. The dI/dV map acquired at -100 mV shows higher occupied LDOS in the moiré region A (green curve), suggesting a stronger hybridization of this area with the substrate.[121] Tentatively, a charge transfer could take place where electrons are transferred from the gold substrate to the moiré region A.[117] This effect is favored in the moiré region A due to a geometric effect, being this area at lower height and therefore, closer to the substrate. The increase in the occupied LDOS sustains the results obtained in the measurements of the apparent height by STM at negative bias voltage: the moiré pattern is better visualized at negative voltages, where the LDOS is larger at the moiré region A and therefore this area seems to be higher.

Notably, dI/dV maps shows a different region, not identified in the topographic images. The dI/dV map acquired at 100 mV reveals brighter areas (gray circle) at the bottom of the island, which constitutes a region with distinct electronic structure. The dI/dV spectra show that the electronic properties of this new region, never reported before and from now on named β-region, are completely different to the moiré pattern region. The dI/dV curve acquired on top of the β-region is represented in Figure 4.8b (gray line), together with the spectra acquired on the region B (purple line) and A (green line) of the moiré pattern. Such curve, recorded on the β-region, shows higher density of unoccupied states with respect to the rest of the CoO islands, both in the regions A and B. It is worth mentioning that we find some similarities, both in the resolution of the STM images and in the electronic structure at positive bias close to the Fermi energy (marked in the blue circle in Figure 4.8b), between the bottom moiré area and the β-region.

In addition, it was observed that the chemical reactivity of the β-region is different, showing more affinity to the contaminants and residual gas present in the UHV chamber. Such contaminants appear as bright protrusions attached to the CoO surface (observed in the inset STM image in Figure 4.8c), being only present on the β-region. Tip manipulation allows us to move the adsorbates between different locations at the β-region and even from different islands, although it was not possible to move them to the moiré pattern region. These adsorbates, found attached to the β-region, are tentatively assigned to water molecules considered as contaminants, coming from the UHV chamber.[122]

Once the β-region was recognized in the system, the next goal was to explore its nature. Figure 4.9a shows a HR-STM image with atomic resolution containing all the regions, allowing a direct comparison between them. We found that the β-region corresponds to a compression of the moiré region, where its atoms show a shorter interatomic distance of ~ 3.0 Å (with respect to the 3.3 Å found in the normal moiré region). In Figure 4.9b the height profiles drawn along the moiré region A (green line), the moiré region B (purple line) and the β-region (gray line) are plotted in order to compare their atomic periodicities. Herein, we can compare the decrease in the atomic periodicity in the β-region, despite its hexagonal lattice is intact. As a result, we conclude that there is a compression in the bond length of ~ 9% in the β-region that modifies the electronic properties and the chemical reactivity of the CoO island resulting in a new phase.

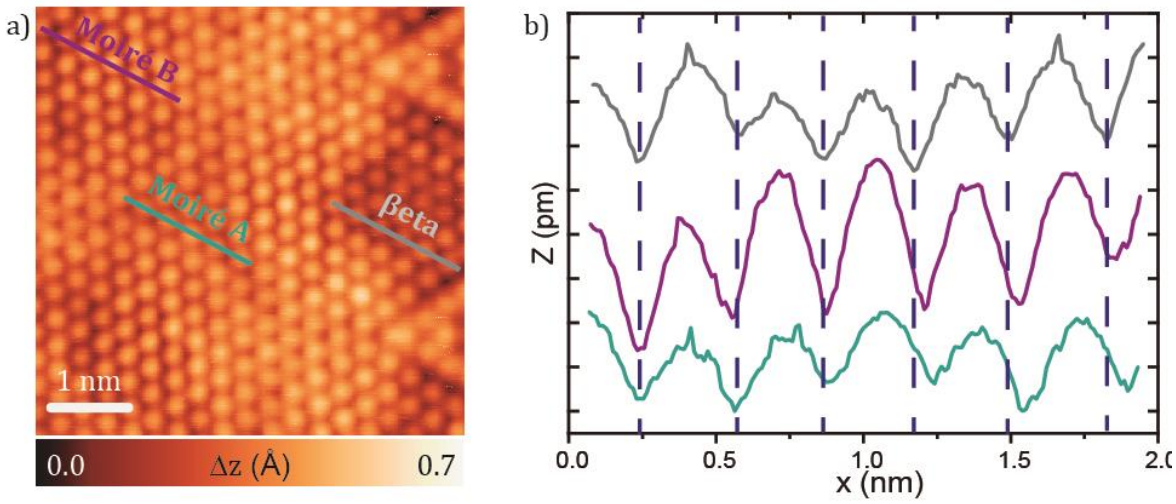

Figure 4-9. Atomistic comparison between the moiré pattern and the β-region

a) *High-Resolution STM image with atomic resolution of moiré region A, B and β-region (V_b = -3 mV, I_t = 700 pA).* ***b)*** *Height profiles extracted from* ***a)*** *plotted in stack of moiré region A (green line) with the longest bond length, moiré region B (purple line) with slight shorter bond length and β-region (gray line) with the shortest bond length.*

The absence of a moiré pattern in the β-region suggests the match between the CoO and the substrate. In addition, bond distances measured in the β-region exhibit values close to that reported for the Au(111) lattice. Taking into consideration the analogies found in the topography and in the electronic properties between the moiré region B and the β-region, we establish a relation between them. Then, we propose that the β-region corresponds to a local bottom area (Co and O in 3-fold with the substrate) that follows a hexagonal lattice commensurate with the Au(111).

We observed that the β-region tends to appear adjacent to the edges of the islands. The appearance in the topographic images of the β-region is similar to the moiré region B, though it could be larger in size. The extension of the β-region varies in every single island. It is shown in Figure 4.10 how the extension of the β-region can be modified from being a small region, identified by the attachments of the adsorbates (Figure 4.10a), to cover half of the island (Figure 4.10b) or up to be the unique region found in the island (Figure 4.10c). Several samples were grown varying the parameters (substrate temperature, flux evaporation, oxygen pressure, post-annealing…). Nevertheless, a protocol for controlling the extension of the β-region was not found.

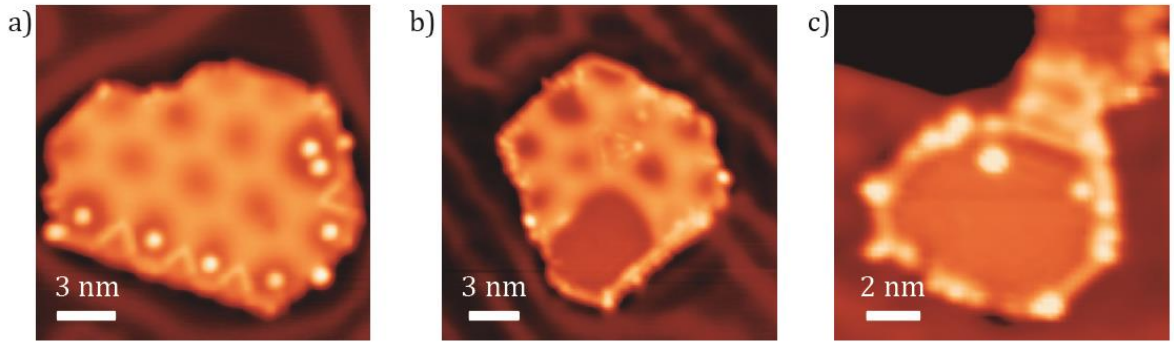

Figure 4-10. STM images of CoO islands composed by β-region

a) *CoO island partially formed by β-region (V_b = -1.0 V, I_t = 150 pA).* ***b)*** *Half covered by β-region (V_b = -0.2 V, I_t = 500 pA),* ***c)*** *Entirely formed by β-region (V_b = -0.1 V, I_t = 100 pA).*

In summary, we have demonstrated the effect of the atomic structure on the electronic properties of the oxide, which also determines its reactivity. Next, we have inspected the correlation between these two phases of the c-CoO with respect to the registry with the Au(111) substrate.

4.4 Field-induced change of the atomic and electronic structure of CoO

The observation of the β-region reveals the versatility of the CoO and demonstrates the possibility of tuning its properties at the atomic scale. However, as mentioned before, we could not optimize the parameters for controlling the extension of the β-region. Motivated by other works, where transitions between different polymorphs have been induced by tip manipulation, we decided to assess the tunability of the phases found above. In this sense, it is worth to mention that there are phases of different materials

(TMS, TMO…) that can be induced by external stimuli, for example by electric field-induced manipulation.[123–125]

As a consequence of the applied bias voltage and the short distance between the tip and the surface, a considerable electric field in the tunneling junction can be created. The extension of the generated electric field varies for different tips, depending on the distribution of the tip apex, reaching up to hundreds of nanometers.[126,127]

Motivated by the previous mentioned works, we have inspected if we were able to induce the transformation for our system from moiré pattern region into β-region and vice versa. First, we spontaneously induced the modification acquiring LDOS spectroscopy from +1.5 V to -1 V stabilizing the tip at 1.5 V and 500 pA on top of the blue star in Figure 4.11a**.** When the voltage value reached close to -1 V, we observed a non-negligible variation in the $I(V)$, plotted in Figure 4.11c**,** which can be tentatively attributed to a change in the island or a modification at the apex of the tip. The tip remained topographically unaltered. In addition, $\mathrm{d}I/\mathrm{d}V$ curves were acquired on top of gold, before and after the variation in the $I(V)$, confirming that the tip did not suffer any variation. However, the appearance of the island (Figure 4.11b), as well as its electronic structure were modified. We show in Figure 4.11d the $\mathrm{d}I/\mathrm{d}V$ maps at -100 mV and +100 mV of the modified island, where the transformation into β-region coexisting with moiré regions A is clearly observed.

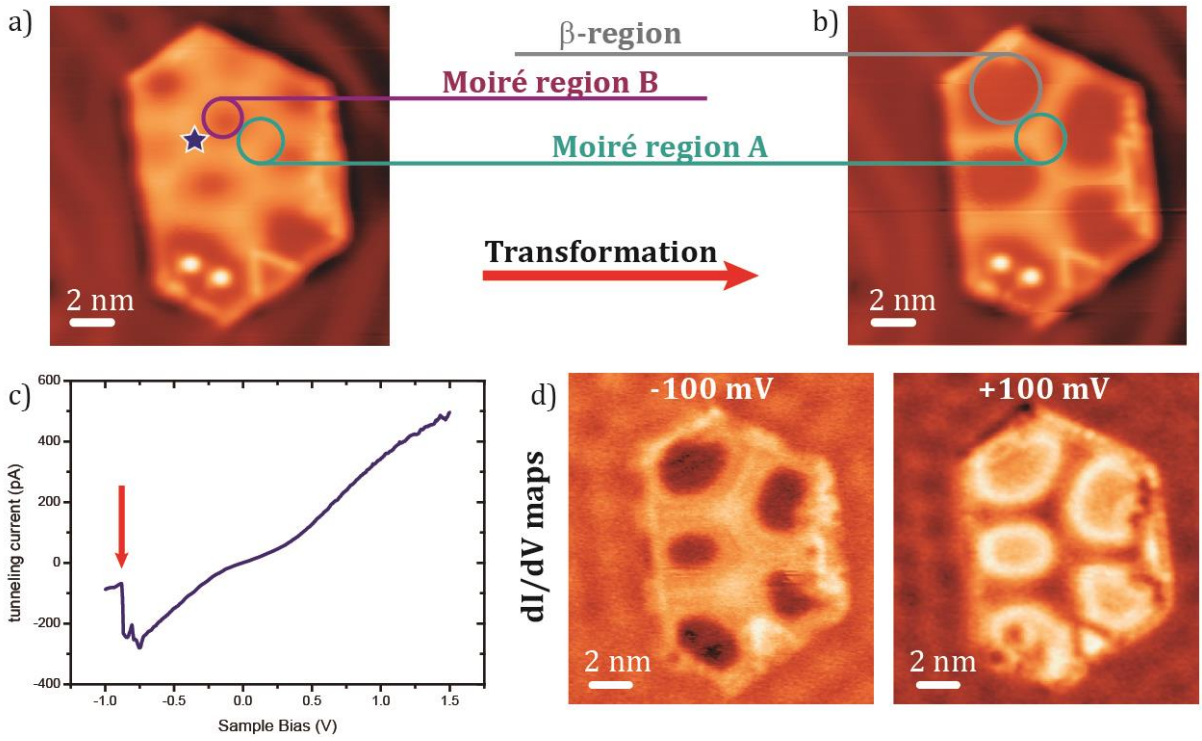

Figure 4-11. Modification of single bilayer CoO island

a) *Constant-current STM image of a CoO island before induce the transformation (V_b = -0.4 V, I_t = 500 pA).* ***b)*** *Constant-current STM image of the modified island (V_b = -0.5 V, I_t = 500 pA).* ***c)*** *The I(V) spectrum showing an abrupt change assigned to the island transformation (tip stabilize on top of the blue star at 1.5 V and 500 pA).* ***d)*** *Constant-current dI/dV maps of the modified island displayed in* ***b)****. (Left map: V_b = -0.1 V and It = 250 pA. Right map: V_b = 0.1 V and It = 250 pA).*

So far, we have proven that we can induce the transformation of the whole island from the moiré pattern into the β-region. Next, we decided to look into the atomic reorganization that is taking place in an island after such modification, comparing it with the initial structure. Therefore, we explored a new island (Figure 4.12a) characterizing it with a CO-functionalized tip (Figure 4.12b) in order to carry out a detailed study of the atomic lattice. Several voltage pulses were applied on top of the red mark in Figure 4.12a-b and, after applying every voltage pulse, the status of the island was checked. Finally, the modification of the island was induced by applying -8 V pulse. Surprisingly, the transformation took place at the border of the islands, ~ 1 nm away from the tip position (Figure 4.12c), so we conclude that the nature of this transformation is mainly induced by electric field.

Once the island was modified, we characterized it again with a CO-functionalized tip using similar parameters (Figure 4.12d). For easier comparison, we have drawn height

profiles at the same atoms row before (Figure 4.12b) and after the transformation (Figure 4.12d). The height profiles are plotted in Figure 4.12e, where we observe clearly a ~ 9 % compression of the atoms. Furthermore, we observe the creation of a vacancy in the adjacent border of the island, marked with a blue circle in Figure 4.12d**,** which could appear as a consequence of the atomic compression or just due to the voltage pulse applied.

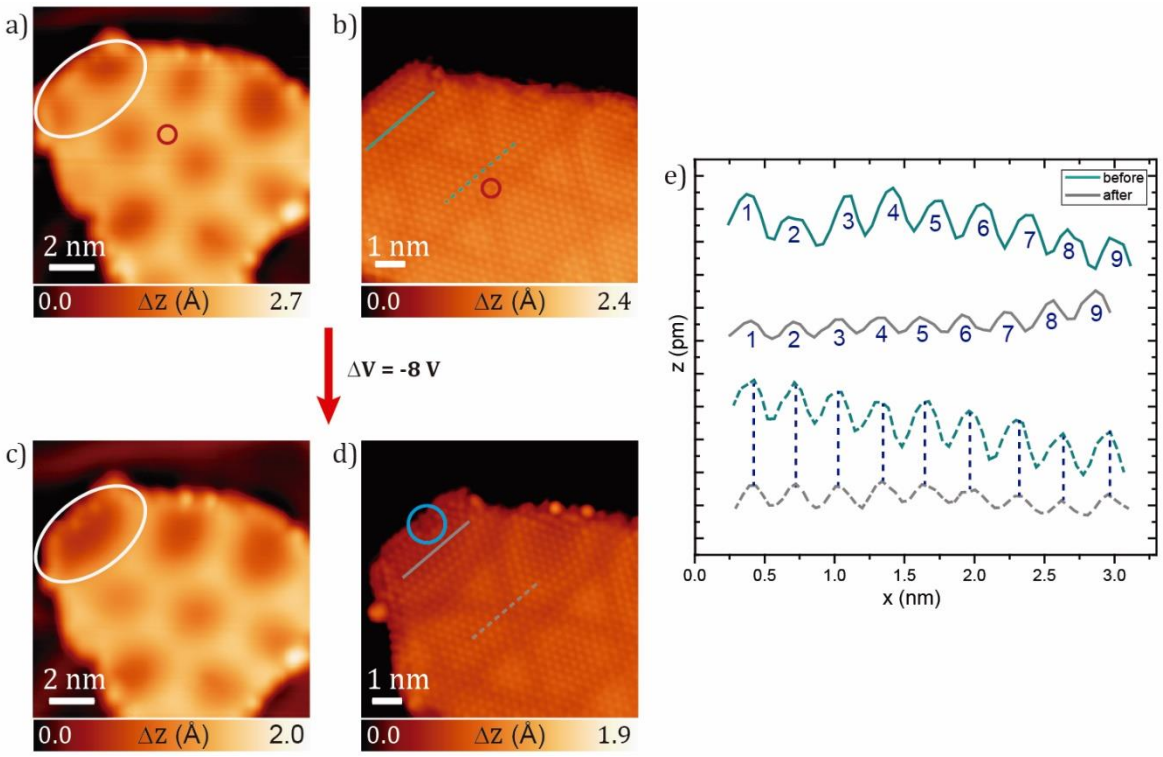

Figure 4-12. Atomic compression after electric field-induced change

a) *STM image of CoO island prior to tip manipulation (V_b = -1.0 V, I_t = 100 pA).* ***b)*** *High-resolution STM image of* ***a)*** *acquired with a CO-functionalized tip (V_b = 20 mV, I_t = 350 pA).* ***c)*** *STM image of the CoO island after tip manipulation (V_b = -1.0 V, I_t = 100 pA).* ***d)*** *High-resolution STM image of* ***c)*** *acquired with a CO-functionalized tip (V_b = 50 mV, I_t = 50 pA.* ***e)*** *Height profiles drawn at the same atoms raw before and after de modification. Continuous lines correspond to the compressed area and dashed lines to an unalterable area as reference.*

In summary, we are able to transform moiré regions into β-regions of c-CoO on Au(111) by electrically tip-induced pulses, thus transforming the electronic properties and the chemical reactivity of this material.

4.5 Water splitting reaction

As mentioned above, the target of the Artificial-Leaf project is the design of a PEC device used to transform the H_2O and CO_2 into oxygen and solar fuels. CoO was proposed as a tentative anode for being integrated in the PEC. To shed some light into the catalytic behavior of such material, we have exposed CoO nanoislands to water under UHV conditions.

Water exposure was carried out with extremely care, in order to avoid any contamination during the exposure which would alter the results. We installed an external line with its own pumping system connected to the preparation chamber by a leak valve (Figure 4.13). Ultrapure mili-Q water (< 1 μS/cm) in a glass vial was connected to the external line and degassed by several freeze-pump-thaw cycles with liquid nitrogen. The pressure in the water line was measured with a pirani gauge connected to the line, reaching a pressure value close to ~ 10^{-9} mbar. Water was dosed into the preparation chamber, with the substrate at RT, using a partial pressure of 5 x 10^{-7} mbar for 3 minutes and 20 seconds, which results in 100 Langmuir.

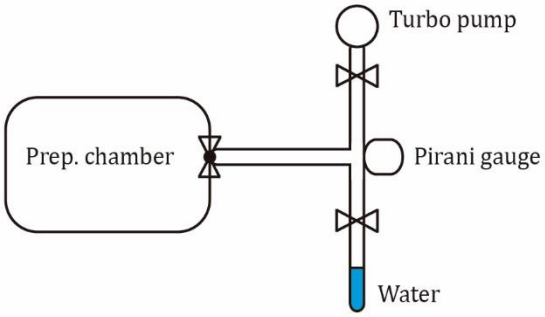

Figure 4-13. Water line dose scheme

After dosing the water into the preparation chamber, the sample was transferred to the STM where it was cooled down to 4.3 K. We investigated the surface of the single bilayer islands, where new bright protrusions appeared (Figure 4.14a). We observed two different adsorbates on the surface: type I marked with a blue circle (assigned to intact H_2O from the background of the chamber attached to the β-region) and type II marked with a yellow circle (the new adsorbate that appears after the water exposure shown in

Figure 4.14b-c). The adsorbate type II is attributed to hydroxyl groups from the water splitting reaction, supported by previous works where the exposure of H_2O was monitored by XPS (Figure 4.14b) and confirmed by the appearance of a new peak at 532 eV of binding energy assigned to O_{OH}.[128]

Then, we focused on the distribution of the hydroxyl groups (adsorbate type II). We found all the edges decorated with bright protrusions. In addition, we observed adsorbates covering the surface of the CoO. They show clearly preference for the moiré region A and the interface between areas A and B (Figure 4.14a), suggesting that the moiré pattern is a template for site-selectivity. As we commented before, it is known that the most reactive points are the edges of the islands.[128–130] We confirmed it for our experiments representing in a graph the percentage of surface covered by hydroxyl groups for different island sizes displayed in Figure 4.14d. We observe how the content of hydroxyl groups, and therefore the intrinsic catalytic activity, decreases for larger islands.

The mechanism proposed for the water splitting is explained following 3 steps: i) water molecules are majority adsorbed at the edges of the islands, showing clear preference for the Co-terminated edges, which are the most reactive points. ii) The water splitting reaction takes place there, dissociating the water molecule. The OH^- from the water molecules remains attached to the edge and the other hydrogen is transferred to an adjacent oxygen of the oxide, which is the most energetic step. iii) Then, each hydrogen atom initializes a hopping process being transferred over the oxygens of the CoO. showing preference for the moiré region A and forming aggregation of OH^- due to the interaction between them by hydrogen bonds which stabilizes each other[131] and favors the catalytic activity.[132,133]

As explained in section 4.3, the moiré region A interacts stronger with the gold and now, after the water exposure, we find that this area shows more affinity for the OH^- groups. Accordingly to previous works, there is a synergy effect between the cobalt oxide and the gold that increases the catalytic activity[108,109] and, with our results, we can tentatively attributed this effect to the electron transfer from the gold to the CoO. In addition, we

observe aggregation of OH^- due to the interaction between them by hydrogen bonds which stabilize each other.

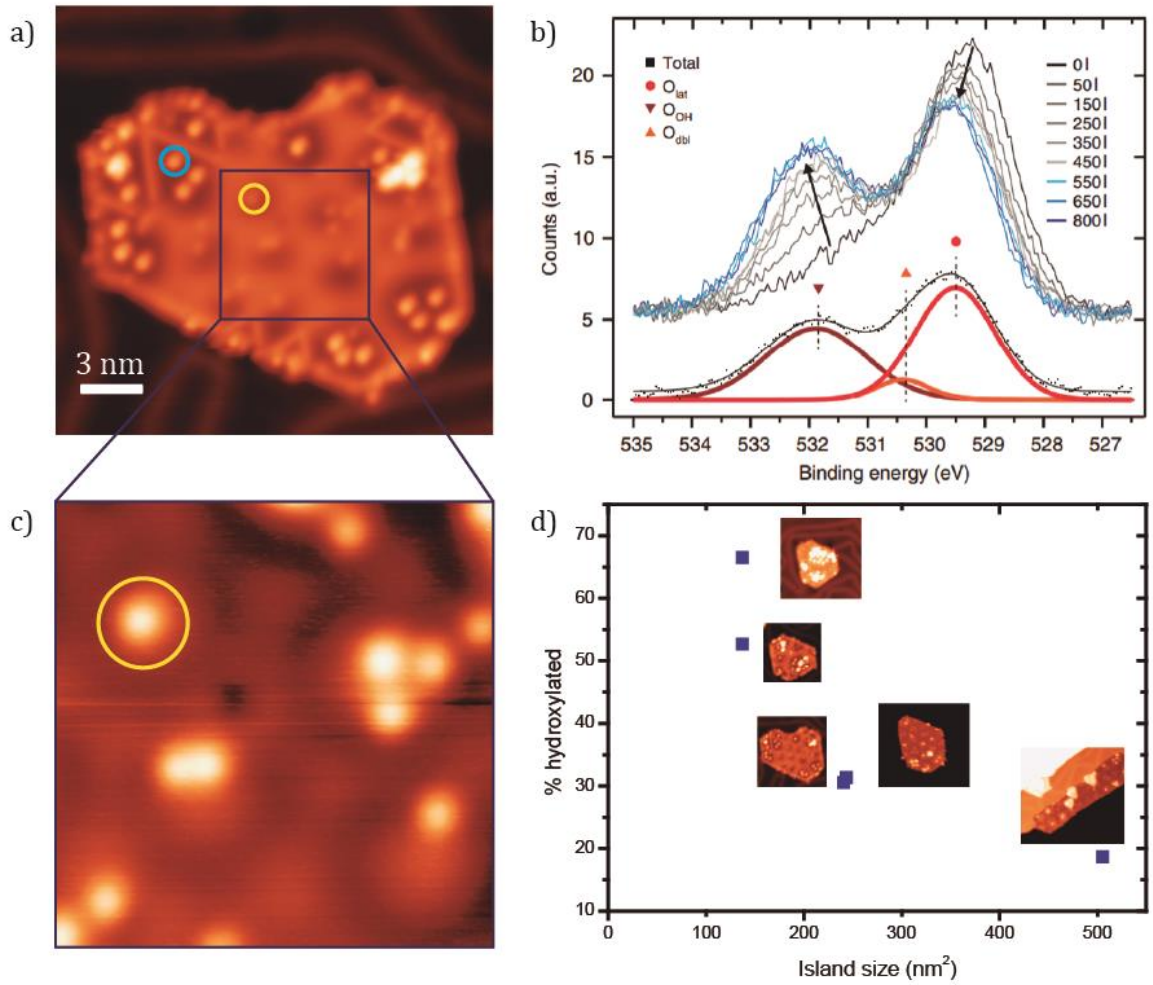

Figure 4-14. Water splitting mechanism

a) *Hydroxilation of CoO nanoisland. Yellow circle highlights the OH^- attached to the CoO and blue circle shows the water contaminants attached to the β-region (V_b = -0.5 V, I_t = 250 pA).* ***b)*** *XPS spectra of the O 1s core level during the water exposure. Extracted from reference* 128*.* ***c)*** *Zoom-in image of* ***a)*** *where the presence of OH^- are clearly observed (V_b = 1.0 V, I_t = 100 pA).* ***d)*** *Degree of hydroxylation versus the surface area of CoO nanoislands.*

Finally, we studied the reversibility of this reaction. As we described before, tip manipulation can induce different processes. In this case, we have tried to manipulate the hydroxyl groups by applying voltage pulses. Surprisingly, we observed that just by applying a voltage pulse of 3 V at any position of the CoO island, we induced the desorption of mainly all the adsorbates (Figure 4.15). After such desorption, the CoO nanoisland remains unalterable and it is available for going on with a new water splitting

cycle. It is worth to mention that we still find some adsorbates attached to the borders of the islands, which could affect the activity of the oxide.

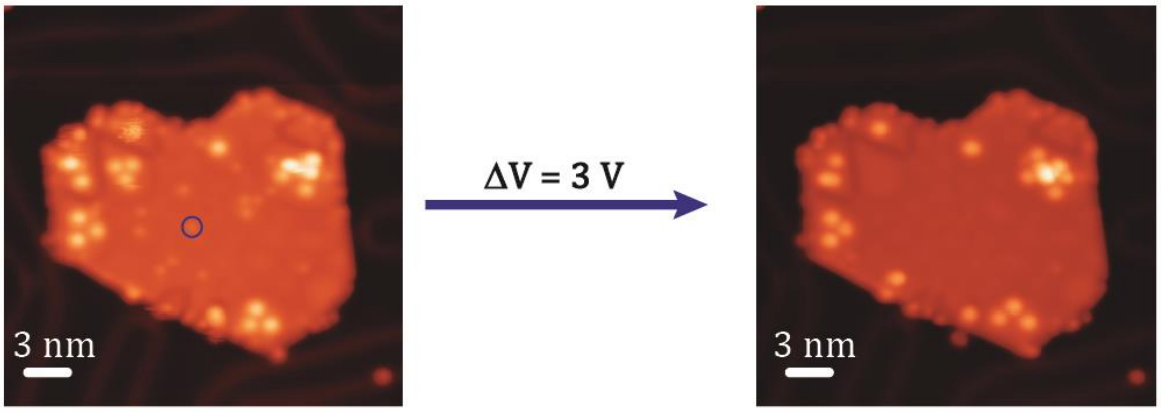

Figure 4-15. OH· desorption by tip manipulation

STM images of CoO islands before (left panel) and after (right panel) OH· desorption (V_b = 1.0 V and I_t = 100 pA).

4.6 Conclusions

Cobalt oxide is a promising candidate for catalyzing the water splitting reaction and could be integrated as anode in a PEC device. We have grown CoO nanoislands under UHV conditions on a Au(111) support, finding that the role of the substrate is non-innocent. Such CoO nanoislands show two coexisting phases: a moiré region and a commensurate β-region. We have inspected the interaction between the CoO and the gold atoms, which alters the electronic properties of the CoO islands. The moiré region A shows a stronger interaction with the gold substrate, where an electron doping from the gold to the CoO is suggested to take place. In addition, the moiré region A shows more affinity for the hydroxyl groups from the water splitting reaction, suggesting that the interaction between CoO and gold substrate could be the nature of the well-known synergy effect in electrochemical conditions.

We have identified a new region, named β-region, in the CoO nanoislands. We have proven that this β-region corresponds to an atomic compressed area, where a slight compression around 9 % is modifying the properties of the CoO, tentatively suggesting commensurability with the substrate. We have observed that the reactivity of this new

region is completely different from the moiré pattern region. Finally, we have demonstrated the capability to transform moiré regions into β-regions by tip-induced electrical pulses.

Finally, we have exposed our model nanocatalyst to 100 Langmuir of H_2O under UHV at RT. We have observed the appearance of bright protrusions assigned to OH^- groups, confirming the success of the water splitting reaction. We proved the reversibility of this reaction by tip-induced pulses, suggesting long lifetime for PEC devices.

5. On-surface synthesis of acene- and periacene- based π-conjugated polymers

This chapter presents the on-surface synthesis of π-conjugated polymers and the study at the atomic scale of their physico-chemical properties, which arise from the conjugation of their π electrons. Specifically, we focus on polymers based on acene or periacene units connected with each other through ethynylene/cumulene-like bridges.[20,134,135]

The chemical precursors were synthesized by the group of Prof. Nazario Martín from *Universidad Complutense de Madrid*. The DFT, GW calculations and nc-AFM simulations in this chapter were performed by Prof. Pavel Jelínek, from the *Institute of Physics of the Czech Academy of Sciences*, Czech Republic. The Tight Binding (TB) and Mean Field Hubbard Tight Binding (MFH-TB) calculations were done by Prof. Oliver Gröning at *Empa Materials Science and Technology*, Switzerland. The nc-AFM measurements from sections 5.3, 5.4, 5.5 and 5.7 were performed in collaboration with Dr. Bruno de la Torre at *The Regional Centre of Advanced Materials and Technologies* of Olomouc, Czech Republic. The reaction pathway of the synthesis of the polymers has been studied by means of DFT-based transition state theory performed by Prof. Jonas Björk at the *Department of Physics, Chemistry and Biology in Linköping University*, Sweden. Prof. Hans Lischka from *Tianjjin University*, China has performed the *ab initio* density matrix renormalization group (DMRG) calculations.

5.1 Introduction

π-conjugated polymers are defined as organic systems exhibiting carbon-carbon single-multiple bond alternation. Their overlapping p-orbitals create a system of delocalized π-electrons, which can result in very interesting electronic and optical properties. One of the main advantages that presents such polymers is the tunability of their properties depending on their π-extended conjugation along the molecular backbone.[136]

The evolution of the band gap (E_g) energy depends on the topology of π-electrons. The bond length alternation (BLA) of a conjugated system is the difference between the largest and the shortest C-C bond. This BLA is directly associated with the localization (larger alternation) or delocalization (small alternation) of π-electrons, and, as a consequence, with the value of the band gap energy of the system.[137] Hückel´s theory predicted that the value of the band gap of polyacetylene (PA) is proportional to the bond alternation.[138] This simplistic concept can be tentatively applied to all the π-conjugated molecules or polymers. However, it is important to notice that some π-conjugated polymers are based on aromatic rings, where the competition between the aromatic and the quinoid character alters the π-electron network, and thus a proper calculation of the band gap becomes difficult. Previous theoretical works reported that the increase of the quinoid character contributes to the decrease of the band gap energy due to the larger delocalization along the polymer instead of inside the aromatic ring,[139] which will be demonstrated throughout this chapter. Furthermore, we should take into account that the relation between the bond alternation and the band gap energy becomes even more complicated when the system involves heteroatoms, fused rings and other structural motifs.[137]

Many efforts have been focused on the design of π-conjugated polymers showing unique properties with applications in several fields, such as optics, electroluminescence, photovoltaics and organic electronics.[140] In 1977 the first conductive π-conjugated polymer was synthesized by doping the polyacetylene (PA).[141] PA is not a conductive polymer due to the dimerization by Peierls distortion that leads to a BLA ≠ 0. However, when such polymer is doped with an electron acceptor compound, such as halogens, vacancies (or holes) are created at the valence band, and, as a result, the conductivity of the polymers increases orders of magnitude. Such an effect was exemplified by just varying 1 % the content of the dopant. Alan J. Heeger, Alan G. MacDiarmid and Hideki Shirakawa were awarded with the Nobel Prize in Chemistry in 2000 for this discovery.[19]

Since then, a large variety of π-conjugated polymers has been investigated, where the presence of fused rings, heteroatoms or chirality plays a crucial role. In addition, the geometry, the coupling of the orbitals and the bond alternation determine the electronic

properties of such polymers. Over the last decades, a plethora of π-conjugated polymers have been synthesized (Figure 5.1 shows some examples),[142] but some limitations are found in wet chemistry, due to the high reactivity and low solubility intrinsic to such compounds. In this context, on-surface synthesis has emerged as a powerful strategy to develop and study new polymers overcoming the limitations found in solution chemistry.[143–145] Specifically, the on-surface synthesized polymers achieved in this work are formed by members of the acene and periacene families connected with each other *via* cumulene/ethynylene-like bridges.

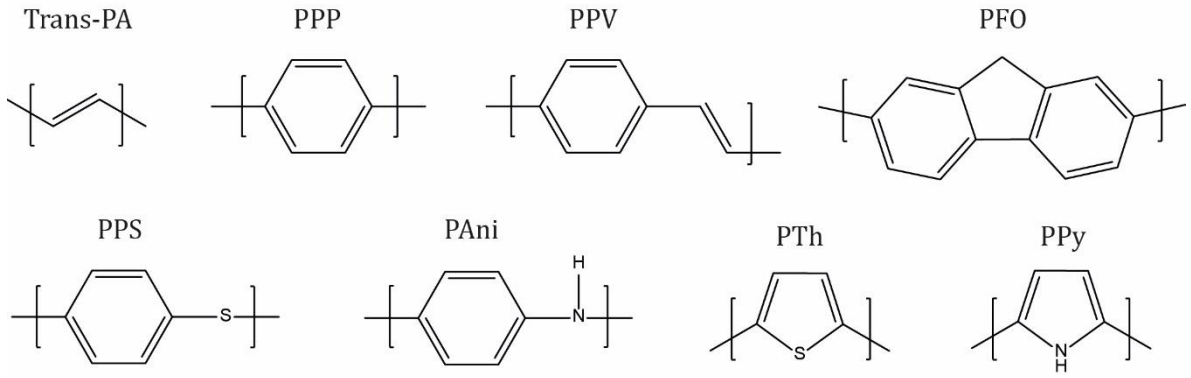

Figure 5-1. Chemical sketch of some π-conjugated polymers

Trans-polyacteylene (Trans-PA). Poly(p-phenylene) (PPP). Poly(p-phenylene-vinylene (PPV). Polyfluorene (PFO). Poly(p-phenylene-sulphide) (PPS). Polyaniline (PAni). Polythiophene (PTh). Polypyrrole (PPy). Adapted from reference 142.

Acenes and periacenes are polycyclic aromatic hydrocarbons (PAH). While acenes are composed by linearly fused benzene rings, periacenes are formed by two rows of *peri*-fused acenes with two distinct edge types: the armchair and the zigzag edges (see Figure 5.2). These compounds show particular interest in fields such as organic chemistry and material science, due to their low band gap and its tunability by varying the size, resulting in a wide range of applications.[146] Recently, several works have been reported, focusing on their intriguing optical,[147] magnetic[148–150] and electronic properties.[148,151] Small acenes and periacenes are predicted to be closed-shell structures with a non-magnetic ground state and large band gap energy, however by increasing their size an antiferromagnetic ground state is expected.[152]

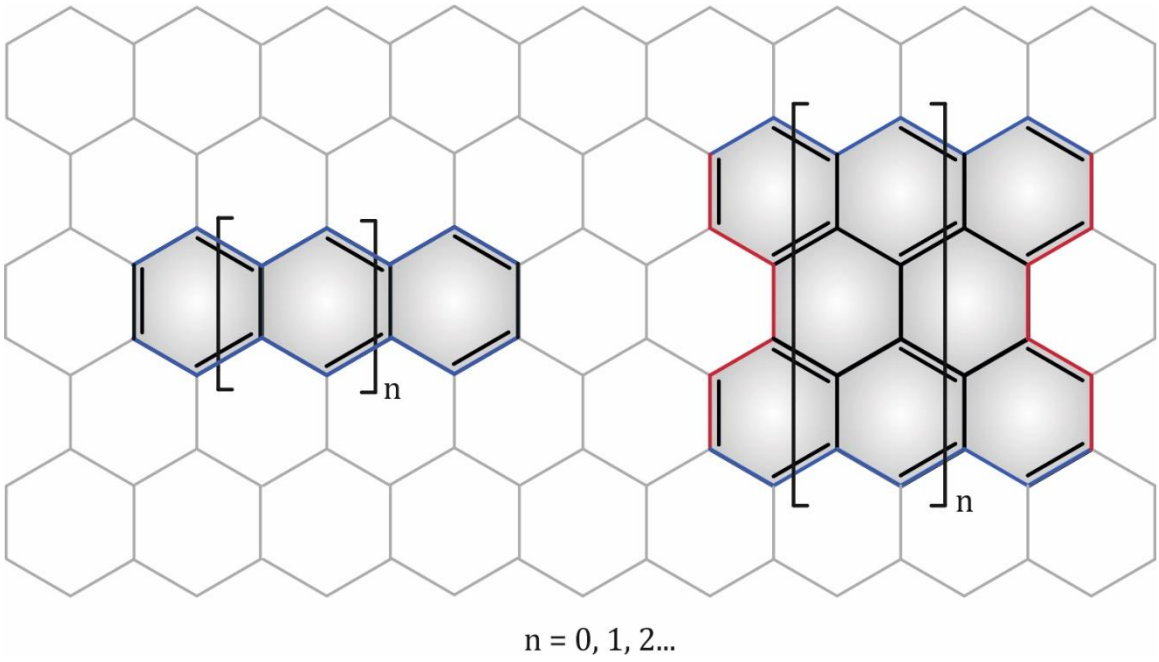

Figure 5-2. Chemical scheme of acene and periacene compounds

The zig zag and armchair termini are highlighted in blue and red, respectively.

As mentioned above, the versatile properties of acenes and periacenes make them promising carbon-based semiconductor compounds.[153] Their electronic properties can be tune by varying their sizes. However, larger acene and periacenes show high reactivity and low solubility,[154] which hamper their study. Therefore, on-surface synthesis emerged as a powerful alternative to overcome such limitations. Researchers from different groups have paid special attention in the study of these compounds.[45,155–157] The on-surface generation of acenes of different sizes on metallic substrates (from n=3 up to n=12, where n is the number of fused rings) reveals the decreasing experimental band gap as the acene length is increased, finding the lowest band gap for the undecacene (Eg ≈ 1 eV). However, moving a step further, dodecacene shows again a larger energy band gap of ≈ 1.4 eV (see graph in Figure 5.3).[158] This effect is rationalized by the electronic rearrangements taking place in the units with increasing number of valence electrons, which also augments the radical character, and hence, increases the open-shell character.[159]

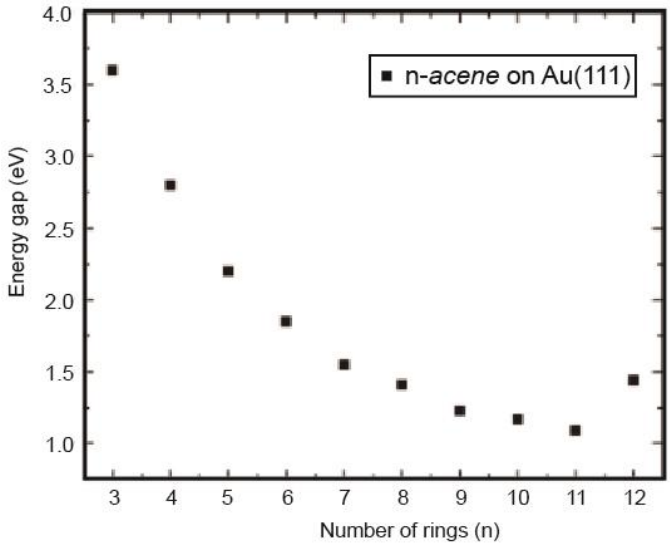

Figure 5-3. Band gap energy of acenes on Au(111) as function of the number of fused rings.
Adapted from reference 158.

In addition, these families of PAHs present a controversial nature of the ground state as a function of the number of fused benzene rings (n), which is associated to the degree of aromaticity of the benzene units.[160–162] Following the Clar´s rule, the formation of Kekulé structures that contain the largest number of disjoint Clar sextets results in more energetically favorable structures[163] (272 kJ per Clar sextet).[164] However, Kekulé structures cannot describe the open-shell character of PAHs, therefore it is needed to consider the non-Kekulé structures.[165] The transition between Kekulé and non-Kekulé structures implies an electronic rearrangement that cost a certain energy. Consequently, the most favorable resonance form is defined by a complex energetic balance. As a result, short acenes (from n=3 to n=6) exhibit a closed-shell electronic ground state with all the electrons paired.[152] Nevertheless, larger acenes present more resonance forms finding larger number of Clar sextets and hence more stability (see Figure 5.4), resulting in an open-shell structure with singlet, triplet or even quintet ground state predicted by theoretical calculations.[92]

However, for the periacene family, the radical character was predicted to appear from the peritetracene on, which already exhibits open-shell character (see Figure 5.4).[166] This open-shell character has been experimentally demonstrated for peritetracene derivative,[167] though has not yet been observed for pure peritetracene.[168] Altogether, the

inherent radical character of the acene and periacene families opens a new field of applications in spintronic devices for these materials, due to their inherent magnetic properties.[169]

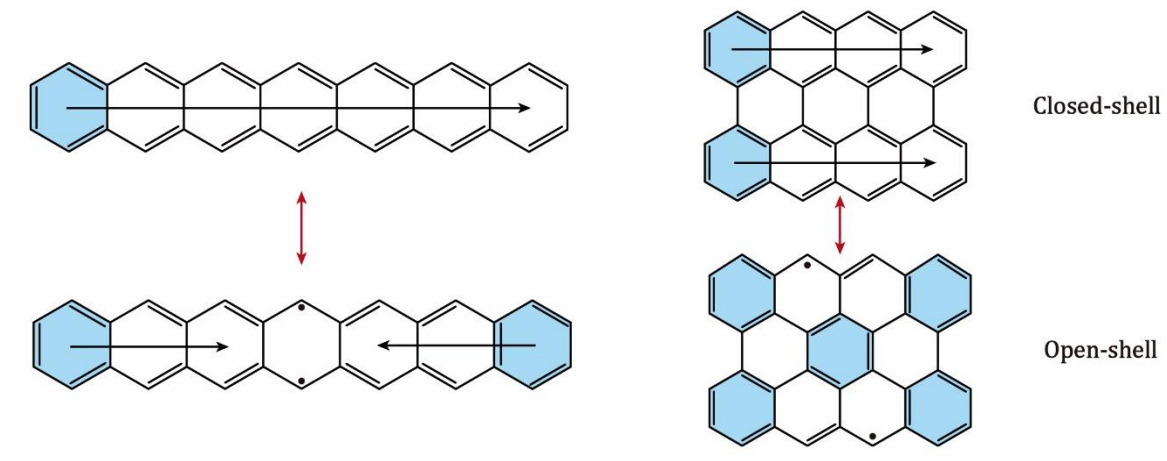

Figure 5-4. Closed- and open-shell structures of heptacene and peritetracene

Adapted from references 163,168.

In this chapter, we have developed an on-surface synthetic route towards the formation of π-conjugated polymers constituted by acene/ periacene units connected with each other through ethynylene/cumulene-like bridges (chemical synthesis is described in section 5.2). Here, we have combined the tunable properties of acenes and periacenes with the size and the powerful applications of π-conjugated polymers for a precise control of the electronic properties of the synthesized wires. As mentioned in section 2.2, based on topological predictions, we will synthesize π-conjugated polymers of distinct topological class, revealing the intimate connection between the change of the topological class and the crossover of the dominant resonance form.[20]

These π-conjugated polymers hold two main resonance forms, each one based on aromatic and quinoid structures of the monomers, respectively. The competition between these two π-conjugated forms also implies a simultaneous transformation of the polymer linkers, going from an ethynylene bridge in the aromatic case to a cumulene bridge in the quinoid one. Importantly, in this chapter we prove that the transformation of one dominant resonance form into the other one is associated with a different topological quantum class (see section 2.2). Notably, the transformation between the

two resonance forms occurs as function of the acene or periacene size. We have rationalized this effect with the Clar´s rule. For short acene- (n=3) or periacene-based polymers (n=2), the dominant resonance form is the ethynylene/aromatic structure, which contains all π-electrons paired. However, for longer acene- or periacene-based polymers, an increasing cumulene/quinoid character, which implies two unpaired electrons localized at both ends of the polymer, is observed. In addition, we show the band gap evolution as a function of the size of the monomer comprising the polymer (and the inherent topological class) in the acene (anthracene and pentacene) and the peripentacene families (bisanthene and peripentacene). Hereby, we demonstrate that polymers close to the topological transition point present very narrow band gaps, corroborating that the topological transition implies crossing through a metallic state.[34]

5.2 Synthetic routes towards π-conjugated polymers on surfaces

During the last years, on-surface synthesis has become a powerful tool to achieve new nanostructures overcoming the intrinsic limitations of solubility and reactivity of some compounds, such as acenes longer than pentacene[158] or periacenes larger than bisanthene,[168] among others. Specifically designed molecular precursor sublimed on surfaces may follow, after an annealing process necessary to induce the chemical reaction, different pathways with respect to the ones observed in solution, due to the template effect of the surface that confines the precursors in two dimensions. Additionally, on-surface synthesis provides a precise atomistic control over the formation of well-designed nanostructures and allows their direct characterization by surface science techniques such as STM, nc-AFM and STS.

Recently, great efforts have been focused into the development of on-surface routes towards the atomically precise synthesis of novel carbon-based nanostructures such as graphene nanoribbons,[170,171] 2D polymers[172] and other hydrocarbons structures.[173,174] In this context, one of the main strategies employed so far has been based on dehalogenative homocoupling reactions (some examples are shown in Figure 5.5).[175,176] Specifically, the most studied on-surface reaction up to now is the Ullmann coupling reaction, which has been extensively employed to engineer covalent 1D[177–179] and 2D nanoarchitectures.[180–182] Such strategy consists in the functionalization of carbon-based molecular precursors

with halogens at their terminal positions (-CBr) in order to induce the homocoupling of the molecular precursors. After the deposition of these molecules and subsequent annealing to a certain temperature, the halogen atoms are lost and then two routes are feasible depending on the substrate.[181,183] Generally, on Ag(111) and Cu(111) a metal-organic step is frequently induced. Herein, the molecules have lost their halogens due to the catalyzing effect of the surface and the metal adatoms are connected to the molecular backbone forming a stable metal-organic system. Finally, after annealing at higher temperatures, the metalorganic bonds derived in the intermolecular carbon-carbon coupling.[184,185] On Au(111) the reaction normally proceeds through radicals in which the terminal carbons have lost the bromine that results in the carbon-carbon homocoupling.

Recently, new dehalogenative homocoupling reactions of geminal dihalide compounds have been reported.[186,187] The loss of the two bromines attached to the terminal carbon leads to generate C-C coupling with two unpaired electrons per carbon atom, resulting in the formation of a dimer based on a cumulene connection.

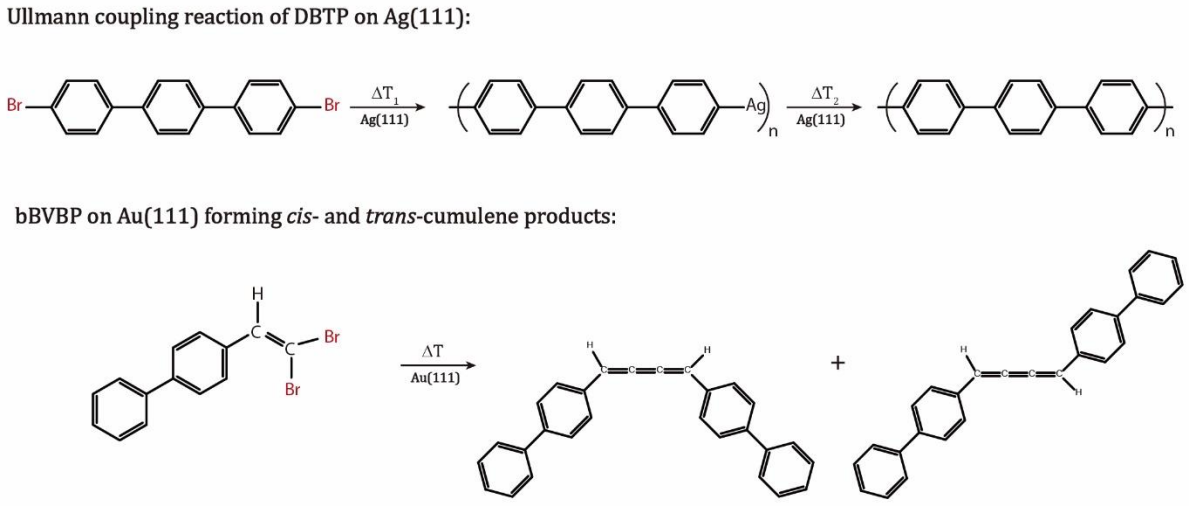

Figure 5-5. Scheme of synthesis of PH via dehalogenative homocouling

Image adapted from references 184,187.

Motivated by the versatility of the aforementioned dehalogenative homocoupling reactions, we have functionalized different acenes and periacenes precursors with $=CBr_2$ functional groups, where two unpaired electrons are generated (carbene compound)

after the loss of the bromines by thermal annealing process, being capable to design π-conjugated polymers on surfaces.[134] Here, we demonstrated the viability of this reaction using acene- and periacene-based precursors. We observed that the reaction is dominated by 2 steps in the case of the acene-based precursors: i) dehalogenation and ii) subsequent homocoupling; and three steps for the periacene-based precursors: i) dehalogenation, ii) homocoupling and iii) cyclodehydrogenation (Figure 5.6).

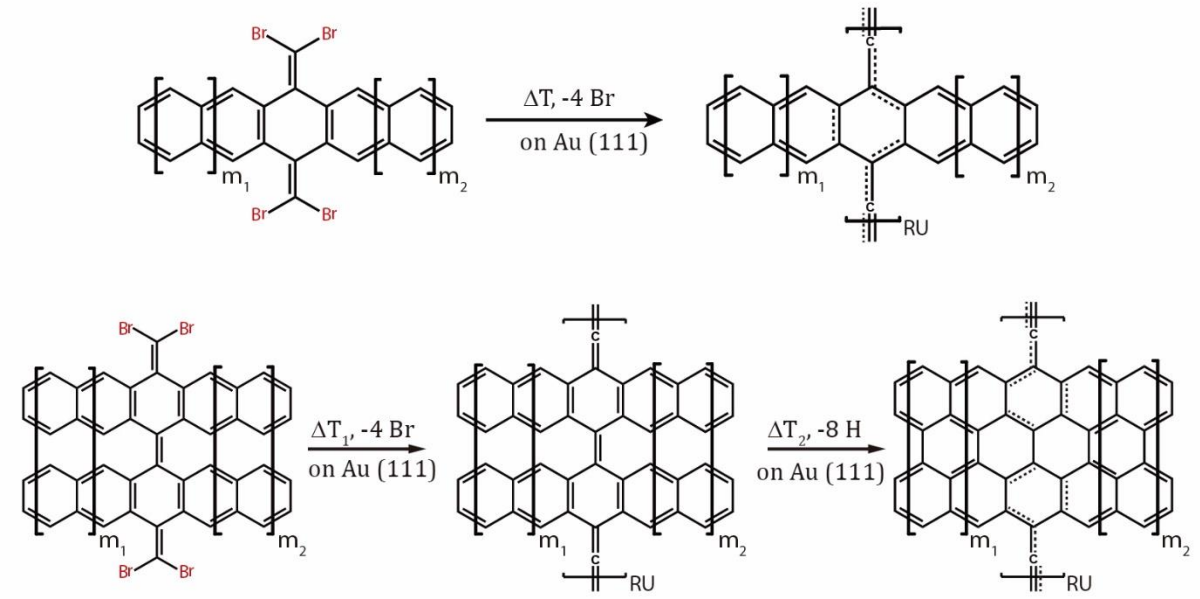

Figure 5-6. Synthesis route of ethynylene/cumulene bridged acenes (top scheme) and peri-acenes (bottom scheme) polymers

The acene- and periacene-based precursors are functionalized with $=CBr_2$ groups at the central benzene rings. Such compounds are evaporated onto a metallic surface, giving rise to linear polymers after thermal activation. The molecular species employed for the acene family are: 4BrAn (9,10-bis(dibromomethylene)-9,10-dihydroanthracene) and 4BrPn (6,13-bis(dibromomethylene)-6,13-dihydropentacene); and for the periacene family: 2(2BrAn) (10,10'-bis (dibromomethylene) -10*H*,10'*H*-9,9'-bianthracenylidene) and 2(2BrPn) (13,13'-bis (dibromomethylene) -13H,13'H-6,6'-bipentacenylidene) (chemical models shown in Figure 5.7). Once the molecules are deposited onto the substrate, a thermal process induces the loss of the halogens forming carbene species

that diffuse and homocouple, resulting in ethynylene or cumulene-bridged anthracene, pentacene, bisanthene or peripentacene polymers.

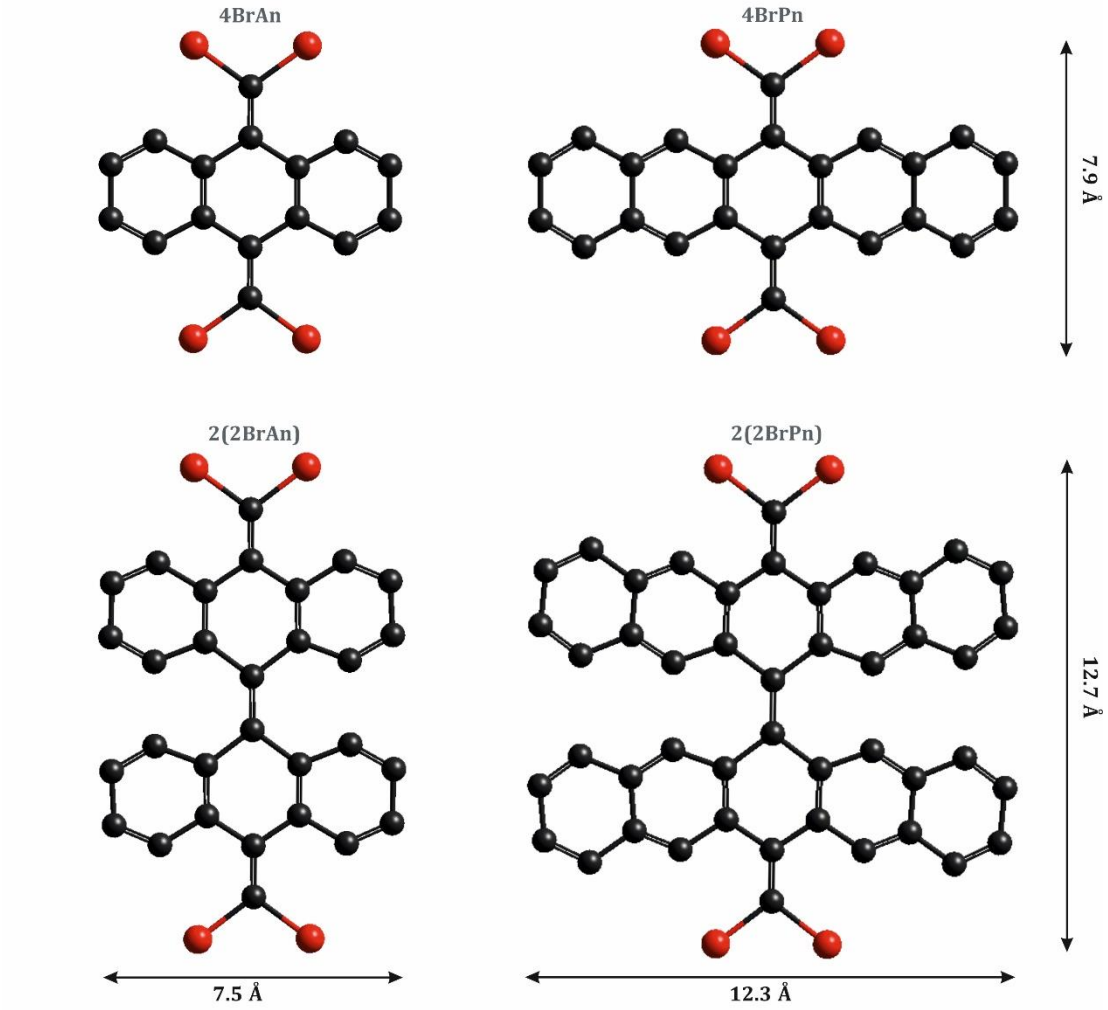

Figure 5-7. Chemical structure of the employed precursors

Ball and stick model of the gas phase relaxed geometry of the 4BrAn, 4BrPn, 2(2BrAn) and 2(2BrPn) precursors, with carbon and bromine colored in black and red, respectively.

This dehalogenative homocoupling reaction introduces, thus, a strategy towards the design of π-conjugated polymers comprising acene- and periacene-based precursors. We envision the versatility of this reaction, since it provides an extraordinary control over the carbon-carbon homocoupling positions, and hence, of the carbon-based materials synthesized. In addition, the reported reaction opens new avenues towards the design of polymers with tailored properties,[134] such as tunable band gap or radical character, featuring great potential in organic electronics or spintronics.

5.3 Ethynylene-bridged anthracene polymers

The deposition at 373 K of a submonolayer coverage of 4BrAn on pristine Au(111) at RT results in the formation of self-assembled islands stabilized by Br···H interactions between adjacent molecular species. Figure 5.8a shows an overview STM image of the self-assembly where the absence of bromines on the Au(111) surface suggests that the molecular precursors have remained intact on the gold surface. In addition, the nc-AFM image of the self-assembly displayed in Figure 5.8c reveals the non-planarity of the molecules and two distinct adsorption conformations. Non-contact AFM simulations of the intact 4BrAn with the $=CBr_2$ groups pointing away from the substrate (E^1_{ads} = -2.47 eV) and pointing towards the substrate (E^2_{ads} = -2.49 eV) were performed (Figure 5.8e-f), showing a perfect agreement with the two conformations observed in the nc-AFM image.

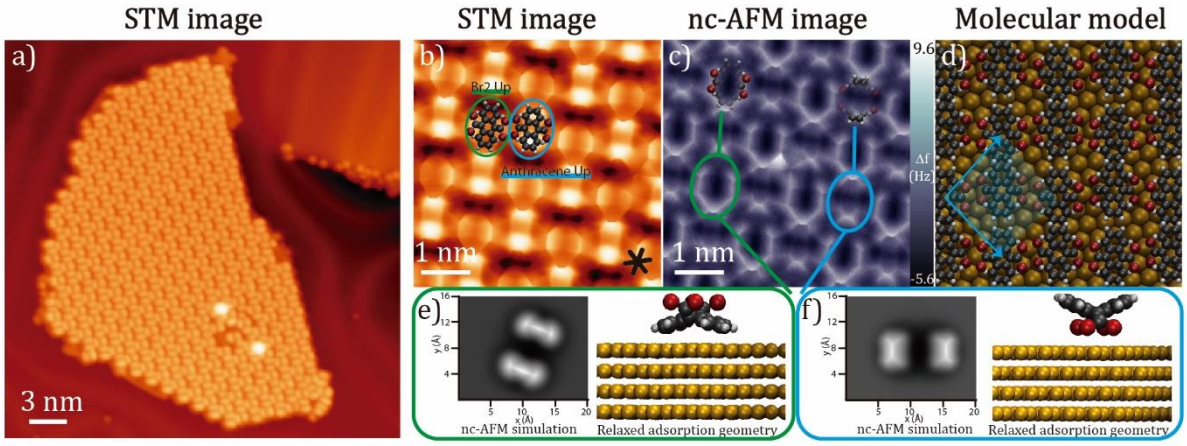

Figure 5-8. Self-assembly of 4BrAn on Au(111) after deposition at RT

a) *Overview STM image of self-assembly of 4BrAn on Au(111) (V_b = -1.0 V and I_t = 150 pA).* ***b)*** *Constant height STM image of the supramolecular self-assembly showing the two different adsorption geometries with Br pointing up and Br towards the surface in green and blue, respectively. (V_b = -60 mV).* ***c)*** *nc-AFM image revealing the appearance of the two different species. (V_b = 10 mV).* ***d)*** *Ball-and-stick model on Au(111) surface (Black, red and white balls corresponds to carbon, bromines and hydrogen atoms, respectively).* ***e)*** *nc-AFM simulation and relaxed adsorption geometry calculated for the specie with the bromines pointing up.* ***f)*** *nc-AFM simulation and relaxed adsorption geometry calculated for the specie with the bromines toward the surface.*

A first annealing step at 400 K leads to the formation of long and linear polymeric wires due to the detachment of bromine atoms from the molecular backbone and the subsequent intermolecular C-C homocoupling. These bromine atoms are observed as bright protrusions decorating the Au(111) surface forming chains and clusters

surrounding the polymers, and also being located in between the polymeric wires (Figure 5.9a).[177,188] In addition, we could visualize several dimers, trimers and longer oligomers (Figure 5.9c), although the majority of the molecules have reacted with each other forming long polymers. Figure 5.9c shows that the edges of several oligomers and polymers present a curved shape. nc-AFM images acquired at such polymer edges reveal that the terminal monomer is not planar and seems to be pushed down towards the surface.

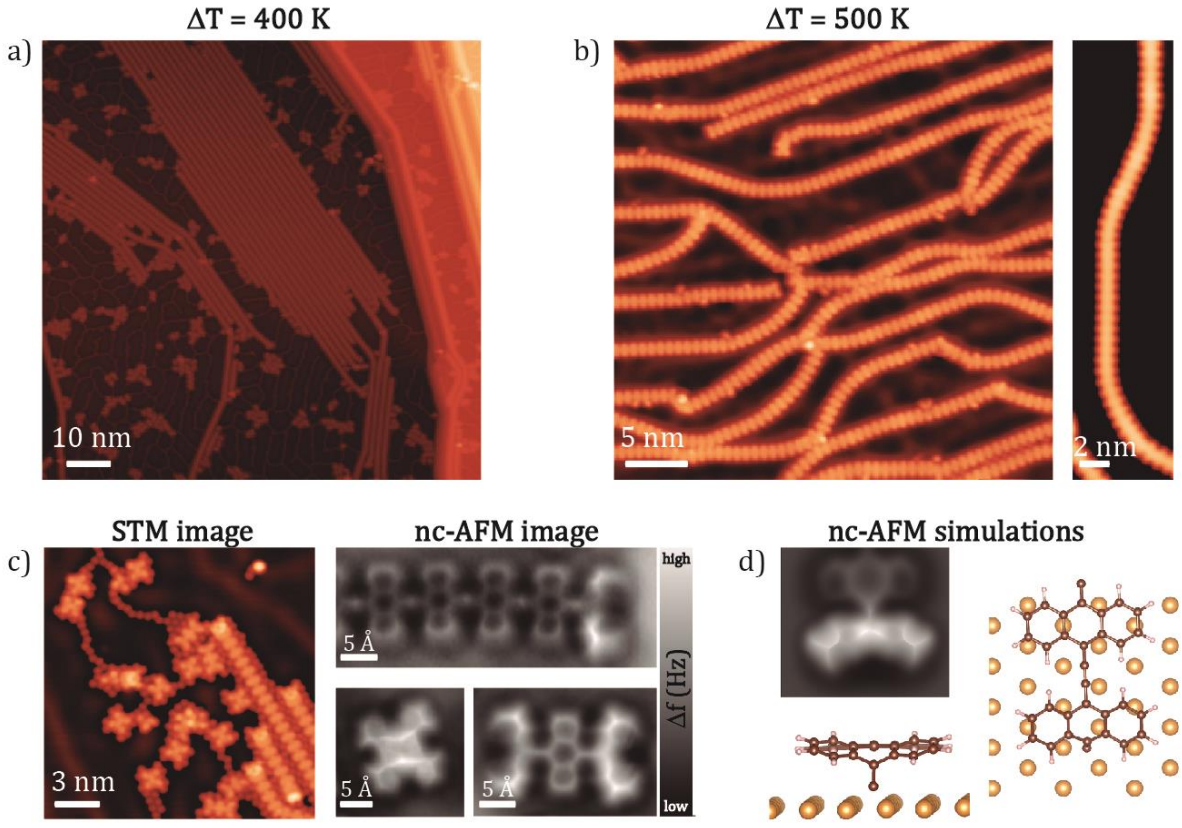

Figure 5-9. Anthracene polymers formation after 4BrAn deposition on Au(111) and subsequent annealing

a) *Overview STM image after thermal annealing to 400 K (V_b = 0.1 V and I_t = 10 pA).* ***b)*** *Overview STM image after thermal annealing to 500 K (V_b = 50 mV and I_t = 10 pA).* ***c)*** *STM image in left shows the ends of polymers, dimers and trimer. Nc-AFM images reveal the non-planar molecules at the ends. (STM image: V_b = -0.1 V and I_t = 50 pA; nc-AFM images: V_b = 3mV).* ***d)*** *AFM simulation and DFT simulation of the end of a chain, allowing to relax the edge monomer.*

A simulated nc-AFM image of the end of an anthracene chain with the last monomer still equipped with a terminal carbon atom (Figure 5.9d), reminiscent of the $=CBr_2$ functional group, is in excellent agreement with the experiments. The interaction of the edge with the gold surface results in the bending of the last anthracene unit towards it. Hereby, it is

worth to point out that the interaction of the terminal carbon with the substrate only alters the geometry of the terminal monomers. Such phenomenon is illustrated for a trimer, in which the central anthracene unit is totally planar (see trimer in Figure 5.9c).

Finally, further thermal annealing at 500 K leads to desorption of the remaining bromines from the surface. We observe the formation of long and almost defect-free anthracene polymers (Figure 5.9b). The absence of bromines on the surface enables the mobility of the chains, finding isolated and flexible wires, featuring curved chains up to 130^0. At this annealing temperature the presence of oligomers is no longer observed, which is tentatively attributed to their high mobility and flexibility, resulting on the formation of long (>100 nm) polymers. A detailed study of the chemical structure and the electronic properties of these polymers is provided later in this section.

The reaction pathway for the homocoupling reaction described above has been studied by means of DFT-based transition state theory. The most favorable mechanism is shown in Figure 5.10, finding that the reaction follows an exothermic pathway of -1.80 eV towards the full dehalogenation. Then, the dehalogenated units (S_{deBr4}) diffuse following two of the high symmetry directions (perpendicular to the anthracene backbone) with an energy cost of 0.53 eV. The activation energy for the final approach and coupling is 0.93 eV and takes place when two molecules find each other followed by a highly exothermic step, definitely stabilizing the final formed product.

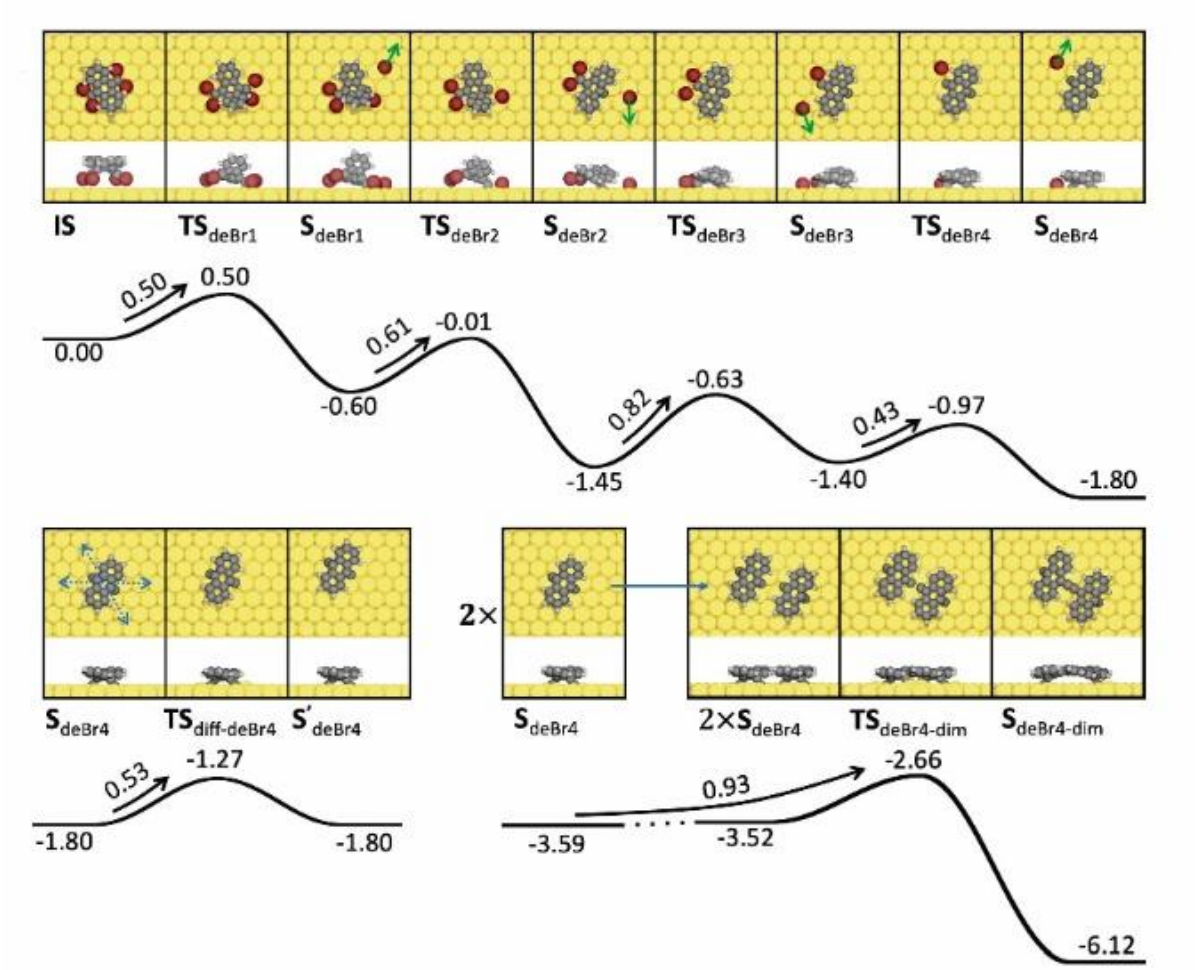

Figure 5-10. Energetically most favorable reaction pathway for the debromination homocoupling of 4BrAn precursors on Au(111)

*The mechanism diagram shows top and side views of local minima (**S**) and transition states (**TS**) with the corresponding energy profile with respect to the initial state (**IS**): the three different profiles correspond to: i) Initial dehalogenation cascade, ii) diffusion of the dehalogenated molecule, and ii) coupling of two dehalogenated molecules. Energies in eV.*

As explained in section 5.1, a competition between quinoid and aromatic resonance forms for the anthracene backbone is expected (scheme shown in Figure 5.11). The aromatic backbone shows a migrating Clar sextet (electron delocalization in all the backbone), while the quinoid form shows two Clar sextets at the terminal rings, which correspond to closed-shell structure and open-shell character for isolated monomers, respectively. The aromatic character is expected to be more energetically favorable in the anthracene backbone, although many reactions take place at positions 9 and 10 of central rings as consequence of the slight quinoid character.[164] In addition, the competition between resonance forms in the anthracene backbone should be reflected in the bridges

of the polymer, in this case ethynylene versus cumulene-like forms, as illustrated in Figure 5.11.

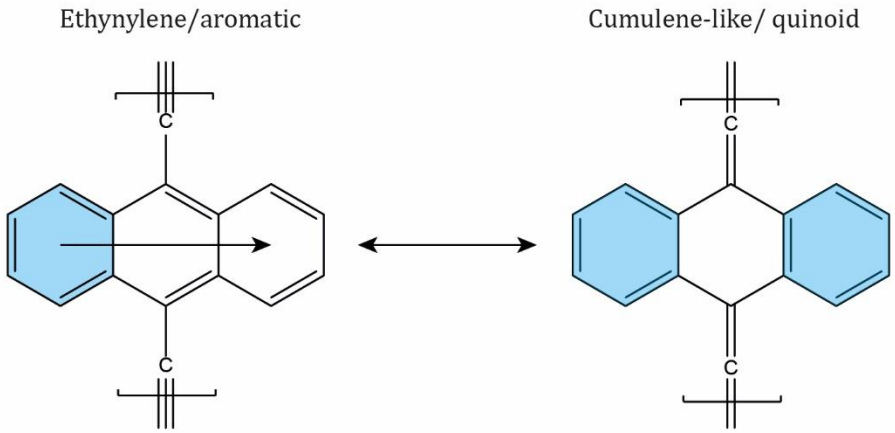

Figure 5-11. Scheme of the resonant form structures of the anthracene polymer

Blue filled rings correspond to the Clar sextets.

First, we have investigated the nature of the bridge by means of nc-AFM measurements. As previously reported, constant-height nc-AFM images acquired with a CO functionalized tip allow the identification of triple bonds, which is visualized as an enhancement of the contrast due to the larger electron density of the triple bond in comparison to the adjacent carbon atoms of the bridge.[189–191] As illustrated by the nc-AFM image displayed in Figure 5.12c, the polymer exhibits a bright protrusion at the middle of the bridges and, thus, they are assigned to ethynylene bridges. The simulated nc-AFM image in Figure 5.12d matches very well with the experimental data and further supports the ethynylene chemical nature of the bridge. As commented above, the formation of the ethynylene bridges is associated with an electron rearrangement at the backbone, resulting in the aromatization of the proquinoid backbone of the molecular precursors. The long-range nc-AFM image in Figure 5.12e reveals the uniform formation of ethynylene-bridged anthracenes along the polymer.

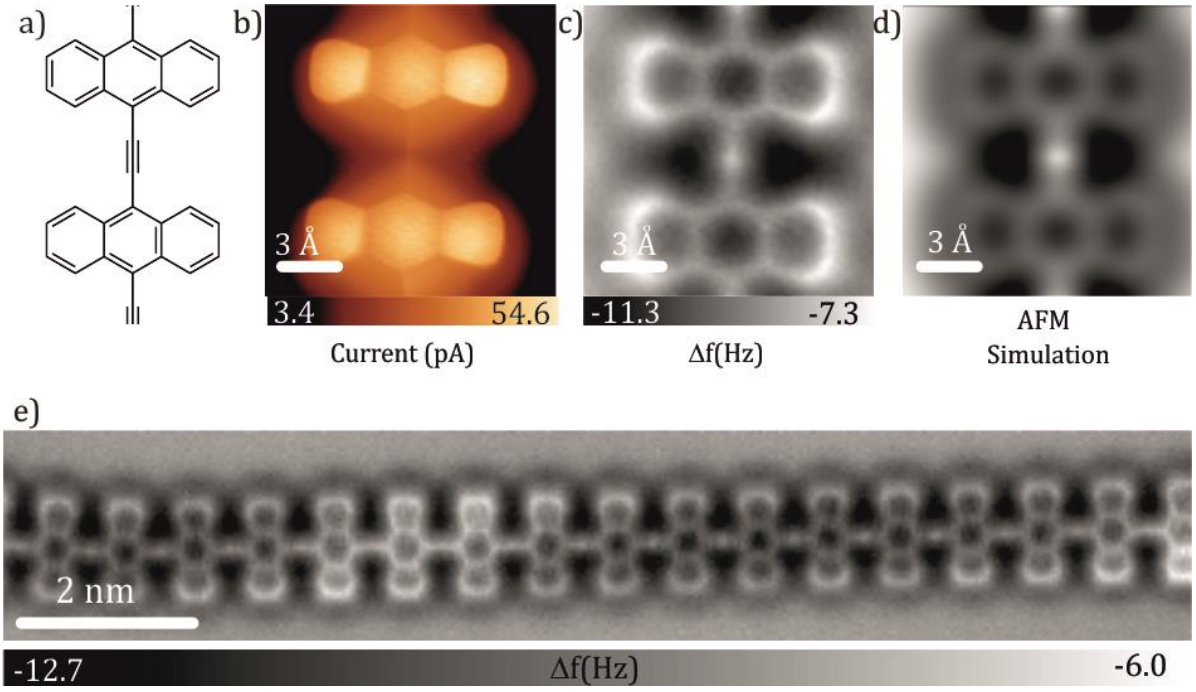

Figure 5-12. Successful formation of planar anthracene polymers

a) *Chemical structure of an ethynylene-bridged anthracene moiety.* ***b)*** *Constant-height STM (V_b = 3 mV) and* ***c)*** *nc-AFM image resolving the intact anthracene backbones (V_b = 3 mV).* ***d)*** *Nc-AFM simulation, which corroborates the experimental measurements.* ***e)*** *Constant-height nc-AFM image of a linear polymer. (V_b = 3 mV).*

Tip-sample distances play an important role in the elucidation of the triple bond. The dependence of the frequency shift with the tip-sample distance is shown in Figure 5.13. First, the force spectra recorded on top of the single and the triple bond (marked in the inset with red and green stars, respectively) reveals a different interaction in the attractive regime before reaching the frequency shift minimum. Then, at closer tip-sample distance, the curves evolve inverting the force interaction. In conclusion, the Δf differs only at specific tip heights, in contrast to higher heights where the resolution is expected to be similar or lowers heights where it is even inverted.[192]

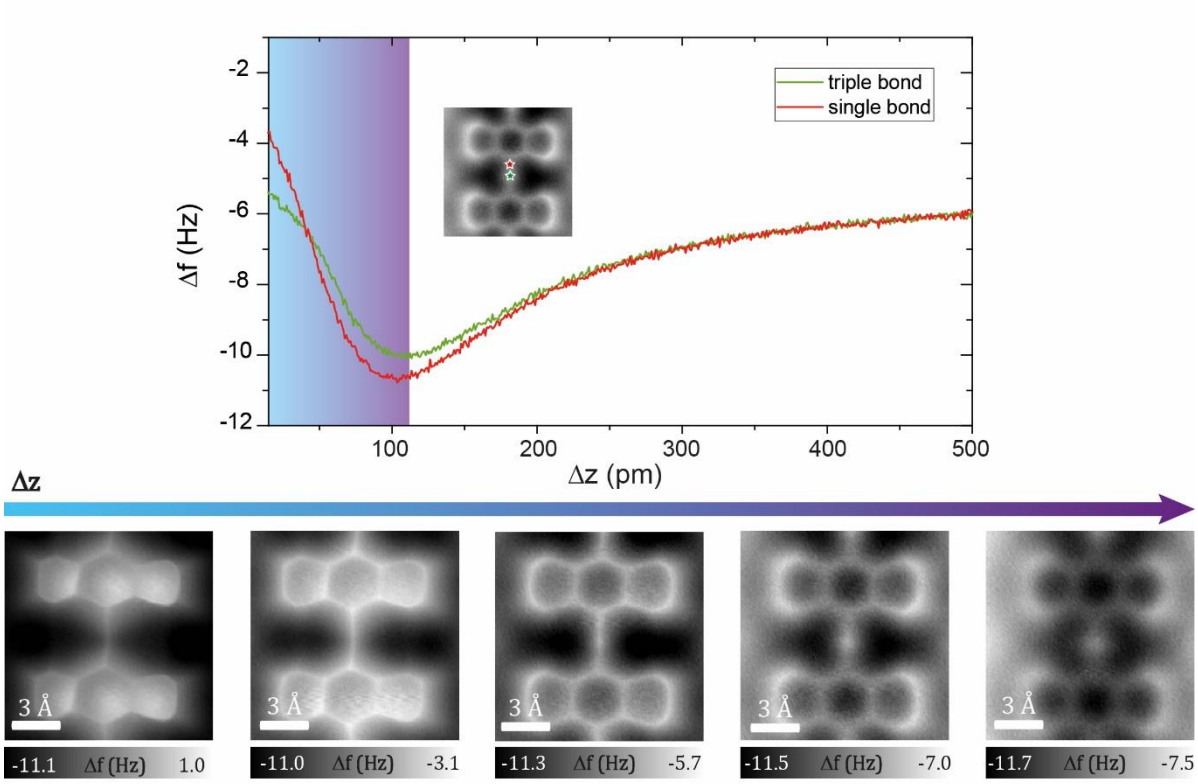

Figure 5-13. Elucidation of the ethynylene bridge

Upper panel shows force spectra acquired on top of the single and triple bond showing the dependence of the Δf with the tip-sample distance are represented. Bottom panel shows nc-AFM images of a single-triple-single bridge at different tip heights acquired with a CO-tip (V_b = 3 mV).

The contrast inversion at the ethynylene bridge is demonstrated in the bottom panel of Figure 5.13, where several nc-AFM images of the same polymer segment acquired with an increasing step height of 20 pm are shown. Changes in resolution are clearly observed being in perfect agreement with the force spectra (top panel of Figure 5.13), which suggests that for larger distances the elucidation of the bright protrusion is plausible, whereas at medium distances the observation of a uniform narrow line and at shorter distances an inversion in the resolution of the bridge are expected, respectively.

Once the nature of the bridge has been discerned, we have investigated its robustness and flexibility. Polymer chains exhibit a considerable degree of flexibility, showing open curvatures (up to 130^0) by bending of the ethynylene bridge. Nc-AFM measurements confirm that the nature of the linker remains intact, regardless of the bending (Figure 5.14a). Furthermore, the curvature of the chains can be intentionally induced by lateral

manipulation. Figure 5.14b-c shows the initial and final stage of a chain before and after the STM tip induces lateral manipulation. Remarkably, after the manipulation process the chains preserve intact its chemical structure, revealing the robustness and flexibility of the polymers.

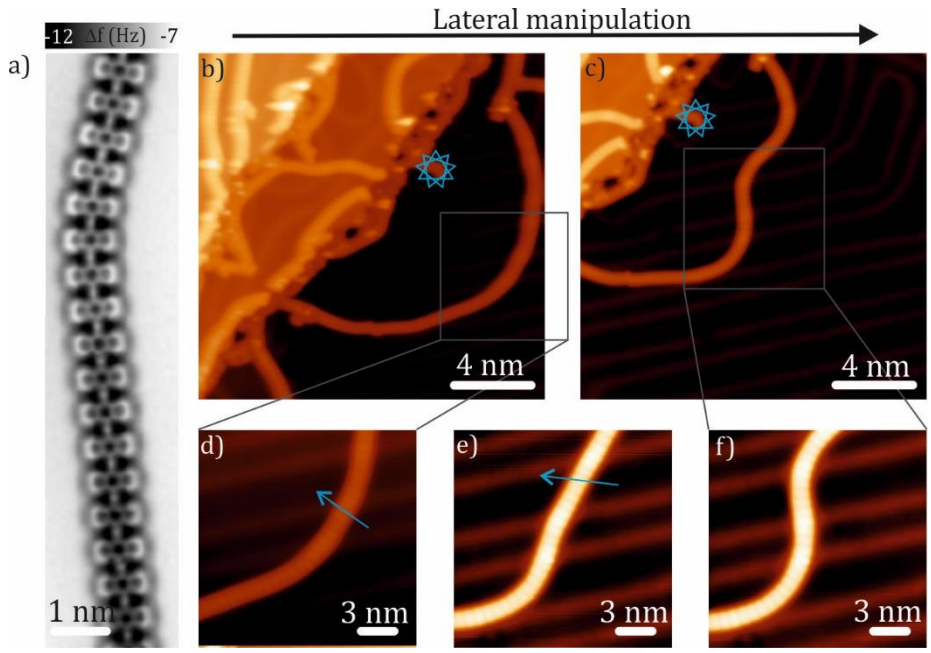

Figure 5-14. Flexibility of the ethynylene-bridged anthracene polymer

a) *Nc-AFM image of a curved anthracene polymer (V_b = 3 mV).* ***b)*** *and* ***c)*** *show the initial and final stage before and after lateral manipulation of the chain. Blue star indicates a reference point.* ***d)***, ***e)*** *and* ***f)*** *show the intermediate stages and the blue arrows indicate the directions of the later manipulation. (All STM images were acquired with similar parameters: V_b = -1.0 V and I_t = 150 pA) (Lateral manipulation parameters: V_b = -0.1 V and I_t = 20 nA, t = 30 ms).*

Next, the electronic structure of the π-conjugated polymers has been inspected by means of STS, complemented by DFT. First, the band gap of the polymer was elucidated by acquiring dI/dV curves (Figure 5.15a) on top of the voids adjacent to the ethynylene bridge (purple line) and on top of the terminal ring of the anthracene moieties (green line). STS measurements show two strong resonances at -0.6 eV and +0.9 eV, which are tentatively assigned to the valence band (VB) and the conduction band (CB) of the polymer, respectively. The orange curve was acquired on top of the Au(111) as a reference. Then, we have resolved the onset of the bands by acquiring constant-current dI/dV maps at their specific energies (Figure 5.15c). On one hand, mapping of the dI/dV signal at -0.6 eV allows us to visualize the onset of the valence band, which displays

density of states in between the anthracene moieties, especially at the adjacent voids. On the other hand, constant-current dI/dV maps acquired at +0.9 eV reveals the onset of the conduction band, located over the peripheries of the anthracene moieties. From these values, we obtain an experimental band gap of 1.5 eV. Here, it is worth to highlight the versatility of on-surface synthesis towards the formation of linear π-conjugated polymers presenting a large variety of band gaps.[193,194]

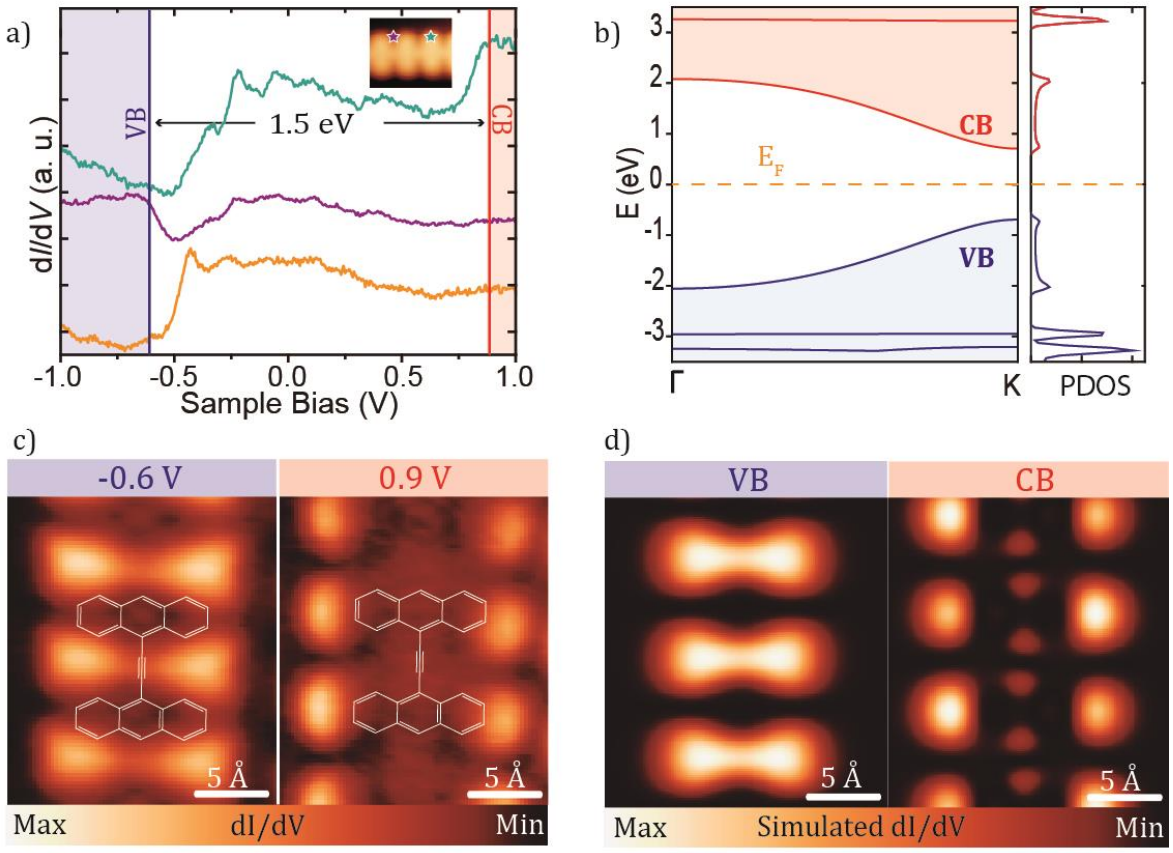

Figure 5-15. Experimental and theoretical results of the electronic structure of the anthracene polymer ***a)*** *STS measurements revealing the experimental value of the band gap. The dI/dV curves were acquired at the positions depicted in the inset STM image.* ***b)*** *Bulk calculated band structure and projected density of states (PDOS).* ***c)*** *Constant-current dI/dV maps acquired at the energies of the VB (V_b= -0.6 V) and CB (V_b= 0.9 V).* ***d)*** *Simulated dI/dV maps of the freestanding anthracene polymer.*

In order to corroborate our experimental results, we have compared them with simulated freestanding polymer using the B3LYP density functional (Figure 5.15b). Such calculations reveal the dispersive character of the bands. Though DFT of freestanding polymers overestimates the band gap, since screening from the substrate and electronic

correlation in the polymer are not included in the calculations,[195–197] the simulated LDOS maps (Figure 5.15d) of the freestanding polymers match perfectly with the experimental constant-current d*I*/d*V* maps, confirming our interpretation of the electronic structure.

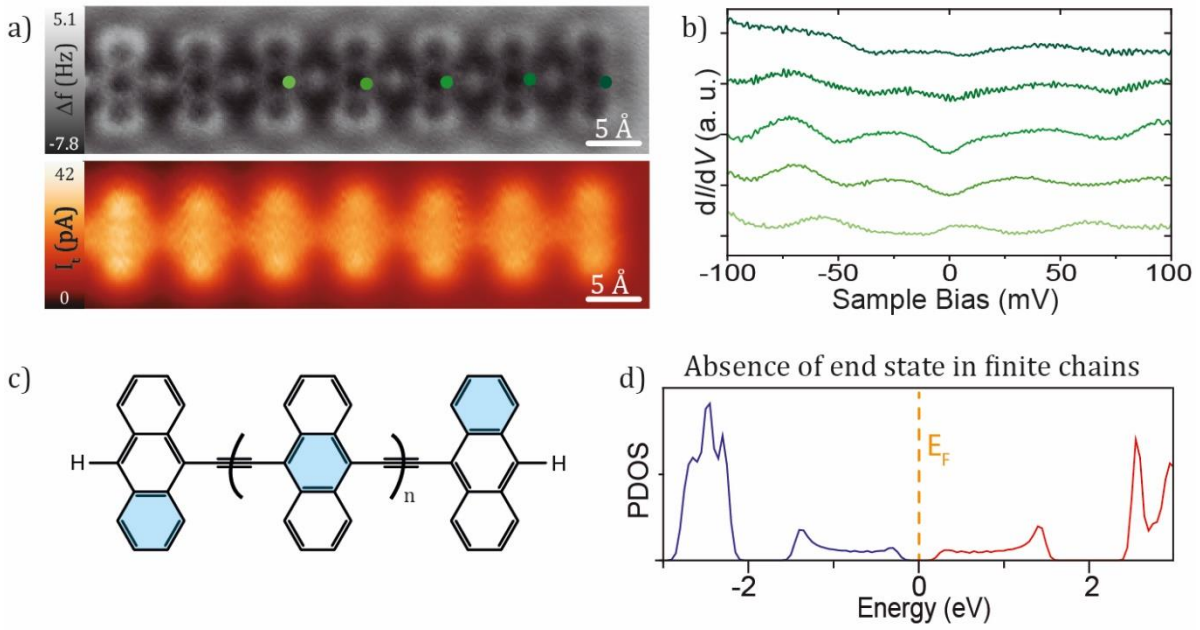

Figure 5-16. Experimental and theoretical results of the electronic structure at the ends of the anthracene polymer

a) *Nc-AFM image (up) and constant-height STM image (bottom) of planar and hydrogenated anthracene polymer terminations (V_b = 5 mV).* ***b)*** *Differential conductance dI/dV curves acquired in the position indicated in a, where non-zero-bias features are observed.* ***c)*** *Chemical scheme of anthracene polymer. The rings filled in blue indicated the Clar sextets.* ***d)*** *Calculated PDOS for a finite chain of 15 units.*

Finally, we have paid special attention to the ends of the polymers. The majority of them have lost their terminal carbon (from the $=CBr_2$ after full debromination) and have been passivated by residual atomic hydrogen present in the UHV chamber (Figure 5.16a). Importantly, the chemical structure of the polymer ends is similar to the one described for the bulk of the polymer, being formed by planar aromatic anthracene units connected through ethynylene bridges. We have recorded d*I*/d*V* spectra at the terminal anthracene units of the polymer (Figure 5.16b), which allow to discard the presence of any feature close to Fermi level.

The comparison with the projected density of states of a finite polymer is in agreement with the experimental results and confirms the absence of an end state (Figure 5.16d).

Such results corroborate that ethynylene-bridged anthracene polymers is a topologically trivial insulator, as predicted by tight binding calculations in section 2.2.

In summary, by exploiting a novel homocoupling reaction based on anthraquinone precursors equipped with $=CBr_2$ functional groups, we have synthesized long, flexible and semiconducting ethynylene-linked anthracene polymers on Au(111).

5.4 Cumulene-like bridged pentacene polymers

The deposition of a submonolayer coverage of 4BrPn and subsequent annealing at 500 K on Au(111) leads to the formation of long wires formed by pentacene units. Once again, a competition between the ethynylene- and cumulene-like bridges is expected. Figure 5.17 shows the competition between the Kekulé structure with a migrating Clar sextet and the non-Kekulé structure with two migrating Clar sextets. In this case, the non-Kekulé structure (with open-shell character) with two Clar sextets becomes more favorable than in the anthracene case, due to the larger molecular size. The extent of the radical character of pentacene monomers is 7 % and increases for larger acenes (n > 6).[162,198,199] It is accepted that the pentacene molecule shows a closed-shell ground state, however when pentacene molecules form part of a π-conjugated polymer, the nature of their ground state can be modified. In fact, we will show in the following that this is the case for the pentacene polymers described below, whereby a quinoid cumulene-like resonance form is observed.

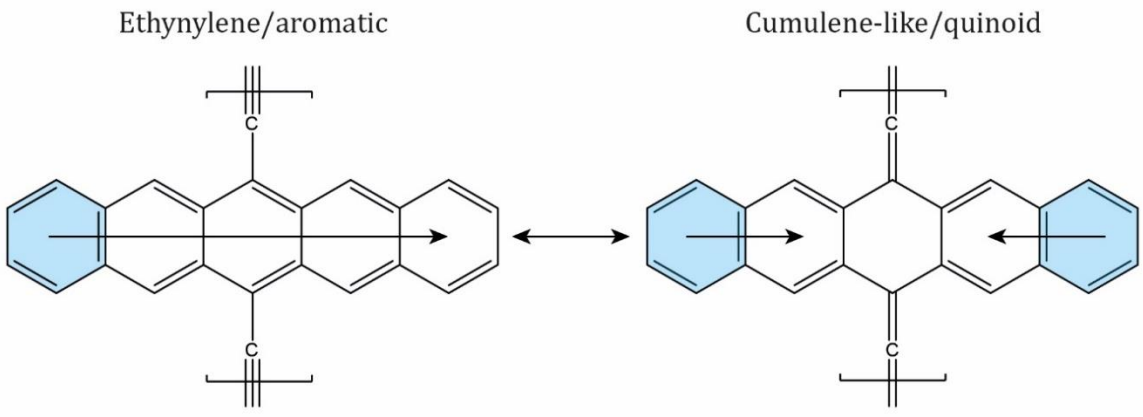

Figure 5-17. Scheme of the resonance form structures of pentacene polymer

Blue filled rings correspond to the Clar sextets.

Nc-AFM images of the pentacene polymers were acquired at several heights, in order to elucidate the chemical nature of polymers. The nc-AFM measurements reveal planar polymers formed by intact pentacene units. Figure 5.18 shows nc-AFM images acquired for the same pentacene polymer segment increasing sequentially the tip-sample distance by 15 pm from one image to another. In contrast to the bright protrusion at the middle of the bridge observed in nc-afm images for the previously described anthracene polymers (section 5.3), here the bridges connecting the pentacene units are characterized by a sharp line independently from the tip-sample distance , which suggests the formation of cumulene-like bridges connecting the pentacene units.[200] Interestingly, the formation of the cumulene-like bridges is in agreement with the quinoid resonance form of the pentacene backbone.

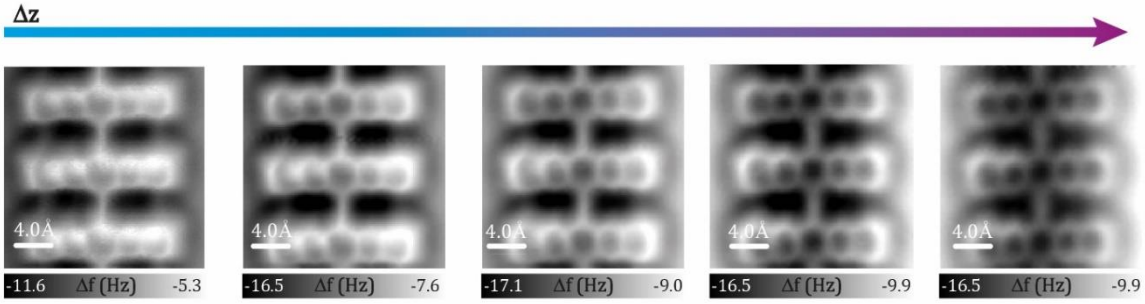

Figure 5-18. Elucidation of the cumulene-like character of the bridge

Nc-AFM high-resolution images of three consecutive double bonds (cumulene bridge) connecting pentacene units at sequentially 15 pm increasing tip height with a CO-functionalized tip (V_b = 3 mV).

In order to validate the experimental results obtained by nc-AFM measurements, DFT calculations of freestanding anthracene and pentacene polymers were performed. Figure 5.19a shows the bond length of selected carbon-carbon bonds. Importantly, the middle bond in the bridge of the anthracene polymers displays a bond length of 1.21 Å, shorter than the middle bond of the bridge of the pentacene case, which is of 1.24 Å. Furthermore, the bonds adjacent to the middle one are longer in the anthracene case (1.41 Å), reflecting their single character, in contrast to the shorter bonds of the pentacene case (1.36 Å). These calculations suggest a debilitation of the ethynylene bridges in the pentacene polymer and the increase of the cumulene-like character, as a consequence of the predominant quinoid resonance form of the pentacene unit. The variation in the bond

order of the bridges is also observed in the DFT calculated charge density distribution, as illustrated in Figure 5.19b. Large electron density distributed at a bond indicates its larger bond order, as we can see in the anthracene case where the ethynylene bonds are perfectly distinguished.[201,202] Contrary, an almost uniform charge distribution along the cumulene bridge is observed for the pentacene polymer. Altogether, such calculations are in agreement with the experimental measurements, where the increase of the cumulene-like character of the bridge in the pentacene polymer is observed.

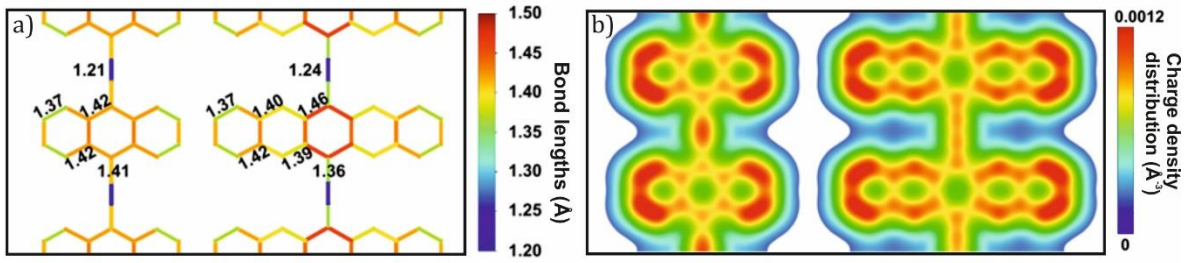

Figure 5-19. Bond length analyses and charge density distribution of anthracene and pentacene polymers from DFT simulations using hybrid B3LYP functional with periodic boundary condition

a) *Bond lengths obtained from DFT calculations with periodic boundary conditions.* ***b)*** *DFT calculated total charge density distributions.*

Next, we have investigated the electronic structure of the polymer, in order to assess the impact of the quinoid cumulene-like resonance form and the presence of larger acenes as constituent units in their electronic properties. Long chains formed by pentacene units connected through cumulene-like bridges are observed in the overview STM image of Figure 5.20a. First, we have elucidated the value of the band gap of the polymer by means of STS measurements. The dI/dV spectra show two resonances at -150 meV and +200 meV (as depicted in purple and green, respectively in Figure 5.20b), suggesting a narrow band gap of 0.35 eV. The bulk calculated PDOS shows dispersive conduction and valence bands (see Figure 5.20c). In addition, dI/dV maps of the freestanding pentacene polymer were simulated and compared with the experimental dI/dV maps acquired at the onset of the valence and conduction bands (Figure 5.20d-e). We observe how the simulations describe perfectly the features of the bands, corroborating our interpretation of the results.

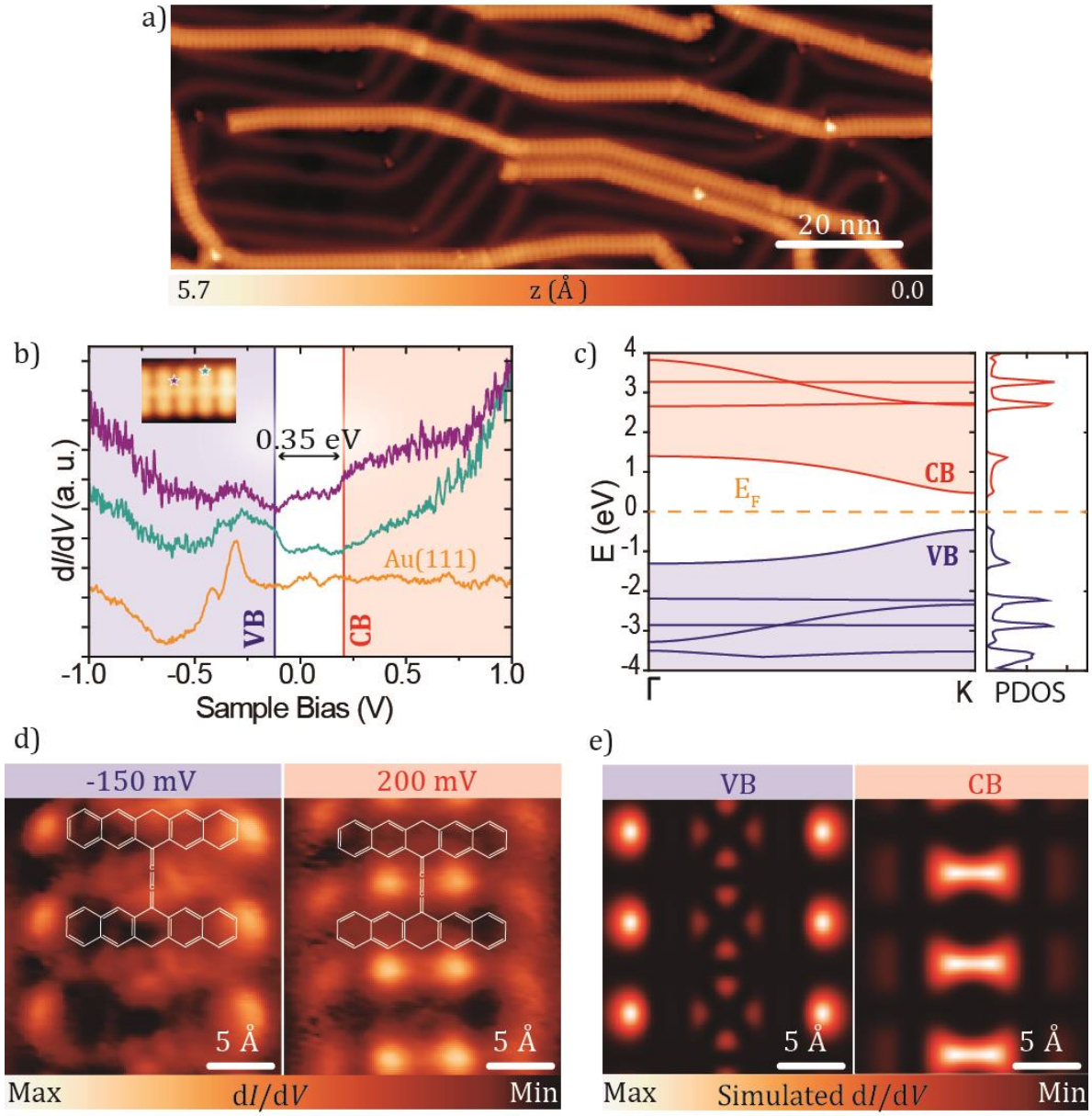

Figure 5-20. Experimental and theoretical results of the electronic structure of the pentacene polymer

a) *Overview STM image of cumulene-like bridged pentacene polymers on Au(111) (V_b= -0.8 V, I_t= 100 pA).* ***b)*** *STS measurements revealing the experimental value of the bandgap. The dI/dV curves were acquired at the positions depicted in the inset STM image.* ***c)*** *Bulk calculated band structure and projected density of states (PDOS).* ***d)*** *Constant-current dI/dV maps acquired at the energies of the VB (V_b= -150 mV) and CB (V_b= 200 mV).* ***e)*** *Simulated dI/dV maps of the freestanding pentacene polymer.*

Here it is worth to pay attention to the narrow band gap of 0.35 eV obtained from the experimental measurements. In order to assess its value, DFT and GW calculations were performed. DFT calculations provide a larger band gap, however these calculations

neglect the substrate effect and the electronic correlation of the polymer.[195–197] Importantly, GW calculations, which consider the electronic correlation, reveal an even narrower band gap of 0.05 eV.[203] This result looks strange since GW calculations does not include the substrate effect, and hence, we expected a larger value of the band gap than the experimental one. Tentatively, we assign this slight mismatch to the non-innocent role of the substrate, which increases the quinoid cumulene character of the pentacene polymer once adsorbed on the surface, thus displacing it slightly away from the topological transition point. As a result, it is expected that the free-standing pentacene polymer or simply the same polymer adsorbed on a distinct substrate could behave as a quasimetallic polymer.

As explained in section 2.2, the transition from a trivial to a non-trivial topological phase involves the closure of the band gap. The cumulene-like bridged pentacene polymer is expected to be a non-trivial topological insulator and to exhibit edge states.[34] To assess such topological class we have investigated the ends of the chains. First, we have confirmed the loss of the terminal C from the $=CBr_2$ functional group and the subsequent hydrogen passivation of the polymer ends by nc-AFM images (see Figure 5.21a). Next, we have performed STS measurements, which show a zero bias resonance at the polymer ends (Figure 5.21d). Tight binding calculations predict an exponential decay of such end state. However, our experimental results reveal that the maximum density of the states is located at the third unit and then decays towards the interior until it vanishes at the 8th unit (see Figure 5.21b). This effect is tentatively assigned to some relaxations of the polymers at the end, resulting in slight variations of the bond lengths. Figure 5.21c shows a TB simulated image of the charge distribution of a finite pentacene polymer of 40 units assuming some relaxations of the bond strengths of the bridges at the end of the polymer, which matches perfectly with the experimental STM image in Figure 5.21b. Interestingly, nc-AFM images acquired at the end of pentacene polymer show the presence of a faint protrusion in the middle of the latest bridges, which suggests an increasing ethynylene character of the bridge at the very end of the polymer.

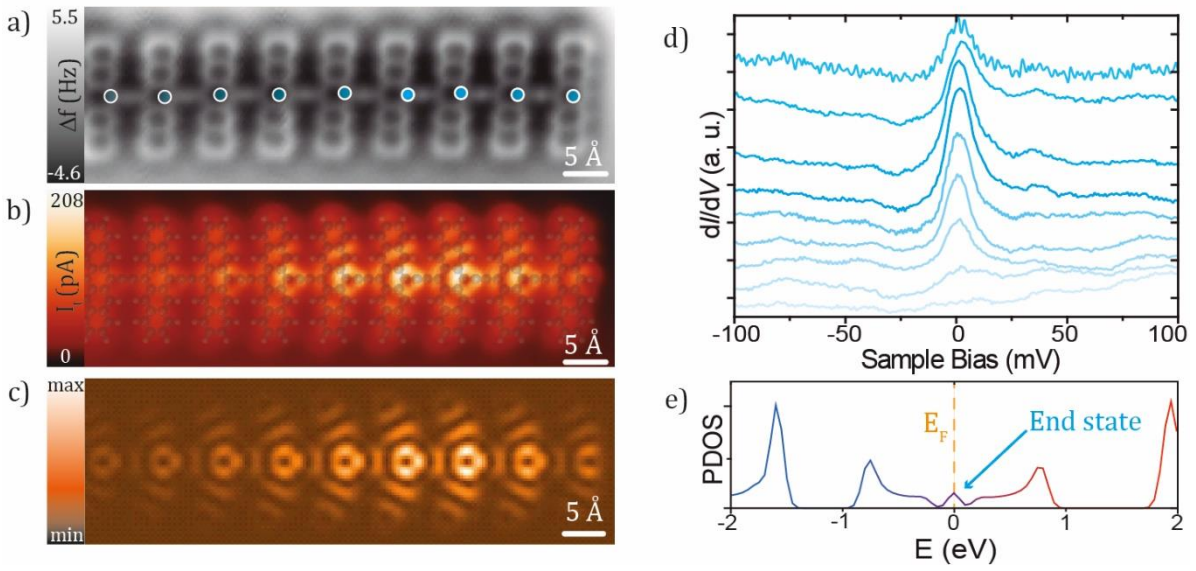

Figure 5-21. Experimental and theoretical results of the electronic structure at the ends of the pentacene polymer

a) *nc-AFM image acquired at the end of a pentacene polymer.* ***b)*** *Its corresponding constant-height STM image (V_b= 5 mV).* ***c)*** *TB simulated image of the charge density of a finite pentacene polymer with variations of the bond strengths at the polymer end.* ***d)*** *Differential conductance dI/dV curves acquired in the position depicted in* ***a)****, revealing a zero-bias feature.* ***e)*** *Calculated PDOS for a finite chain of 15 units confirming presence of an end-state.*

PDOS calculations for a finite pentacene polymer were performed (Figure 5.21e), finding the existence of an in-gap feature at the ends. Such an end state corroborates the non-trivial nature of the polymer and, together with the narrow band gap, its proximity to the topological transition.[30,204]

Finally, by comparing the experimental dI/dV maps of the anthracene and pentacene polymers we found an inversion of the frontier bands, reminiscent of the topological band transition between such polymers. This transition, from an aromatic ethynylene-like to a quinoid cumulene-like form, connects the frontiers bands of such resonance forms through a level crossing.[137,205] Such a crossover implies a closure of the band gap, as well as the transition from a trivial insulator to a topological insulator involves the crossing of the metallic phase. Thus, we reveal a fundamental connection between the resonance forms and the topological class of the polymer.

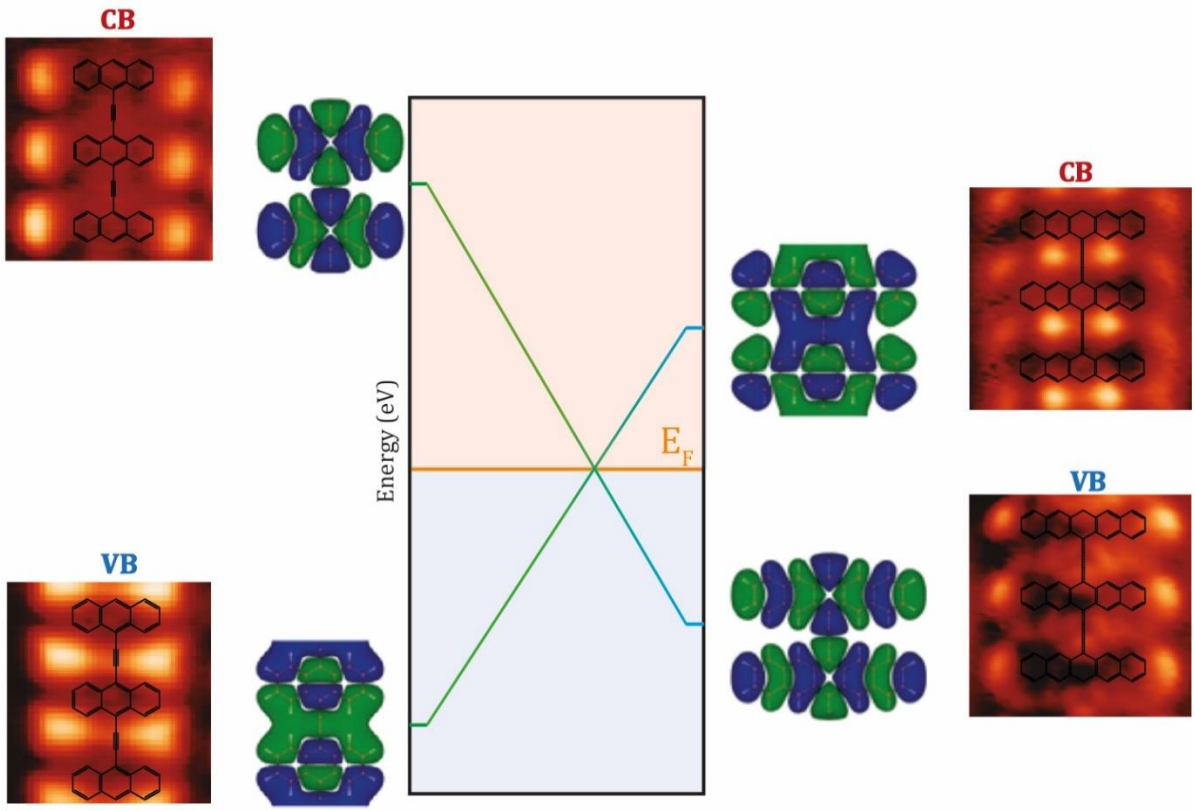

Figure 5-22. Crossing level mechanism at the K-edge between the anthracene and pentacene polymer

We rationalized the topological transition of the ethynylene- (aromatic)/cumulene-like (quinoid) character in π-conjugated polymers by the level crossing observed in the frontier orbitals, where orbitals of different symmetry swap (see Figure 5.22). An analysis of the character of such orbitals confirms our hypothesis. On one hand, for the anthracene case the highest-occupied wave function at K edge of the Brillouin zone shows π-bonding character in the triple bond, enhancing the ethynylene character of the bridge. On the other hand, the pentacene polymer stabilizes the wave function with the same symmetry as the lowest-unoccupied orbital, which weakens the triple bond. This change in the nodal character together with the small energy difference between the two resonance forms, allows the tuning of the resonance form of the π-conjugated polymers by the strategic design of the precursor.

Thus, we have demonstrated that polymers formed by acene-based precursors connected with each other through ethynylene/cumulene bridges are very interesting due to their π-electron network topology and our capacity to tune it by varying the acene

size. Here, we have shown two different cases: the ethynylene-bridged anthracene polymers with a dominant aromatic character and the cumulene-bridged pentacene polymer with an increasing quinoid character. On one hand, the anthracene polymer presents an aromatic backbone where π-electrons are mainly confined at the anthracene units and at the triple bonds. On the other hand, the pentacene polymer shows a quinoid backbone and an increased cumulene bridge character, altogether resulting in a more delocalization of the π-electrons, which gives rise to a narrower band gap.[206]

In summary, we have synthesized cumulene-like bridged pentacene polymers on Au(111). Notably, we have shown that by increasing the size of the acene units, the energy barrier to promote the transition from an aromatic backbone to a quinoidal one becomes smaller in larger acene-based polymers. In the case of pentacene it becomes small enough to promote a dominant quinoidal resonance form, modifying completely the electronic structure of the polymer, as compared to the anthracene polymer counterpart. Furthermore, we have shown that the stabilization of such resonance structure implies the level crossing of the frontier orbitals when compared to the anthracene polymer through a metallic phase. Such a crossover, results in the transformation of the polymer into a topological insulator, which features in-gap end states. Thus, we stablish a direct connection between the π-conjugation form of the polymer and its topological nature, which can be tunable by tailoring the size of the monomer.

5.5 Cumulene-like bridged bisanthene polymers

We have extended the synthetic route previously described to the periacene family and, in addition, we have proven the topological predictions from TB calculations for such family. Bisanthene polymers were synthesized by depositing a submonolayer coverage of 2(2BrAn) on Au(111) and subsequent annealing at 500 K in order to induce the dehalogenation, homocoupling and cyclodehydrogenation of the precursors. The reaction takes place successfully, obtaining high quality polymers similar to the case of the family of acene polymers. Here, we have also investigated the competition between ethynylene/aromatic and cumulene-like/quinoidal forms for polymers formed by repeating units of periacenes.

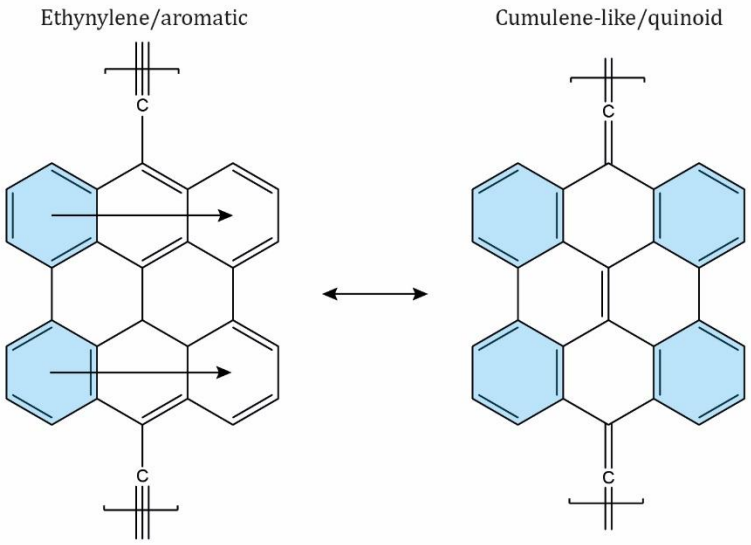

Figure 5-23. Scheme of the resonant form structures of the bisanthene polymer

Blue filled rings correspond to the Clar sextets.

Figure 5.23 shows for the bisanthene case two extreme resonance forms: the ethynylene/aromatic one featuring 2 migrating Clar sextets *versus* the cumulene/quinoid one with 4 Clar sextets. As we can see, more number of Clar sextets are formed in the cumulene/quinoid form, therefore it is expected a lower threshold that favors the stabilization of such form.[162] The competition between these two resonance forms resulting in a cumulene/quinoid character for the bisanthene polymer is described below.

Once more, we have elucidated the nature of the bridges and the polymer backbone by means of nc-AFM. Figure 5.24a shows several nc-AFM images at step heights of 15 pm of a couple of bisanthene units, which belong to a longer polymer (see Figure 5.24b). These images reveal the linear linkage connecting the bisanthene monomers, where the bridge appears as a sharp line with homogeneous contrast despite the tip-sample distance.[200] A slight enhancement in the contrast at the middle of the bridge is observed at the maximum tip-sample distance recorded (right image of Figure 5.24a), revealing a very small triple bond contribution. We tentatively assign the nature of the bond to an intermediate character between ethynylene and cumulene with major contribution of the cumulene form.[137] DFT calculations of the optimized freestanding bisanthene polymer reveal that the increasing length of the central bond of the bridge favours the

formation of three consecutive double bonds. These calculations show similar bond lengths between the pentacene (section 5.4) and the bisanthene polymers, concluding that both polymers are dominated by the quinoid/cumulene-like form.

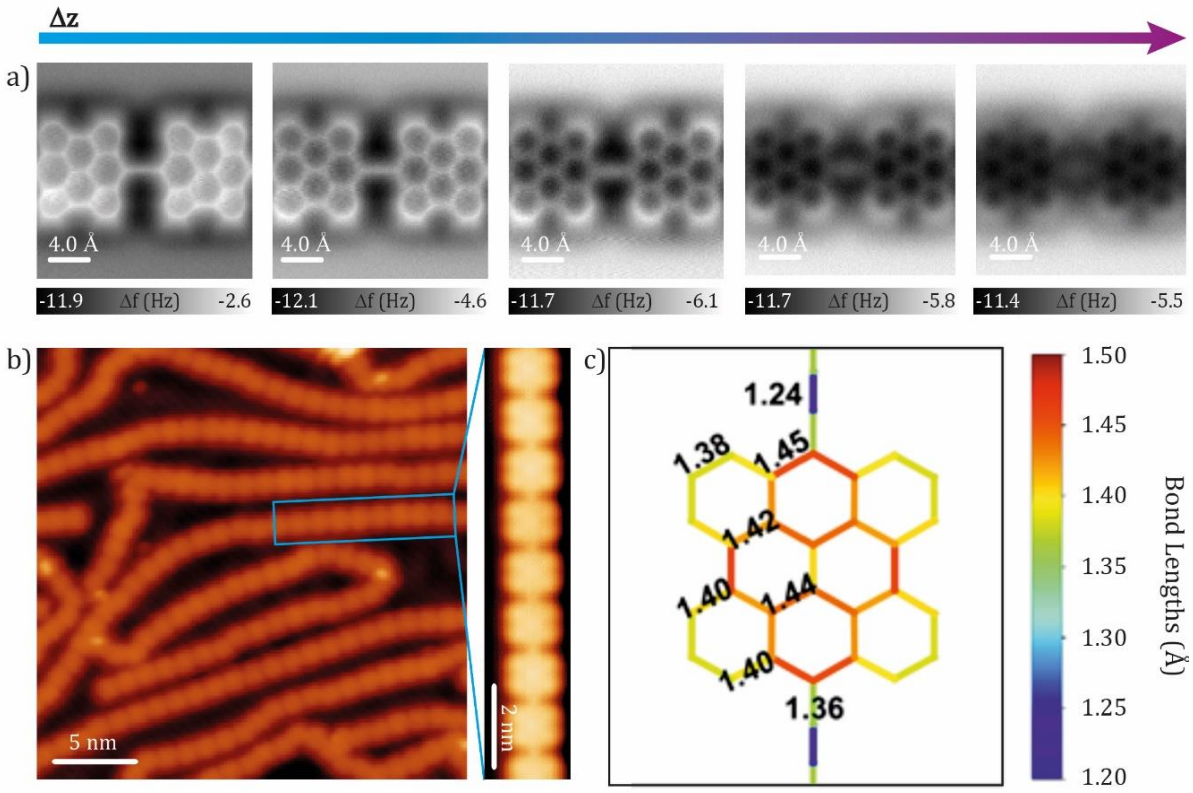

Figure 5-24. Elucidation of the cumulene-like character of the bridge

a) *Nc-AFM high-resolution images of three consecutive double bonds character of the bridge at different tip heights with a CO-functionalized tip (V_b = 10 mV).* ***b)*** *Overview STM image of high coverage bisanthene polymers on Au(111) after thermal annealing at 500 K. (V_b = 50 mV and It= 50 pA).* ***c)*** *Bond length analyses of bisanthene polymer from DFT simulations using hybrid B3LYP functional with periodic boundary conditions.*

The electronic structure of the polymer was investigated by means of STS. The differential conductance dI/dV spectra reveal strong peaks at -75 meV and 200 meV, assigned to the valence band maximum and the conductance band minimum, respectively. We obtain a very narrow experimental band gap of ≈ 0.3 eV (Figure 5.25a), even shorter than the band gap of the pentacene polymers. DFT calculations for an infinite polymer reveal dispersive valence and conductance bands, although exhibiting larger band gap energy (Figure 5.25b).[195,196] Like in the pentacene case, GW calculations of a freestanding bisanthene polymer display an almost negligible band gap (smaller than

0.05 eV), which suggests the quasimetallic behavior of such polymer. TB calculations predicted that the topological phase transition of the family of periacene is expected at the bisanthene polymer, supporting the very narrow band gap obtained by means of STS. The experimental measurements of the polymer reveals that it is located very close to the topological transition at the topological non-trivial region as we will show below.

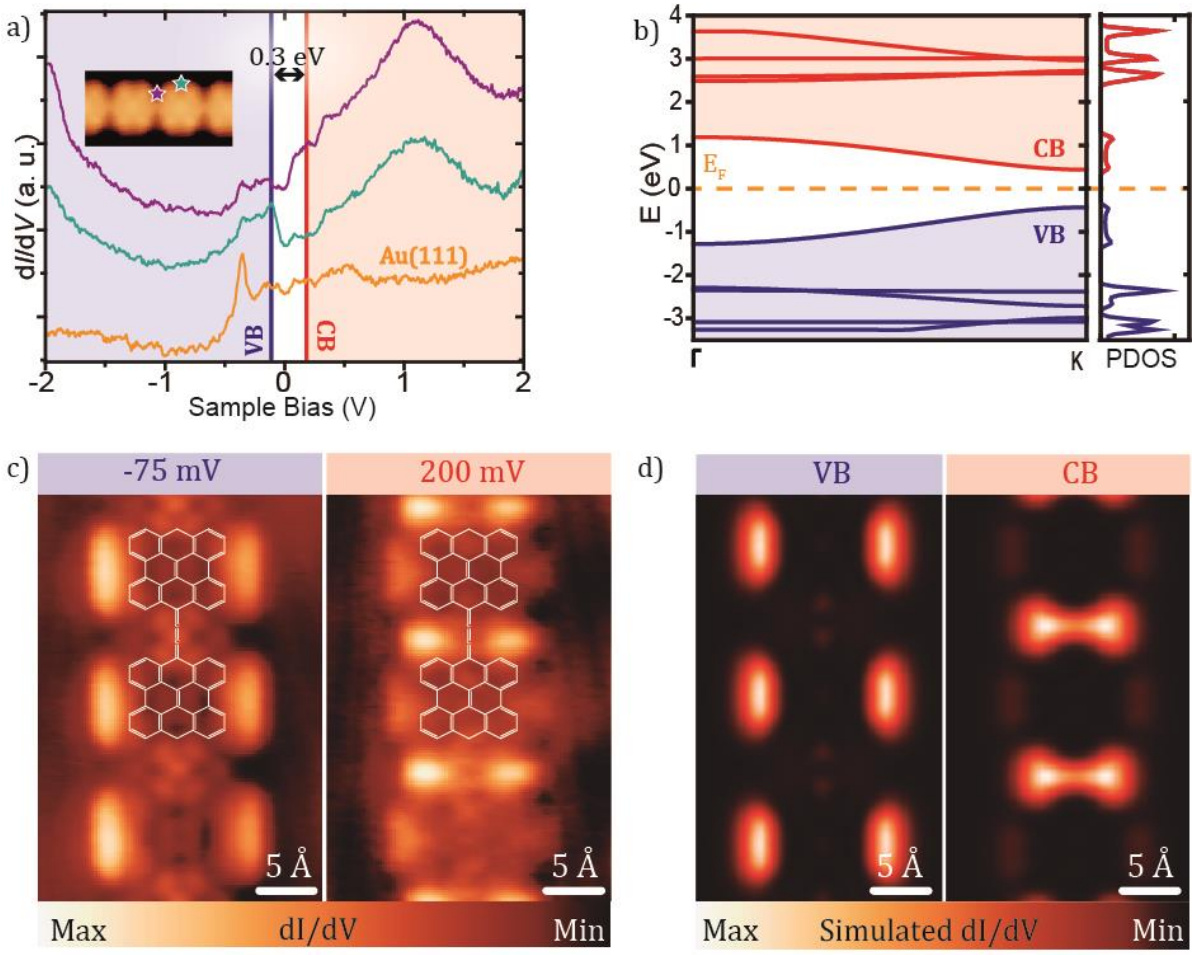

Figure 5-25. Experimental and theoretical results of the electronic structure of the bisanthene polymer

a) *STS measurements revealing the experimental value of the bandgap. The dI/dV curves were acquired at the positions depicted in the inset STM image.* ***b)*** *Bulk calculated band structure and projected density of states (PDOS).* ***c)*** *Constant-current dI/dV maps acquired at the energies of the VB (V_b= -75 mV) and CB (V_b= 200 mV).* ***d)*** *Simulated dI/dV maps of the freestanding bisanthene polymer.*

The dI/dV maps acquired at the energies of the frontier bands show the spatial distribution of such states (Figure 5.25c). More in detail, the dI/dV map acquired at -75 meV shows the largest LDOS at the bisanthene edges along the polymer, while the dI/dV map acquired at +200 meV shows the largest LDOS along the cumulene-like bridge and

its adjacent voids. Thus, the perfect agreement between simulated and experimental dI/dV maps (Figure 5.25d) allows the determination of the electronic structure of the bulk of the polymer.

Remarkably, we observed some analogies between the pentacene and the bisanthene polymers, like the predominant quinoid cumulene-like resonance form, the narrow electronic band gap and some resemblances of the valence and conduction bands, which in addition are supported by the DFT calculations. These analogies between pentacene and bisanthene polymers suggest that the bisanthene polymer belongs to the same topological quantum phase as the pentacene polymer and it is located close to the transition phase from trivial to non-trivial insulator of the periacene family, which would validate the tight binding predictions for the periacene family, simply taking into account slight deviations of the hopping parameters to match the cumulene-like character.

In order to study the topological nature of the bisanthene polymer, we have investigated the structural and electronic nature of the edges. The nc-AFM image recorded at a polymer end in Figure 5.26a confirms the loss of the terminal carbon from the $=CBr_2$ functional group and its subsequent atomic hydrogen passivation. STS measurements reveal the presence of in-gap states at the end of the polymer, which is in agreement with the DFT calculated PDOS for a finite bisanthene polymer (see Figure 5.26d). Figure 5.26b displays the dI/dV spectra acquired along the end of the chain, showing a disperse edge state extended along 3 or 4 units. Likewise the pentacene polymer, we do not observe an exponential decay from the end towards the bulk of the polymer, but a highest contrast at the second bisanthene unit, which decays towards the inner part of the polymer (see Figure 5.26c). Here, it is worth to highlight the shift of the end state towards higher energies and the broadening of the state with respect to the pentacene polymer. As previously reported for other nanomaterials, particularly for the 5-AGNR,[207] this upshifted end state is attributed to the electron transfer from the polymer to the gold surface, causing the emptying of the end states.[137,208]

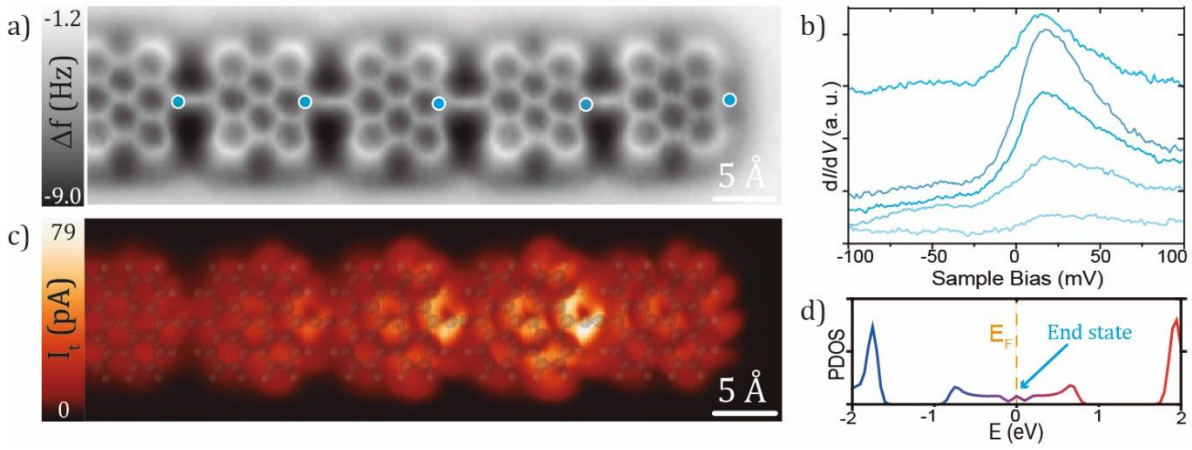

Figure 5-26. Experimental and theoretical results of the electronic structure at the ends of the bisanthene polymer

a) Nc-AFM image acquired at the end of a bisanthene polymer (V_b= 5 mV). ***b)*** *Differential conductance dI/dV curves acquired in the position indicated in* ***a)*** *revealing a zero-bias feature.* ***c)*** *Constant-height STM image of planar and hydrogenated bisanthene polymer termination (V_b= 5 mV).* ***d)*** *Calculated PDOS for a finite chain of 15 units confirming presence of an end-state.*

As mentioned above, the end state displays its maximum at the second unit and then decays towards the inner part of the polymer (Figure 5.27a). Like for the pentacene case, it is predicted to have the maximum at the end. However, small relaxations of the terminal monomers can shift this maximum, as we can see in Figure 5.27b in the TB simulated image of the charge density, where an increasing ethynylene character is forced at the end of the polymer. Such hypothesis is confirmed by nc-AFM, whereas there is an enhancement of the triple bond at the last units (see Figure 5.27c). This behavior is better visualized in the Laplace filtered nc-AFM image in Figure 5.27d, where the last bridge at the end of the polymer features a slightly less cumulene character than in the interior, which is manifested by the appearance of a slight protrusion.

In conclusion and in analogy to the pentacene polymer, the bisanthene polymer belongs to the topologically non-trivial quantum phase and is located close to the transition phase where the competition between the two possible resonance forms is observed, while featuring a quasimetallic band gap.

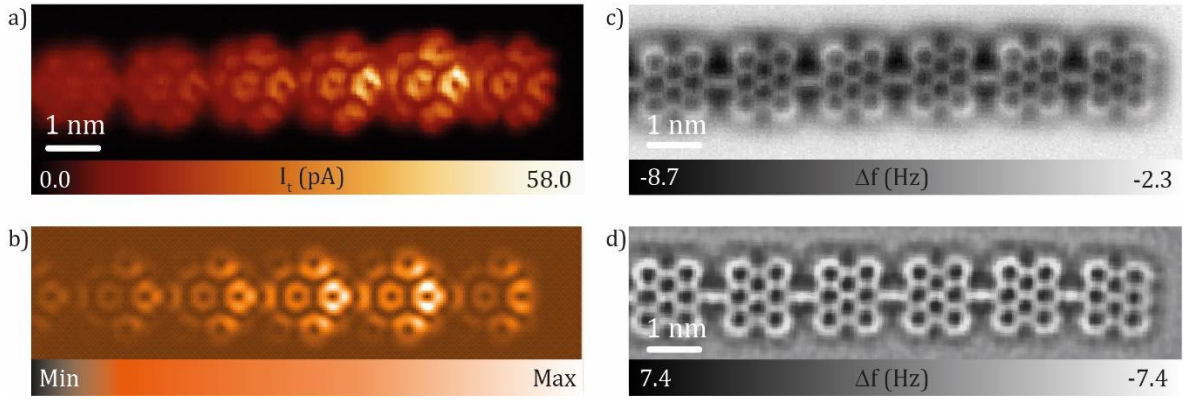

Figure 5-27. Inspection of the ends of a bisanthene polymer

a) *Constant-height STM image of planar and hydrogenated pentacene polymer termination (V_b = 5 mV).* ***b)*** *TB simulated image of the charge density of a finite bisanthene polymer with variations of the bond strengths at the polymer end* ***c)*** *Nc-AFM image.* ***d)*** *Laplace filtered nc-AFM image (V_b = 5 mV).*

5.6 Cumulene-like bridged peripentacene polymers

In order to explore the family of peripentacene polymers in the non-trivial topological regime, we have moved a step further away from the topological transition with respect to the bisanthene polymer, synthesizing bridged peripentacene-based polymers.[135] To this aim, the deposition of the 2(2BrPn) precursor on Au(111) and subsequent annealing at 450 K leads to the formation of planar peripentacene oligomers and polymers.

The peripentacene monomer is a highly reactive compound due to its radical character.[160,209] Here, the stabilization of the non-Kekulé structure with 5 Clar sextets per peripentacene unit results more favorable that the stabilization of the Kekulé structure with a closed-shell ground state (with 2 migrating Clar sextets, see Figure 5.28). The energetically favorable open-shell structure leads to the stabilization of the quinoid/cumulene-like bridge resonance form, which is in agreement to bisanthene polymers described in section 5.5. In fact, the predominant quinoid/cumulene-like form is expected to increase for larger periacenes units.

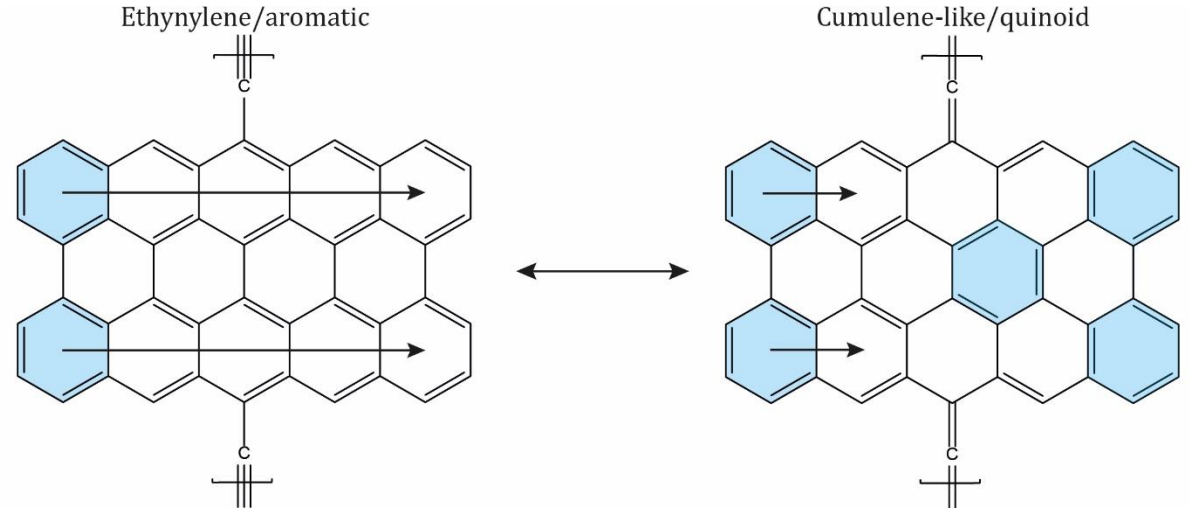

Figure 5-28. Scheme of the resonance form structures of peripentacene polymer

Blue filled rings correspond to the Clar sextets.

First, we have observed a dependence between the length of the polymer and the annealing time. This effect was not observed during the synthesis of the other polymers, where they tend to form long wires even at short annealing times (5-10 minutes). To illustrate such dependence, we have annealed different samples with similar coverage at 450 K for 5, 30 and 180 minutes. Overview STM images of the prepared samples are shown in Figure 5.29a**,** where the difference in the polymer length is clearly observed. Figure 5.29c shows a graph containing the different length of the polymers (counting the number of units forming the oligomers or polymers) as a function of the annealing time. The graph reveals a tunable average length from 4.5 nm for 5 minutes of annealing time to 14.5 nm for 180 minutes.

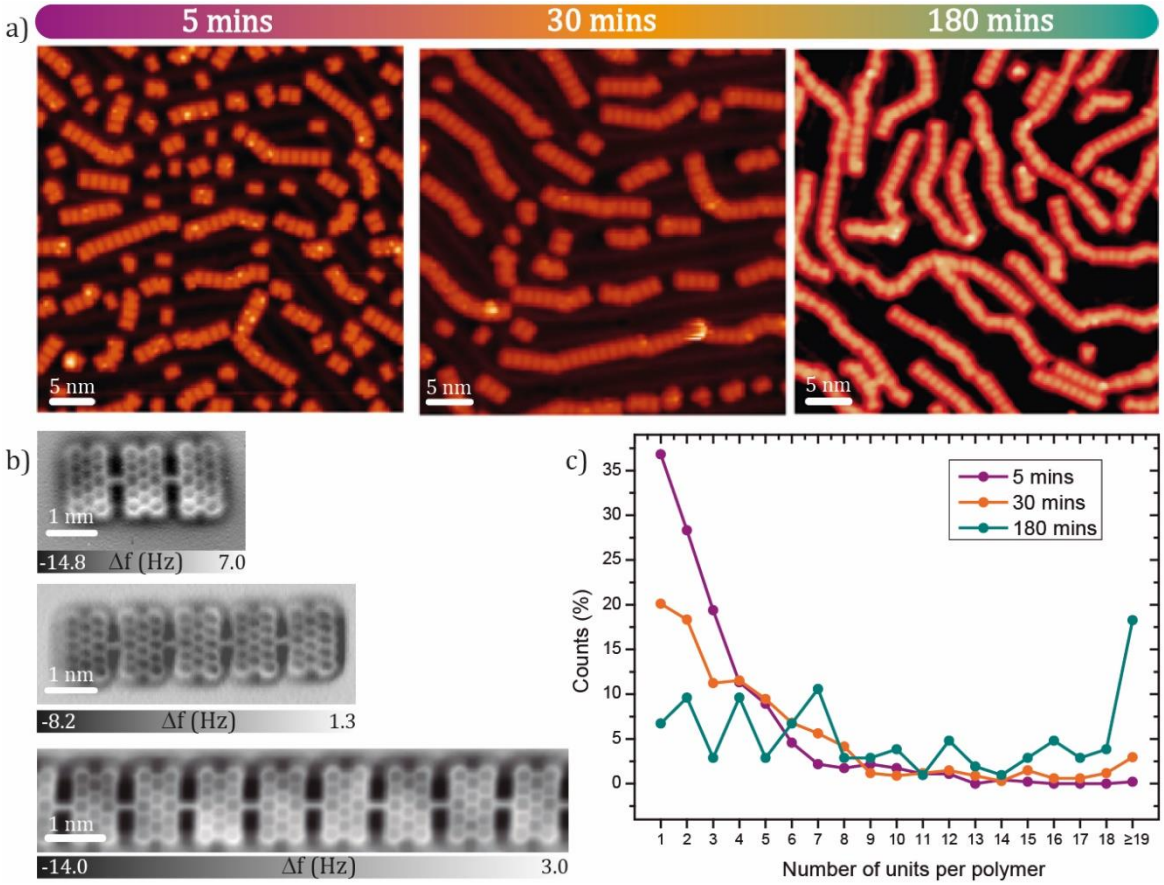

Figure 5-29. Length dependence of the peripentacene polymers with thermal annealing time

a) *Overview constant-current STM images of distinct samples after different annealing times at 180 °C. Image at the left panel: t = 5 mins, V_b = 0.2 V and I_t = 25 pA; image at the middle panel: t = 30 mins, V_b = 0.2 V and I_t = 100 pA; image at the right panel: t = 180 mins, V_b = 0.4 V and I_t = 100 pA.* ***b)*** *high-resolution nc-AFM images of peripentacene trimer, pentamer and polymer (all nc-AFM images acquired with V_b = 3 mV).* ***c)*** *Graph displaying the polymer length as a function of the annealing time of the sample at 450 K.*

Next, we have inspected the chemical nature of the polymers *via* nc-AFM measurements. Constant-height nc-AFM images reveal planar peripentacene units connected by linear and homogeneous bridges. We do not distinguish any contrast enhancement in the middle of the bridge by varying the tip-sample distance, therefore we conclude that the cumulene/quinoid is the predominant resonance form. The character of the bridge cannot be 100 % cumulene, due to bond relaxations that tends to avoid a BLA = 0.[210–212] In addition, we have investigated the chemical nature of the bridge for the different lengths of the polymers. Figure 5.29b shows nc-AFM images of a trimer, a pentamer and a long polymer (>19 units), where homogeneous bridges, detected in all cases as a sharp line connecting the peripentacene units are observed. Thus, within the limitations of nc-

AFM, the cumulene character does not depend on the length of the peripentacene oligomer/polymer.

Then, we have inspected the electronic properties at the bulk of the peripentacene polymer by means of STS. dI/dV curves show two strong resonances in the density of states at -0.4 eV and +0.4 eV, which are tentatively assigned to the onsets of the valence and conductance bands, respectively (see Figure 5.30a). The STS measurements reveal an experimental band gap of ≈ 0.8 eV, larger than the band gap obtained for the bisanthene polymer, in agreement with the TB calculations shown in the section 2.2, which predicted the increase of the band gap energy of the polymers after crossing and moving away from the topological transition. DFT calculations of the PDOS of an infinite peripentacene polymer reveal the non-dispersive behavior of the bands, which are almost flat (Figure 5.30b). This non dispersive behavior corroborates the negligible variation of the band gap (0.8 eV) with respect to the length of the polymer experimentally observed. We have acquired the dI/dV maps at the energies of the edges of valence and the conductance bands (shown in Figure 5.30c at -0.4 eV and +0.7 eV, respectively) in order to visualize their spatial distribution. The features of the bands are very similar to the ones observed for the bisanthene polymer, with the CB located at the adjacent voids of the cumulene-like bond and the VB visualized as two lobes at the transversal molecular boundaries. DFT simulated dI/dV maps of a freestanding peripentacene polymer support our experimental results (Figure 5.30d) and corroborate our interpretation of the electronic structure of the peripentacene polymers.

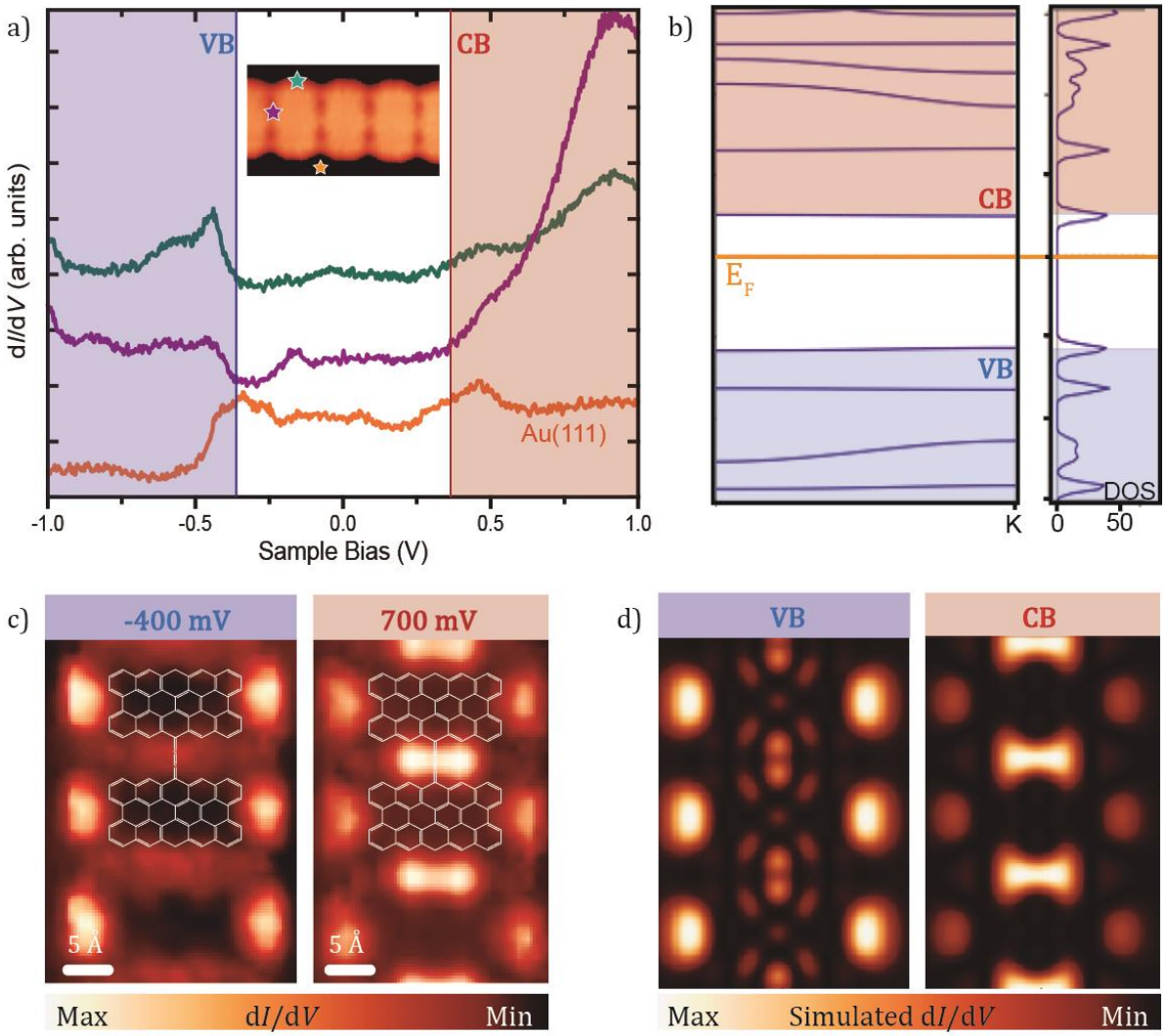

Figure 5-30. Experimental and theoretical results of the electronic structure of the peripentacene polymer

a) *STS measurements revealing the experimental value of the band gap. The dI/dV curves were acquired at the positions depicted in the inset STM image.* ***b)*** *Bulk calculated band structure and projected density of states (PDOS).* ***c)*** *Constant-current dI/dV maps acquired at the energies of the VB (V_b = -400 mV) and CB (V_b = 700 mV).* ***d)*** *Simulated dI/dV maps of the freestanding peripentacene polymer.*

We have also recorded differential conductance spectra (dI/dV) at the polymer ends, in order to investigate the presence of end states and confirm the topological predictions described in section 2.2. STM images acquired at constant height with a CO-functionalized tip and at low bias voltages (3 mV) show an enhancement of the LDOS at the longitudinal edges of the polymer chains independently of their length (see Figure 5.31a). In contrast to the pentacene and bisanthene polymer, these features are localized only at the edge of the last unit of the polymers and vanished in the neighboring of the area, due to the higher band gap. The dI/dV spectra acquired at the brightest areas show

a strong and very narrow zero-bias peak (Figure 5.31c). We attribute this spectral feature to a Kondo resonance that results from the presence of a localized magnetic impurity located at the topological end state, which is screened by a sea of electrons coming from the conduction electrons of the Au(111).[213,214]

To proof the nature of the Kondo feature we measured the variation in the HWHM (half width at half medium) with the temperature of a peripentacene hexamer *via* dI/dV spectroscopy (see Figure 5.31d).[215,216] The peaks were fitted to a Frota function (Equation 5.1) in order to calculate the HWHM at the different temperatures.[217] The fitting of the peaks were corrected taking into account a linear background and a slight offset of the sample bias voltage (parameters a and b from Equation 5.1).

$$\frac{dI}{dV}(V) = a + bV + A\left[-ie^{i\cdot\Phi}\cdot\sqrt{\frac{(0.39i\Delta)}{(eV-\mathcal{E})+(0.39i\Delta)}}\right] \qquad (5.1)$$

Where A corresponds to the amplitude of the peak, Φ the lineshape, $\mathcal{E}$ the center position of the energy peak and Δ the half width at half maximum (HWHM).

The extracted HWHM was corrected in order to calculate the effective half width at half medium (Γ) with Equation 5.2 taking into account the finite temperature of the tip:[218]

$$\Gamma = \sqrt{\Delta^2 - \Delta_{tip}^2} \qquad (5.2)$$

Where $\Delta_{tip} = \frac{1}{2}K_B\cdot T$, $K_B = 8.6173324\cdot 10^{-5}$ eV/K and Δ is the HWHM. Then, we have considered the broadening of the Kondo peak produced by the lock-in amplifier by recalculating the effective temperature for every measurement temperature with Equation 5.3,[218] using a V_{rms} of 0.8 mV.

$$T_{eff} = \frac{1}{5.4\cdot K_B}\sqrt{(5.4\cdot K_B\cdot T)^2 + (1.7\cdot V_{rms})^2} \qquad (5.3)$$

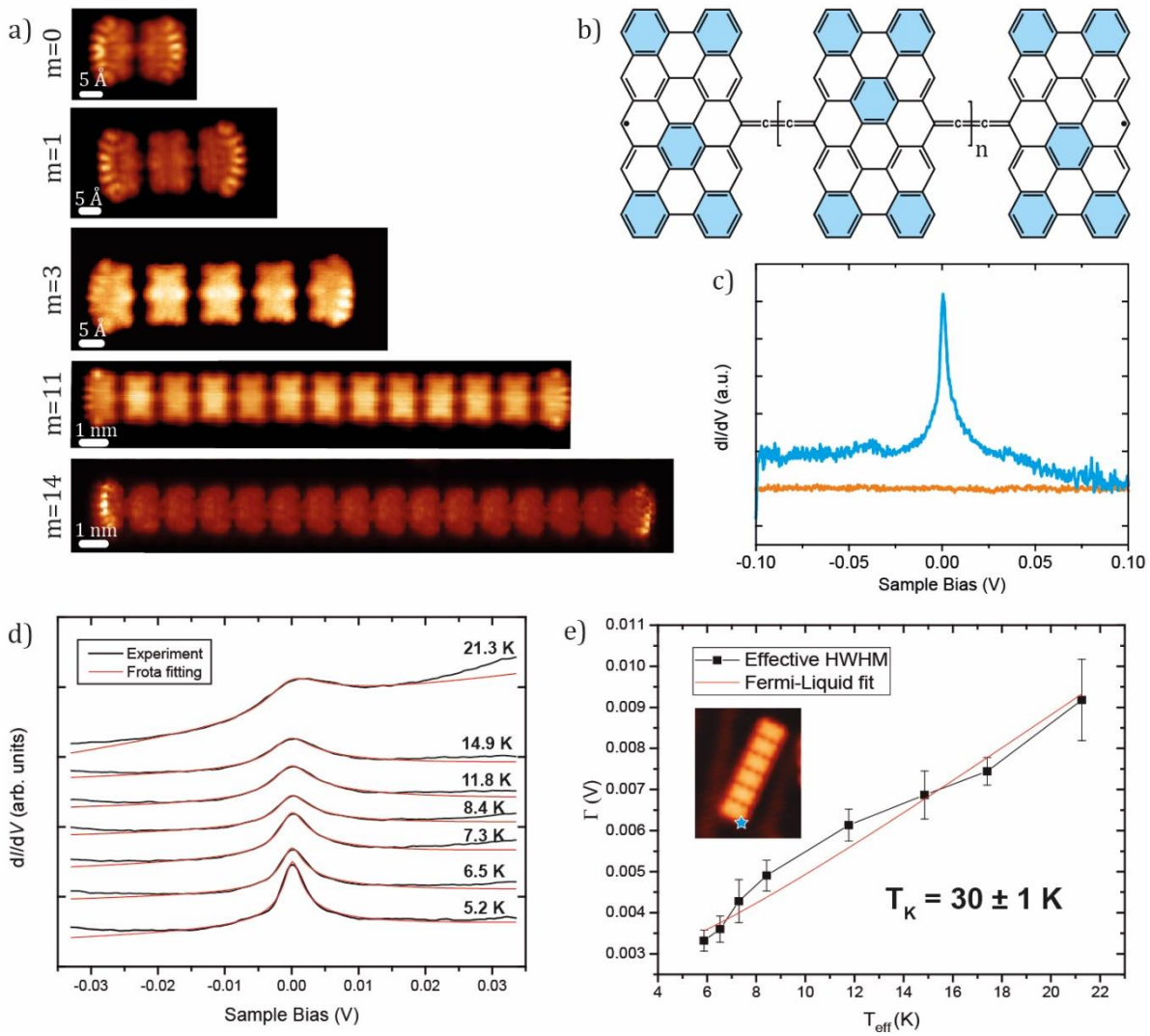

Figure 5-31. Assessment of Kondo phenomena in diradical peripentacene oligomers and polymers

a) *Show constang-height STM images of peripentacene oligomers and polymers revealing an enhancement of the LDOS at the end of the chains (V_b = 3 mV).* ***b)*** *chemical sketch of the general expression for the peripentacene linked by cumulene bridges polymers family with diradical character. Blue filled ring denote Clar sextets.* ***c)*** *dI/dV curve acquired at the end of a peripentacene polymer at the position depicted in* ***a)*** *with V_{rms} = 0.4 mV. Blue curve reveals a strong and narrow zero-bias peak.* ***d)*** *Evolution of the Kondo renonance of a hexamer with the temperature (black lines) and the corresponding frota function fitting (red lines) (V_{rms} = 0.8 mV). The dI/dV curves were acquired on top of the grey mark of the STM image of the hexamer inserted in* ***e)****.* ***e)*** *Γ (effective half width at half maximum) extracted from* ***d)*** *as a function of the temperature. The evolution was fitted using a Fermi-Liquid model ($\Gamma(T) = \frac{1}{2} \cdot \sqrt{(\alpha \cdot K_B \cdot T)^2 + (2 \cdot K_B \cdot T_B)^2}$),[219] where T_K = 30 K and α = 9.8.*

The dependence of effective HWHM with the effective temperature was fitted to Fermi-liquid model (Equation 5.4),[219] which allows to extract a tentative Kondo temperature of the system.

$$\Gamma(T) = \frac{1}{2} \cdot \sqrt{\left(\alpha \cdot K_B \cdot T_{eff}\right)^2 + (2 \cdot K_B \cdot T_B)^2)} \qquad (5.4)$$

Figure 5.31e shows the evolution of the effective HWHM with T_{eff}, which follows the characteristic behavior of a Kondo screened state. The Kondo temperature predicted from the HWHM broadening with the increase of the temperature is T_K = 30 ± 1 K. Therefore, we conclude that the zero-bias resonance correspond to a Kondo signal, which matches perfectly with the radical character predicted for such polymer. Figure 5.31b shows the chemical scheme of the cumulene-bridged peripentacene polymers and the diradical character at the edges of the polymer.

Finally, we have studied the exchange coupling of the unpaired electrons at the edges with respect to the length of the polymer. Figure 5.32a shows the dI/dV spectra acquired at the edge of a dimer. Notably, such spectra show a symmetrical split peak around zero-bias, with the onset around +2.5 meV and -2.5 meV. In contrast, the dI/dV spectra recorded at the edges of a trimer reveal a pronounced zero-bias peak at each side (Figure 5.32b). Theoretical calculations employing distinct methods predict an open-shell singlet ground state. Mean Field Hubbard Tight Binding (MFH-TB) calculations reveal an energy difference of 3.3 meV between the singlet and triplet states for the dimer. In addition, the nature of the ground state of the dimer was studied using high-level wave function-based electronic structure theory, i.e. *ab initio* density matrix renormalization group (DMRG) calculations. These calculations confirmed the singlet ground state of the peripentacene dimers, with a singlet-triplet gap of 3.5 meV. Thus, we assign the split-peak measured in the dimer to a singlet-triplet inelastic spin excitation that changes the total spin of the two exchange coupled spins of the dimer, being induced by tunneling electrons coming from the tip.[220–222] The strength of the exchange coupling J_{eff} between the spins in the dimer can be experimentally calculated from the onsets of the split peak with respect to Fermi energy, revealing a J_{eff} = 2.5 meV, which is reasonably close to the calculated value (3.3 meV).

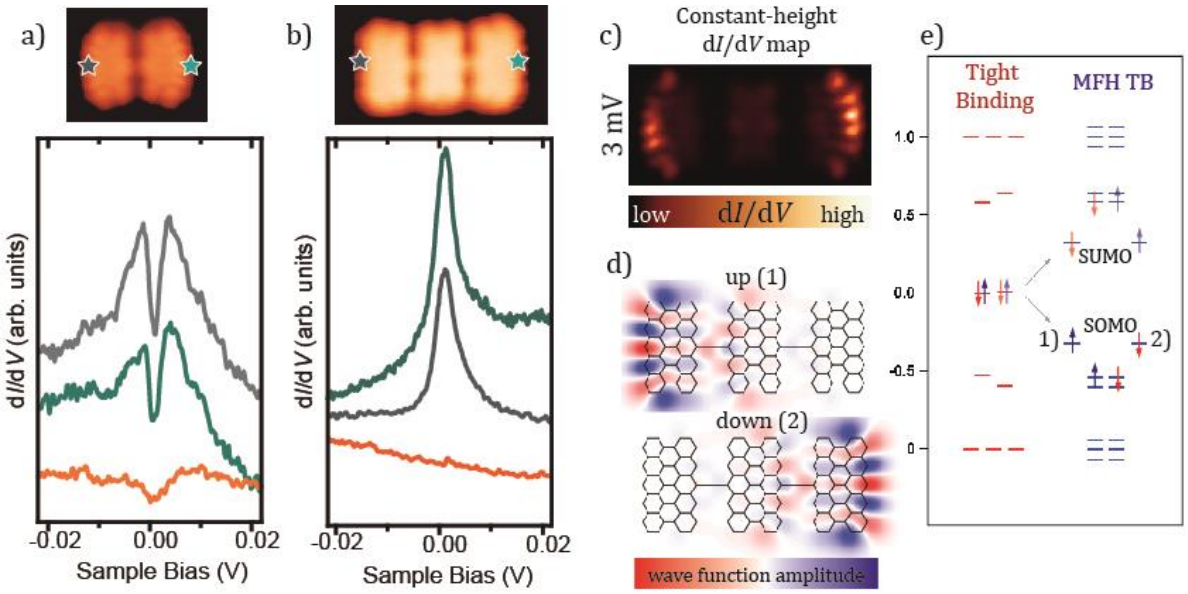

Figure 5-32. Characterization of the magnetic properties of a peripentacene dimer and trimer

a) *Split-peak dI/dV features acquired at the ends of a dimer and assigned to singlet–triplet inelastic excitations. The spectra were acquired in the positions depicted in the upper STM image (V_b = 50 mV and I_t = 100 pA).* ***b)*** *Zero-bias resonances acquired at the ends of a trimer and assigned to Kondo signals. The spectra were acquired in the positions depicted in the upper STM image (V_b = 100 mV and I_t = 100 pA).* ***c)*** *Constant-hieght dI/dV maps of a trimer acquired at 3 mV.* ***d)*** *Spin resolved wave-function plots of the singly occupied frontier orbitals of a trimer by MFH-TB.* ***e)*** *Spin-density distribution of a peripentacene trimer from TB and MFH-TB calculations.*

The theoretical calculations predict the vanishing of the exchange coupling from oligomers longer than trimers. In fact, the Kondo signal measured at edges of the trimer confirms that the exchange coupling between the unpaired spins in the peripentacene trimer is negligible. The experimental results and the calculations lead us to conclude that there is a transition in the magnetic properties from dimer to trimer (and longer oligomers and polymers), where the dimers show an antiferromagnetic coupling, while longer oligomers and polymers a paramagnetic behavior.

We can conclude that in the case of peripentacene polymers the end state is located below Fermi level in the occupied states region, being populated with just one electron, thus giving rise to the Kondo effect. As a result, with local STS we probe the Kondo effect arising from the scattering of such unpaired electron by the Au(111) electronic cloud for polymers and oligomers longer than dimers (Figure 5.31c and Figure 5.32b, respectively). Importantly, the imaging of the spatial distribution of such resonance,

shown in Figure 5.32c, has the same shape of the calculated SOMO (see Figure 5.32d and diagram in Figure 5.32e), and corroborates its existence, as previously found for other molecules adsorbed both on graphene and metals.[55,223]

In summary, we have described the on-surface synthesis of cumulene-bridged peripentacene polymers. Notably, we have revealed that such polymer also belongs to the non-trivial topological class as bisanthene polymer. However, in this case, the localization of the edge state in the HOMO region, results in a singly occupation. As a result, there are two unpaired spins at the edges. For dimers such spins are antiferromagnetically coupled with a small exchange interaction of 2.5 meV, which vanishes for longer oligomers that become paramagnetic. Therefore, we have demonstrated the diradical character of the cumulene-bridged peripentacene oligomers and polymers.

5.7 Towards the synthesis of ladder polymers containing pentalene units

All the polymers described above were synthesized after annealing the samples to 450-500 K. At this stage, it is interesting to investigate the thermal robustness of such polymers and if we can induce an additional reaction by a further annealing step. Figure 5.33 summarizes the reactions induced after annealing at around 600 K the anthracene (section 5.3), the pentacene (section 5.4), the bisanthene (section 5.5) and the peripentacene (section 5.6) polymers.

Figure 5.33a shows the intact ethynylene-bridged anthracene polymer after the annealing to 600 K, except for the presence of a fused segment (white square in Figure 5.33a). The STM image acquired in constant-height mode with a CO functionalized tip (inset in Figure 5.33a) allows to resolve the molecular structure of this polymer segment, where the formation of a pentalene bridge (two fused cyclopentadiene rings) *via* double dehydrogenation and cyclization is observed. However, the low content of pentalene bridges demonstrates the low success of such reaction. In addition, further annealing to 700 K induces the almost complete dissociation of the C-H bonds favoring other reactions and resulting in a dendritic growth of the polymer.

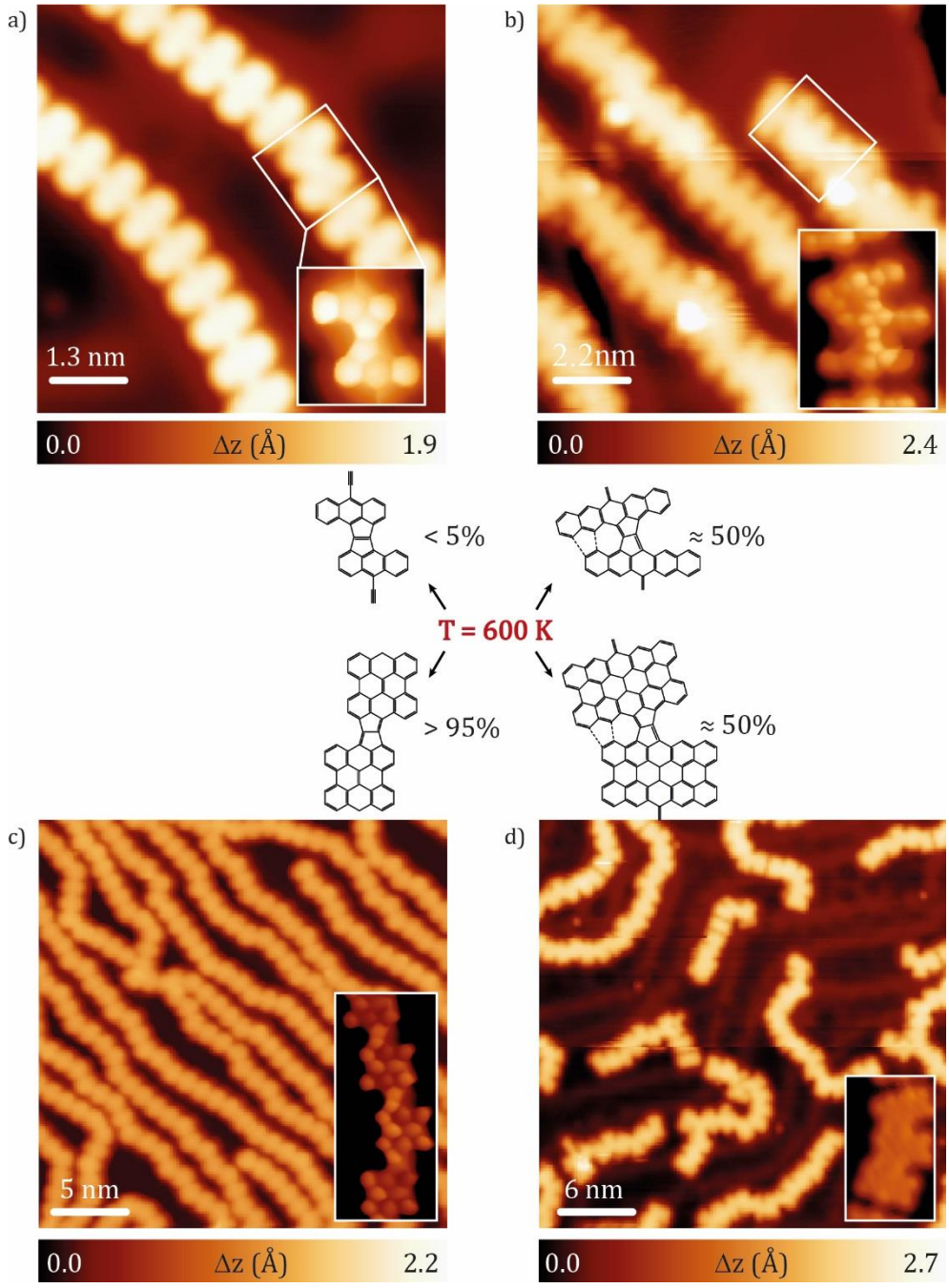

Figure 5-33. New reactions induced after thermal annealing to 600 K of acene and periacene polymers ***a)***, ***b)***, ***c)*** *and* ***d)*** *correspond to overview STM images after annealing to 600 K the anthracene (V_b = 20 mV and I_t = 100 pA), pentacene (V_b = 1.0 V and I_t = 150 pA), bisanthene (V_b = 1.0 V and I_t = 50 pA) and peripentacene (V_b = 50 mV and I_t = 50 pA) polymers, respectively. The inset images are constant-height STM images acquired with CO-tip resolving the chemical structure. The chemical scheme at the middle panel summarizes the reactions that are taking place.*

Next, the reactions induced after annealing the pentacene and peripentacene polymers, are shown in Figure 5.33b-d. The observed reaction is similar for both polymers, where

the larger size of the backbone (n=5), in comparison with the anthracene and bisanthene polymers (n=3), plays an important role. For these cases, the percentage of pentalene bridges in between the units is higher than for the anthracene polymer. However, the annealing of the sample at 600 K also induces a concomitant reaction in the external rings (dashed lines in chemical sketch) forming an azulene bridge (fused cyclopentadiene and cycloheptatriene). Although the formation of azulene bridges is interesting,[224–227] such reaction induces the curvature of the polymer , blocking further reactions.

Finally, an STM image showing the annealing to 600 K of the bisanthene polymer is displayed in Figure 5.33c. Interestingly, the successful formation of pentalene bridges connecting the bisanthene units takes places with a yield > 95%, giving rise to the ladderization of the polymer and the formation of a pentalene-bridged bisanthene polymer.[228,229] Such polymer belongs to the family of the ladder polymers, which are described as a type of polymers in which all the units of the main-chain are π-conjugated and fused. Furthermore, the presence of non-benzenoid rings predicts different π-electron density distribution and a tendency towards open-shell structures.[230–232]

A different reaction mechanism for the ethynylene-bridged anthracene polymer and the cumulene-bridged bisanthene polymer after higher thermal annealing to 600 K is observed. Theoretical calculations of the reaction pathways of the anthracene polymer and the biasanthene polymer do not reveal relevant differences in the energy barriers of the reaction. However, the experimental measurements evidence the viability of such reaction only for the bisanthene case. In addition, the pentacene and peripentacene polymers also show certain affinity towards the ladderization, though such reaction is frustrated for steric effects.

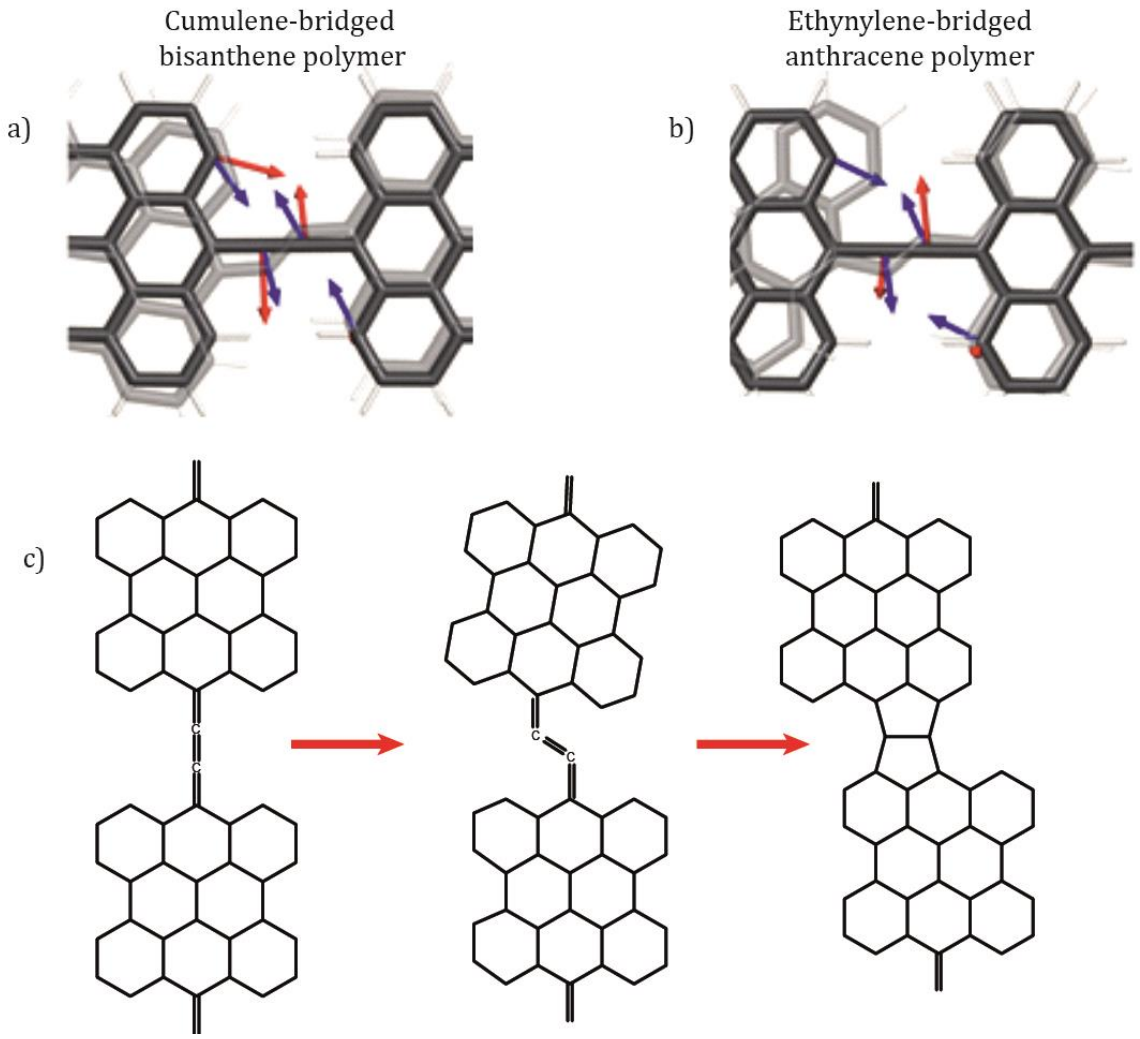

Figure 5-34. Comparison of calculated vibrational modes and reaction pathways of ethynylene-bridged anthracene polymer and cumulene-bridged bisanthene polymer towards ladderization

a) *and* ***b)*** *show the comparison of calculated vibrational mode (red arrows) and reaction coordinates (blue arrows) of bisanthene polymer and anthracene polymer, respectively. The transition state of the reaction pathway calculated is represented in transparent mode.* ***c)*** *Chemical sketch of the bending modes of bisanthene polymer towards the formation of pentalene bridges.*

The low flexibility of the ethynylene bridges in the anthracene polymer together with the localized π-electrons avoid the promotion towards the formation of pentalene bridges. In the case of the polymers featuring cumulene bridges specific bending vibrational modes favor the formation of pentalene bridges (see Figure 5.34a). Contrary, the vibrational modes of the ethynylene-bridged anthracene polymer present a lack of coupling towards the formation of the pentalene bridge (see Figure 5.34b). Therefore, we conclude that the bending vibrational modes of the cumulene-bridged bisanthene

polymer together with the subsequent thermal annealing lead to the intrapolymeric cyclization reactions giving rise to the formation of the pentalene bridges (scheme in Figure 5.34b). Here, we have demonstrated the important role of the vibrational modes for the viability of some reactions,[233–235] complementing the conventional transition state theory.

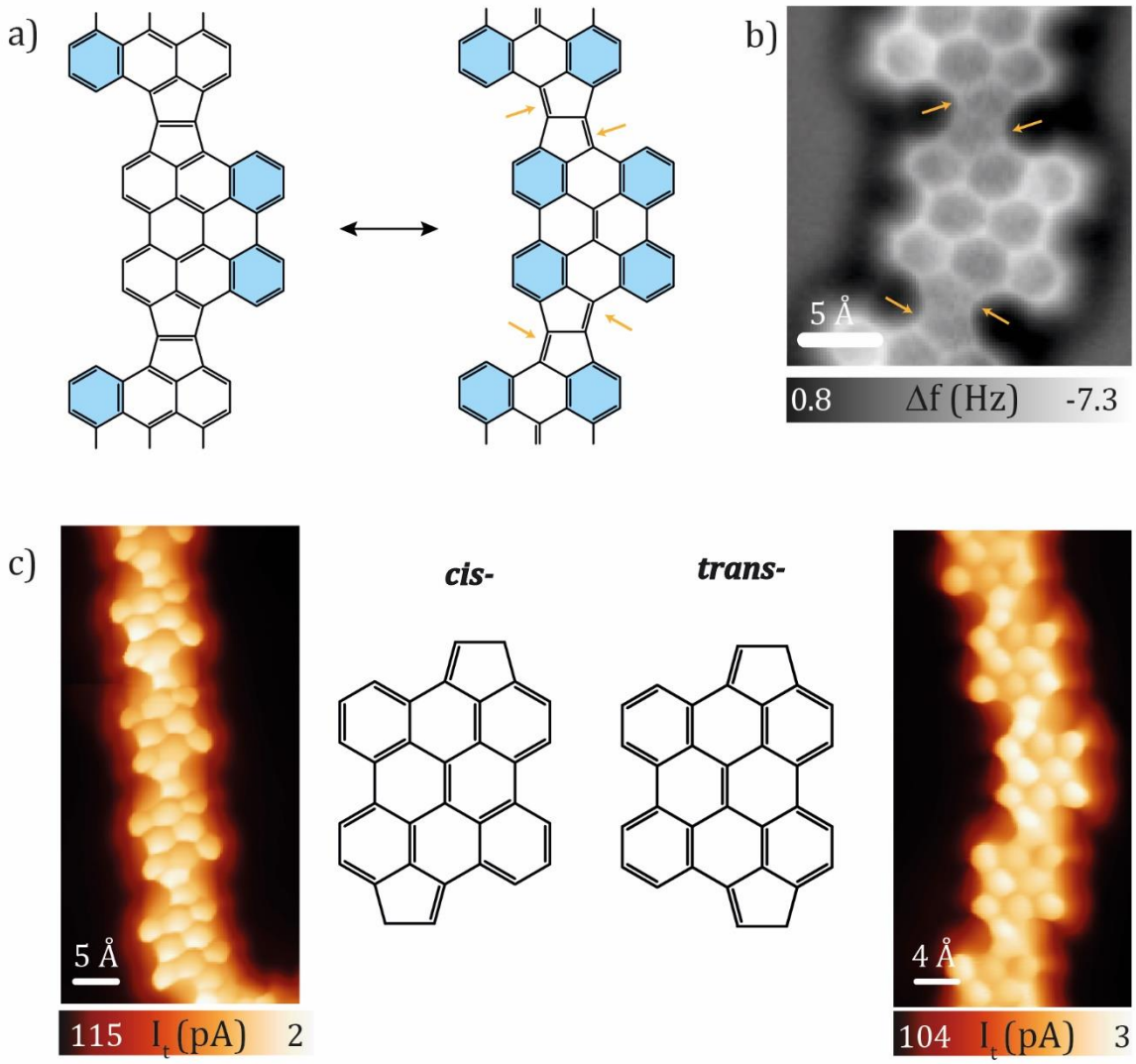

Figure 5-35. Resonance structures and isomers of pentalene-bridged bisanthene polymer

a) *Resonance structures of pentalene-bridged bisanthene polymer. Blue filled rings correspond to 6 π-electrons group.* ***b)*** *nc-AFM image of a section of the pentalene-bridged bisanthene polymer where shorter bonds in the pentalene bridge are observed (highlighted with yellow arrows) (V_b = 10 mV).* ***c)*** *Chemical sketch of the two different connection observed and their corresponding CO-tip constant-height STM image (both images: V_b = 20 mV).*

The two main competing resonance forms are shown in Figure 5.35a. To study the local aromaticity of the system, formed by benzenoid and non-benzenoid rings, we applied the Glidewell-Lloyd rule.[236,237] This rule is an extension of the Clar´s rules to non-benzenoid polycyclic conjugated hydrocarbons and affirms that these systems tend to form the smallest 4n+2 groups and avoid the formation of antiaromatic rings (4n), where n is zero or any positive integer number. The resonance form depicted in the chemical sketch shown at the left in Figure 5.35a contains two migrating Clar sextets in the bisanthene backbone. In contrast, the resonance form depicted in the chemical sketch shown at the right of Figure 5.35a depicts four Clar sextets at the bisanthene backbone. Following the Glidewell-Lloys rule the most stable resonance form is the one at the right of Figure 5.35a. Furthermore, high-resolution nc-AFM images allow to resolve the chemical structure and discriminate the bond order.[45,238] The dominant resonance form for this ladder polymer was investigated by means of nc-AFM. Figure 5.35b shows shorter bond lengths at the inner bond of the pentalene in comparison with the outer bond (shorter bonds highlighted with yellow arrows). The variation of the bond length observed in the nc-AFM image matches well with the most favorable resonance form predicted by the Glidewell-Lloyd rule. Thus, we can conclude the validity of such rule for this system that defines the second resonance form at the right as the predominant one.

Next, we have focused on the study of the two possible connections observed in the pentalene-bridged bisanthene polymer. The connection can feature *cis*- or *trans*-configurations, in which the bisanthene backbones are on or off the vertical axis of symmetry with respect to each other. Figure 5.35c shows both chemical sketches of the connections together with their corresponding constant height STM image with molecular resolution. Both connections are equally favourable and the maximum number of units with a repeating *cis*- or *trans*- connections was found to be 12.

These conjugated ladder polymers are of great interest due to their tendency towards the electron delocalization thanks to the restriction of free torsional motion in between the fused monomers.[229] Therefore, we have investigated their electronic properties *via* differential conductance dI/dV measurements. Figure 5.36a shows dI/dV spectra acquired on top of the external boundary of the bisanthene unit (purple curve) and on

top of the Au(111) surface as reference (orange curve). We distinguish two frontier resonances at -0.55 eV and +0.55 eV, which are assigned to the valence (VB) and conductance band (CB), respectively, giving rise to an experimental band gap of 1.1 eV.

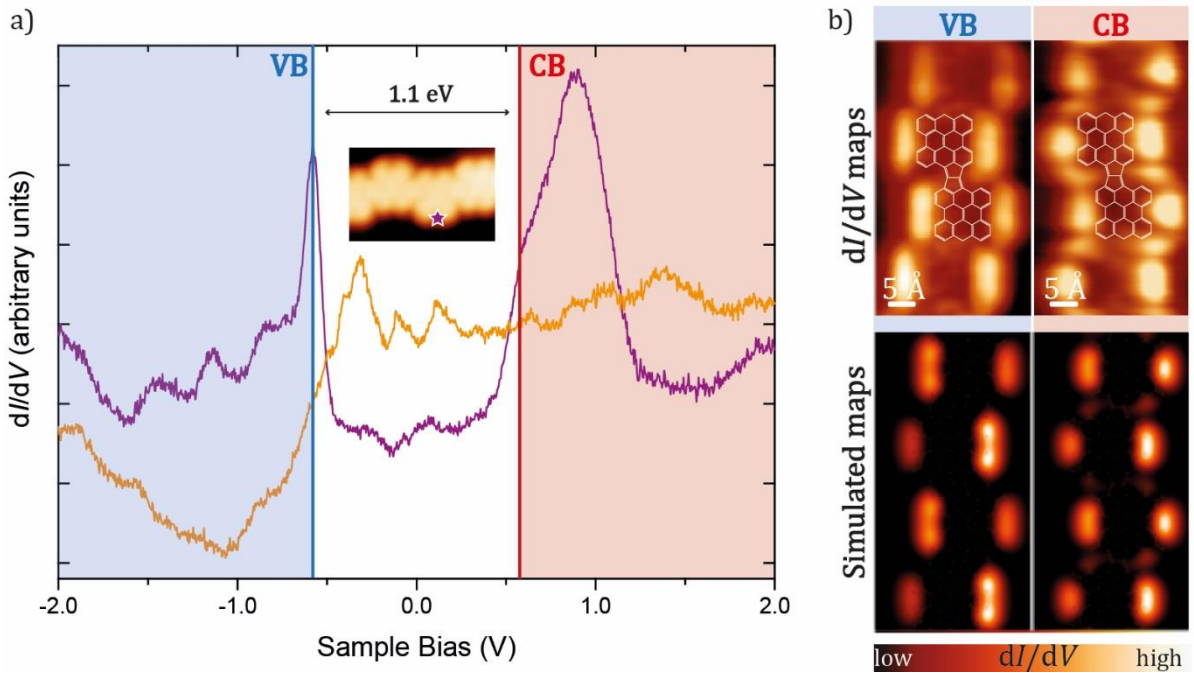

Figure 5-36. Experimental and theoretical results of the electronic structure of pentalene-bridged bisanthene polymer

a) *STS measurements revealing the experimental value of the band gap. The dI/dV curves were acquired at the positions depicted in the inset STM image.* ***b)*** *Upper panel corresponds to constant-current dI/dV maps acquired at the energies of the VB and CB (V_b = -550 mV and V_b = 550 mV, respectively). Bottom panel show the simulated dI/dV maps of the freestanding pentalene-bridged bisanthene polymer.*

Next, we acquired the dI/dV maps at the energies where the strong resonances in the STS were observed (see upper panel of Figure 5.36b). The dI/dV map at the VB shows maxima LDOS over the rims of the bisanthene units, as well as the dI/dV map of the CB, which in addition exhibits states over the armchair region of the bisanthene motifs and at the boundaries of the pentalene bridge. We have compared the experimental maps with calculated dI/dV maps for a freestanding pentalene-bridged bisanthene polymer, finding an excellent agreement between them (Figure 5.36b) and corroborating the rationalization of the electronic structure. No differences between the electronic properties of the *cis*- and *trans*- connection were found in the experimental measurements.

In conclusion, we have demonstrated that the cumulene-like bridged polymers after thermal annealing tend to react forming fused pentalene-bridged polymers. In such a way, we have introduced a new on-surface strategy for designing non-benzenoid based nanomaterials with low electronic band gaps.

5.8 Conclusions

We have developed a new on-surface strategy towards the design of π-conjugated polymers based on the functionalization of the molecular precursor with $=CBr_2$ functional groups, deposition on surfaces and subsequent thermal annealing.

Here, we have focused on the acene and periacene families, where we have observed how the most favorable resonance form of the polymer is modified depending on the repeating unit of the polymer. Furthermore, this change in the topology of the π-electrons of the molecular backbone and in the chemical nature of the bridge allows to tune the value of the electronic band gap of the polymer and defines its topological quantum class.

The experiments performed in this chapter are summarized in Figure 5.37, where we observe an abrupt decrease in the band gap of the polymer with the increasing size of the repeating units (1.5 eV for the anthracene polymer and 0.35 eV for the pentacene polymer). This decrease remains till the transition phase from trivial insulator to non-trivial (n=5 for acenes and n=3 for periacenes in black and red, respectively) is reached. After crossing the transition point, the electronic band gap starts to increase smoothly again (0.3 eV for the bisanthene polymer and 0.8 eV for the peripentacene polymer).

We have demonstrated that the topological transition is intimately related to a change in the size of the units and the π-electron network and, thus, there is a fundamental relationship between the resonance forms in π-conjugated polymers and their topological quantum phase.

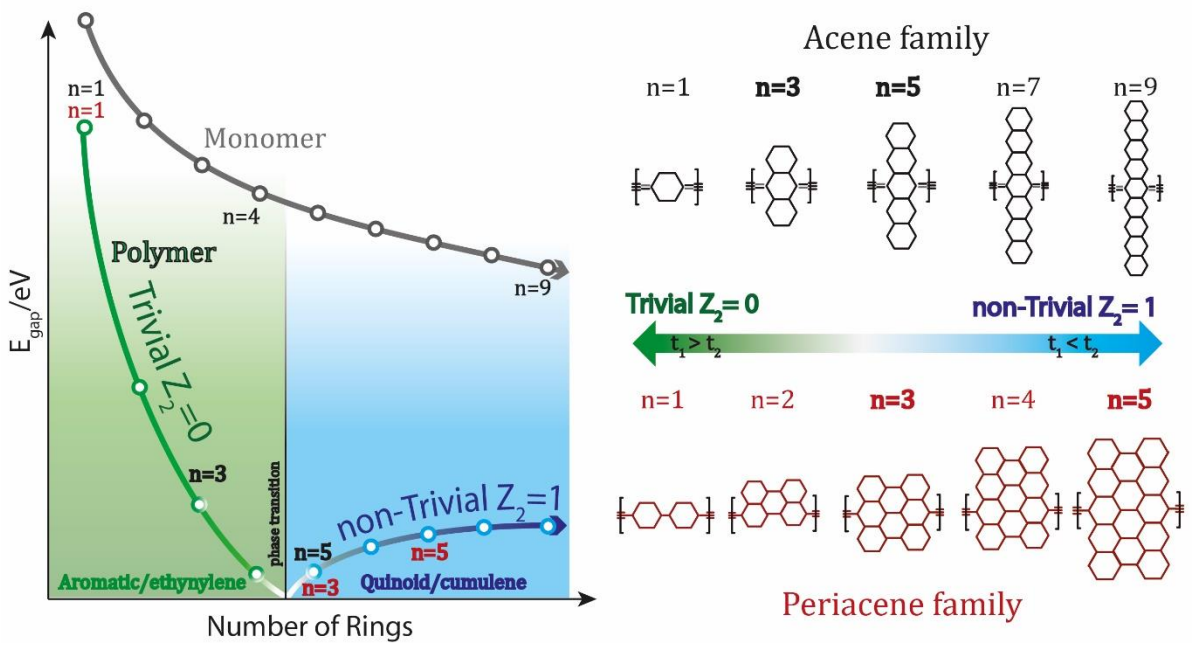

Figure 5-37. Topological quantum phase transition in the acene and periacene polymer family

Schematic evolution of the band gap of acene (black labels) and periacene (red labels) monomers and polymers with increasing size of the units. The transition phase and reorganization of π-conjugation is summarized in the scheme at the left. The right panel summarized the topological quantum phase predicted by tight binding for the ethynylene-bridged acene and periacene polymers.

Finally, further annealing of the cumulene-bridged polymers leads to their ladderization *via* double dehydrogenation and cyclization. Following this protocol, from cumulene-linked bisanthene polymers we have grown long and defect-free pentalene-bridged bisanthene polymers, which belong to the family of the ladder polymers where the bisanthene units are connected with each other through non-benzenoid fused rings. Notably, vibrational modes of the initial cumulene-linked biasanthene polymer play a crucial role in the reaction as compared to the ethynylene-bridged anthracene polymer case. These polymers show special interest due to the restriction of free torsional motion in between the fused monomers and their unique electronic properties caused by the presence of non-benzenoid rings.

6. General conclusions and perspectives

The work presented in this thesis shows the study of different nanomaterials at the atomic scale by means of state-of-the-art surface science techniques. Specifically, the characterization of the prepared nanomaterials has been achieved *via* low temperature STM and nc-AFM, supported by LEED and XPS measurements and complemented by TB, DFT and GW calculations. All the nanomaterials were prepared on a pristine Au(111) surface. This thesis reports the on-surface design of two different types of nanomaterials: i) inorganic compounds based on cobalt oxides and ii) organic compounds based on linear π-conjugated polymers. We have focused on such materials, since both of them are relevant to achieve global sustainability by the production of solar fuels or mitigation of the increasing demand of energy in our modern societies.

<u>CoO model catalyst for water splitting</u>

First, we have successfully grown single bilayer cobalt oxide nanoislands on Au(111) by cobalt evaporation in an oxygen environment and under UHV conditions. We have demonstrated a strong dependence in the electronic structure of the CoO nanoislands with the registry of the Au(111) substrate *via* STS. Two different regions have been found:

- The **Moiré pattern region** corresponds to an incommensurate region of the CoO ($d_{O\text{-}O}$ = 3.3 Å) with the substrate where two different sub-regions are identified: the **moiré region A** and the **moiré region B**. We have investigated the nature of this moiré pattern by means of force spectroscopy, finding a vertical spatial corrugation of 30 pm. In addition, this corrugation implies an electronic modulation with larger unoccupied LDOS in the area B in contrast to the larger occupied LDOS of the area A. We tentatively assigned this effect to a modulated electron transfer between the Au(111) substrate and the CoO nanoislands.

- The **βeta-region** corresponds to a compressed area of the moiré region, where the averaged interatomic distance is $d_{O\text{-}O}$ = 3.0 Å. The electronic structure of this area is totally different with respect to the moiré region, exhibiting the largest unoccupied LDOS. Remarkably, this region presents different reactivity with respect to the moiré region, showing clear affinity for adsorbates, i.e. small molecules coming from the residual gas present in the UHV chamber, tentatively assigned to H_2O molecules, which are found attached only at this region.

Interestingly, we can induce the transition from the moiré region into the βeta-region by tip manipulation. After inducing this transition, the atoms are compressed presenting shorter interatomic distances. Remarkably, this transition is irreversible and we are not able to induce the transformation from βeta-region into moiré region.

Finally, we have investigated the performance of this anode model for catalyzing the water splitting reaction. For that purpose, we have exposed the sample containing a submonolayer coverage of CoO to 100 Langmuir of water at RT under UHV conditions. After water exposure, STM images show hydroxyl groups mainly attached to the moiré region A of the CoO nanoislands, where, apparently, the interaction with the Au(111) substrate is stronger and the occupied LDOS are larger. This effect suggests the synergy effect between the CoO and gold substrate towards a higher catalytic activity of the water splitting reaction. In addition, we have demonstrated the tunability of the CoO reactivity as function of the lattice parameter by external stimuli such as electric field.

Co-based oxides are promising catalysts for the water splitting reaction due to the multivalent oxidation states of cobalt. Our next goal will be the investigation of the synergy effect between binary or even ternary oxides based on transition metal oxides, paying special attention to the cobalt, iron and nickel elements. Oxides based on cobalt, nickel and/or iron are promising candidates to be integrated as anode in a photoelectrochemical cell, which contributes to the development of clean energies.

All these experiments have been performed in the framework of the FET Proactive Artificial Leaf project, which is focused on the design of a photoelectrochemical device

for the capture and transformation of solar energy into chemical energy, as a clean alternative to fossil resources.

π-conjugated polymers based on acene and periacenes

Next, we have developed a new on-surface synthetic route towards the design and fabrication of π-conjugated polymers based on the functionalization of acene and periacene units with the $=CBr_2$ functional groups at strategic positions. In such a way, we have been able to synthesize low band gap linearly linked acene and periacene π-conjugated polymers on the Au(111) surface. We have explored the properties of such polymers and their tunability by varying the size of the central unit.

In addition, we have proven the topological band theory predictions related to the topological phase transition of the acene and periacene polymers from trivial to non-trivial *via* closure of the band gap and electronic rearrangement. This topological transition can be tentatively understood with the SSH model. We have assigned two different hopping parameters, t_1 and t_2, to the two sublattices that form the unit cell. The relation between this hopping parameters will define the topological nature of the polymer, where $t_1 > t_2$ corresponds to a trivial insulator, $t_1 = t_2$ to a metallic polymer and $t_1 < t_2$ to a non-trivial insulator. The values of t_1 and t_2 depend on the central acene or periacene and on the nature of the linker connecting these units. Therefore, the strategical design of the precursor, the investigation of the electronic properties and the inspection of the chemical structure of the formed polymers are crucial in order to rationalize the topological predictions.

From the family of acenes, we have synthesized **ethynylene-bridged anthracene** polymers which present an electronic band gap of 1.4 eV. The experimental dI/dV spectra recorded at the polymer ends reveal the absence of end states and, hence, the trivial insulator nature of such polymer. Then, we have synthesized **cumulene-like bridged pentacene** polymers, in order to decrease the band gap of the polymer, by including a larger acene unit which contributes to the π-electron delocalization along the polymer backbone. This polymer shows a narrow experimental band gap of 0.35 eV and a theoretical band gap of 0.05 eV. Interestingly, we observe the emergence of a delocalized

state along 7-8 units at the polymer ends, which corroborates its non-trivial insulator nature, as indicated by DFT and predicted by TB calculations for the family of acene polymers.

Finally, in order to illustrate the scope of our approach, we have characterized the structural and electronic properties of bisanthene and peripentacene polymers, belonging to the periacene family. First, the **cumulene-like bridged bisanthene** polymer shows an experimental band gap of 0.3 eV (theoretical of 0.05 eV), even narrower than the pentacene polymer. We observe the emergence of an end state at the polymer ends which is delocalized along 4-5 units. We classified this polymer into the non-trivial insulator quantum phase. Theoretical calculations predict that the bisanthene polymer is a topological insulator located close to the transition phase from trivial to non-trivial. Then, moving a step further to the peripentacene polymer, the predictions confirm that such polymer also belongs to the non-trivial insulator quantum phase, though its band gap is expected to be larger and the end state located only at the edges. Therefore, we have synthesized the **cumulene-bridged peripentacene** polymer which exhibits an experimental band gap of 0.8 eV. STS measurements at the polymer ends confirm the emergence of a zero-bias resonance for polymers longer than dimers, which is due to the singly occupation of the end state, which is distributed at the zigzag edges. Interestingly, we have observed a magnetic transition from antiferromagnetic state in peripentacene dimers to paramagnetic for trimers and longer oligomers.

Importantly, a further thermal annealing of the cumulene-bridged bisanthene polymer leads to the formation of long **pentalene-bridged bisanthene polymers**. The viability of such reaction has been rationalized due to the characteristic vibrational bending modes of the cumulene bridge. The ladderization of the polymer can take place *via cis*- or *trans*- configuration. This ladder polymer includes non-benzenoid rings which open new avenues towards tuning the chemical and electronic properties. Our results anticipate the importance of vibrational modes for the understanding of the reaction mechanisms.

In general, we have been able to synthesize and characterize acene and periacene polymers observing the competition between ethynylene/aromatic and cumulene/quinoid forms, which will be crucial for the understanding of the electronic

properties of such polymers. In addition, we have made a direct connection between the chemical resonance forms and the topological predictions, demonstrating that the increase of the acene or periacene size makes the intercell coupling (t_2) overcomes the intra-cell coupling (t_1) and an electronic rearrangement of the bridge from ethynylene to cumulene, resulting in the topological phase transition and a reopening of the band gap.

These results shed light into the design of new polymers with tunable properties and promising applications in organic electronics. On one hand, the synthetic route opens new opportunities for on-surface synthesis, which can be extended towards the formation of 2D materials from the appropriate design of molecular precursors. On the other hand, we have demonstrated that the electronic and magnetic properties of acene and periacene polymers can be tuned, opening new strategies towards the synthesis of metallic polymers or the design of multiradical polymers.

To summarize, cobalt-based oxides are valuable materials with unique applications in catalysis. Furthermore, carbon-based materials show remarkable mechanical, electrical, magnetic and thermal properties and play a critical role in low-energy consumption modern electronics and optoelectronics. Both cobalt oxides and π-conjugated polymers are crucial in the development of clean energies.

7. Conclusiones generales y perspectivas

El trabajo presentado en esta tesis muestra el estudio a escala atómica de diferentes nanomateriales mediante técnicas de caracterización de superficies. Las principales técnicas empleadas han sido la microscopía efecto túnel (STM) y la microscopía de fuerza atómica en modo no contacto (nc-AFM) a baja temperatura y, además, dicho estudio se ha complementado con otras técnicas como difracción de electrones de baja energía (LEED) y espectroscopía de fotoemisión de rayos X (XPS) o cálculos de la teoría del funcional de la densidad (DFT) y del método de ligaduras fuertes (TB). Todos los nanomateriales se prepararon sobre un sustrato limpio de Au(111). Esta tesis muestra el diseño en superficies metálicas de dos tipos de nanomateriales: compuestos inorgánicos basados en óxidos de cobalto y compuestos orgánicos basados en polímeros lineales π-conjugados. Nos hemos centrado en estos materiales ya que ambos podrían contribuir a satisfacer la creciente demanda energética actual o a un mundo más sostenible buscando fuentes energéticas alternativas.

<u>CoO como modelo de catalizador para la división del agua</u>

En primer lugar, hemos crecido exitosamente nanoislas de óxido de cobalto formadas por una única doble capa de cobalto y oxígeno en Au(111) mediante la evaporación de cobalto en ambiente de oxígeno. Hemos demostrado una fuerte dependencia en la estructura electrónica del CoO con el registro del sustrato Au(111) a través de la espectroscopía de efecto túnel. Dos regiones diferentes han sido identificadas:

- La **región del patrón de Moiré** corresponde a una región inconmensurada del CoO ($d_{O\text{-}O}$ = 3.3 Å) con el sustrato donde se identifican dos subáreas diferentes: la **región del moiré A** y la **región del moiré B**. Hemos investigado la naturaleza de este patrón de moiré por medio de espectroscopía de fuerza, confirmando la presencia de una corrugación real de 30 pm. Además, esta corrugación implica una modulación electrónica que conlleva mayor densidad de estados desocupados en la zona de moiré B, mientras que la zona de moiré A posee mayor densidad de

estados ocupados. Tentativamente asignamos este efecto a una transferencia modulada de electrones entre el sustrato Au(111) y el CoO.

- La región βeta corresponde a una zona de compresión atómica de la región del moiré, donde la distancia interatómica promedio es $d_{O\text{-}O}$ = 3.0 Å. La estructura electrónica en este área es totalmente diferente con respecto a la región de moiré, exhibiendo mucha mayor densidad de estados desocupados. Sorprendentemente, esta región presenta diferente reactividad con respecto a la región de moiré, mostrando una clara afinidad por los adsorbatos provenientes de moléculas presentes en la campana de ultra alto vacío. Tentativamente asignamos estos adsorbatos a moléculas de agua que se encuentran únicamente adheridas a la región βeta.

Curiosamente, podemos modificar la región de moiré convirtiéndola en región βeta mediante manipulación con la punta. Después de inducir esta transición, los átomos se comprimen presentando distancias interatómicas más cortas. Sorprendentemente, esta transición es irreversible, de manera que no somos capaces de inducir la transformación de la región βeta de vuelta a la región moiré.

Finalmente, hemos investigado el funcionamiento del CoO como modelo de ánodo para la catálisis de la reacción de división del agua. Para ello, hemos expuesto la muestra a 100 Langmuir de agua a temperatura ambiente y en condiciones de ultra alto vacío. A continuación, observamos la aparición de grupos hidroxilo unidos al CoO que presentan mayor afinidad por la región del moiré A donde, aparentemente, la interacción con el sustrato Au(111) es más fuerte y la densidad de estados ocupados mayor. Este hecho sugiere un efecto sinérgico entre el CoO y el oro hacia una mayor actividad catalítica de la reacción de división del agua. Además, hemos demostrado la capacidad de modificar la reactividad del CoO en función del parámetro de red tras aplicar un estímulo externo como es el campo eléctrico.

Los óxidos de Co son prometedores catalizadores de la reacción de división del agua debido a los estados de oxidación multivalentes del cobalto. Nuestro próximo objetivo será la inspección del efecto sinérgico entre óxidos binarios o incluso ternarios basados

en óxidos de metales de transición, centrándonos especialmente en el cobalto, hierro y níquel. Los óxidos a base de cobalto, níquel y / o hierro son prometedores candidatos para ser integrados como ánodo en una celda fotoelectroquímica, contribuyendo al desarrollo de energías limpias.

Todos estos experimentos se han llevado a cabo en el marco del Proyecto Europeo "Artificial Leaf", en el cual diferentes grupos de investigación trabajan hacia un objetivo común que es diseñar una celda fotoelectrocatalítica para poder capturar y transformar energía solar en energía química, siendo una prometedora alternativa a las fuentes de combustible.

Polímeros π-conjugados formados por unidades de acenos y periacenos

Por otro lado, hemos desarrollado una nueva ruta sintética en superficies para diseñar polímeros π-conjugados basándonos en la funcionalización de unidades de aceno y periaceno con el grupo funcional $=CBr_2$ en posiciones estratégicas para sintetizar polímeros lineales. Hemos sintetizado polímeros lineales π-conjugados de poliacenos con un bajo intervalo de banda prohibida. Hemos explorado las propiedades de estos polímeros y cómo se pueden modificar variando el tamaño de la unidad central que los forma.

Además, hemos demostrado experimentalmente las predicciones de la teoría de bandas topológicas para los polímeros de acenos y periacenos, en los cuales se espera observar una transición de aislante trivial a aislante no trivial a través del cierre de la banda de energía prohibida que conlleva un reorganizado electrónico. Esta transición topológica puede ser interpretada a través del modelo SSH. Para ello, debemos asignar dos parámetros de acople, t_1 y t_2, a las dos subredes que forman la celda unidad del polímero. La relación entre estos dos parámetros de acople definirá la naturaleza topológica del polímero, de manera que la relación $t_1 > t_2$ corresponde a un aislante trivial, $t_1 = t_2$ a un polímero metálico y $t_1 < t_2$ a un aislante no trivial. Los valores que se asignan a los parámetros de acople dependen directamente del aceno o periaceno que forma dicho polímero y de la naturaleza del puente que los une. Por ello, un diseño estratégico del precursor empleado para formar los polímeros, junto al estudio de la estructura

electrónica y de la naturaleza química de los polímeros formados nos permite racionalizar las predicciones de la teoría topológica de bandas.

De la familia de los acenos hemos sintetizado **polímeros de antracenos unidos a través de puentes etinileno** con un intervalo de banda prohibida de 1.4 eV. Los espectros dI/dV tomados en los extremos de los polímeros junto con cálculos teóricos revelan la ausencia de estados finales y, por lo tanto, la naturaleza aislante trivial de dicho polímero. A continuación, hemos sintetizado **polímeros de pentacenos unidos a través de puente de carácter cumulénico** con el objetivo de disminuir el intervalo de banda prohibida del polímero al incluir una unidad central más grande que contribuye a la deslocalización de electrones π a lo largo del polímero. Este polímero muestra un estrecho intervalo de banda prohibida de 0.35 eV (frente al obtenido teóricamente de 0.05 eV). Curiosamente, en los extremos del polímero observamos la aparición de un estado deslocalizado a lo largo de 7-8 unidades, lo que sugiere su naturaleza aislante no trivial. Además, estos resultados son corroborados con los cálculos DFT y TB.

Finalmente, hemos estudiado los polímeros de bisanteno y peripentaceno, los cuales pertenecen a la familia de los periacenos. En primer lugar, el **polímero de bisantenos unidos a través de puentes de carácter cumulénico** muestra un intervalo de banda prohibida experimental de 0.3 eV (y teórico de 0.05 eV), el cual es incluso más estrecho que el medido para el polímero de pentaceno. Observamos la aparición de un estado final en las terminaciones del polímero que se deslocaliza a lo largo de 4-5 unidades, por lo que asignamos este polímero a la familia de los aislantes no triviales. Los cálculos teóricos predijeron que el polímero de bisanteno es un aislante topológico ubicado cerca del punto de transición de trivial a no trivial. Además, si avanzamos un paso más en la familia de los polímeros de periacenos hacia el polímero de peripentaceno, las predicciones confirman que dicho polímero también pertenece a la familia de aislantes no trivial. Sin embargo, se espera que su intervalo de banda prohibida sea mayor y el estado final se encuentre más localizado y ubicado únicamente en los bordes. Hemos sintetizado el **polímero de peripentacenos unidos a través de puentes cumulénicos** que exhibe un intervalo de banda prohibida de 0.8 eV. Las medidas de espectroscopía tomadas al final del polímero confirman la aparición de un estado final ubicado en el borde en zigzag que

confirma el carácter radical de dicho polímero. La estructura de capa abierta del monómero de peripentaceno juega un papel importante en el carácter radical del polímero y su puente cumuleno. Es importante destacar que observamos una transición magnética de dímero de peripentaceno a trímero (o más largos), pasando de ser antiferromagnéticos a paramagnéticos, respectivamente.

Es importante destacar que un calentamiento adicional a 600 K del polímero de bisanteno con puentes de cumuleno conduce a la formación de **polímeros de bisantenos unidos a través de puentes de pentalenos** libres de defectos. Dicha reacción se produce selectivamente debido a los modos de vibración específicos del puente cumulénico. La laderización del polímero puede tener lugar mediante unión por configuración *cis* o *trans*. Este polímero incluye anillos no bencenoides que abren nuevas vías para controlar las propiedades químicas y electrónicas de dichos polímeros. Nuestros resultados demuestran la importancia del estudio de los modos de vibración para el estudio de los mecanismos de reacción.

Hemos sintetizado y caracterizado polímeros de aceno y periaceno observando la competición entre las formas resonantes de etinileno/aromático y cumuleno/quinoide, las cuales serán cruciales para la comprensión de las propiedades electrónicas de dichos polímeros. Además, hemos hecho una conexión directa entre las formas químicas resonantes y las predicciones topológicas, demostrando que al incrementar el tamaño del aceno o periaceno el parámetro de acople intercelda (t_2) sobrepasa al parámetro de acople intracelda (t_1), lo que conlleva una reorganización electrónica del puente etinileno a cumuleno, una transición topológica y la abertura de nuevo de la banda prohibida.

Estos resultados contribuyen al diseño de nuevos polímeros con propiedades ajustables para su uso en electrónica orgánica. Por un lado, la ruta sintética abre nuevas oportunidades en la síntesis en superficie incluso para el diseño de materiales 2D. Por otro lado, hemos demostrado cómo ajustar las propiedades electrónicas y magnéticas, abriendo nuevas estrategias hacia la síntesis de polímeros metálicos o el diseño de polímeros multi-radicales.

En resumen, los óxidos a base de cobalto son valiosos materiales con aplicaciones únicas en catálisis. Además, los materiales a base de carbono muestran remarcables propiedades mecánicas, eléctricas, magnéticas y térmicas y desempeñan un papel fundamental en la electrónica moderna y la optoelectrónica de bajo consumo de energía. Finalmente, cabe destacar que tanto los óxidos de cobalto como los materiales basados en carbono son cruciales para el desarrollo de energías limpias.

8. List of Publications

- **Sánchez-Grande, A.**; De la Torre, B.; Santos, J.; Cirera, B.; Lauwaet, K.; Chutora, T.; Edalatmanesh, S.; Mutombo, P.; Rosen, J.; Zbořil, R.; Miranda, R.; Björk, J.; Jelínek, P.; Martín, N. and Écija, D. **On-Surface Synthesis of Ethynylene-Bridged Anthracene Polymers**. Angewandte Chemie International Edition. 58 (20), 6559-6563 (2019).

- Cirera, B.;* **Sánchez-Grande, A.**;* De la Torre, B.;* Santos, J.; Edalatmanesh, S.; Rodríguez-Sánchez E.; Lauwaet, K.; Mallada, B.; Zbořil, R.; Miranda, R.; Gröning, O.; Jelínek, P.; Martín, N. and Écija, D. **Tailoring topological order and π-conjugation to engineer quasi-metallic polymers.** Nature Nanotechnology 15, 437–443 (2020). (*equally contributing authors)

- **Sánchez-Grande, A.**; Urgel, J. I.; Cahlík, A.; Santos, J.; Edalatmanesh, S.; Rodríguez-Sánchez E.; Lauwaet, K.; Chutora, T.; Mutombo, P.; Nachtigallová, D.; Nieman, R.; Lischka, Hans.; De la Torre, B.; Miranda, R.; Gröning, O.; Jelínek, P.; Martín, N. and Écija, D. **Diradical organic one-dimensional polymers synthesized on a metallic surface.** Angewandte Chemie International Edition (2020).

- De la Torre, B.;* Matěj, A.;* **Sánchez-Grande, A.**;* Cirera, B.; Mallada, B.; Rodríguez-Sánchez E.; Santos, J.; Mendieta-Moreno, J. I.; Edalatmanesh, S.; Lauwaet, K.; Otyepka, M.; Medved, M.; Buendía, A., Miranda, R.; Martín, N.; Jelínek, P. and Écija, D. **Tailoring π-conjugation and vibrational modes to steer on-surface synthesis of pentalene-bridged ladder polymers.** Nature Communications. (*equally contributing authors)

- **Sánchez-Grande, A.**; Urgel, J. I.; Edalatmanesh, S.; Veis, L.; Santos, L.; Lauwaet, K.; Gallego, J.M.; Brabec, J.; Beran, P.; Nachtigallová, D.; Miranda, R.; Martín, N.; Jelínek, P. and Écija, D. **Unravelling the open-shell character of peripentacene on Au(111).** Journal of the Physical Chemistry Letters. (In peer review)

- **Sánchez-Grande, A**.; Nguyën, H.C.; Lauwaet, K.; Rodríguez-Fernández, J.; Carrasco, E.; Zhao-Zong, S.; Urgel, J. I.; Cirera, B.; Gallego, J.M.; Miranda, R.; Lauritsen, J.V.; López, N.; Écija, D. **Electrically Tunable Substrate-supported Cobalt Oxide Nanocrystals.** (In progress)

- Biswas, K.; Urgel, J. I.; **Sánchez-Grande, A**.; Edalatmanesh, S.; Santos, J.; Cirera, B.; Mutombo, P.; Lauwaet, K.; Rodríguez-Sánchez E.; Miranda, R.; Martín, N.; Jelínek, P. and Écija, D. **On-surface synthesis of doubly-linked one-dimensional pentacene ladder polymers.** (In progress)

9. Bibliography

1. Feynman, R. P. There's Plenty of Room at the Bottom. *Eng. Sci.* **23**, 22–36 (1960).
2. Oxley, M. P., Lupini, A. R. & Pennycook, S. J. Ultra-high resolution electron microscopy. *Rep. Prog. Phys.* **80**, 026101 (2017).
3. Eigler, D. M. & Schweizer, E. K. Positioning single atoms with a scanning tunnelling microscope. *Nature* **344**, 524–526 (1990).
4. Balzani, V. Nanoscience and nanotechnology: The bottom-up construction of molecular devices and machines. *Pure Appl. Chem.* **80**, 1631–1650 (2008).
5. Cao, G. *Nanostructures And Nanomaterials: Synthesis, Properties And Applications*. (World Scientific, 2004).
6. Binnig, G., Rohrer, H., Gerber, Ch. & Weibel, E. Surface Studies by Scanning Tunneling Microscopy. *Phys. Rev. Lett.* **49**, 57–61 (1982).
7. Binnig, G., Quate, C. F. & Gerber, Ch. Atomic Force Microscope. *Phys. Rev. Lett.* **56**, 930–933 (1986).
8. Wiesendanger, R. Contributions of scanning probe microscopy and spectroscopy to the investigation and fabrication of nanometer-scale structures. *J. Vac. Sci. Technol. B Microelectron. Nanometer Struct. Process. Meas. Phenom.* **12**, 515–529 (1994).
9. Nourbakhsh, A. *et al.* MoS2 Field-Effect Transistor with Sub-10 nm Channel Length. *Nano Lett.* **16**, 7798–7806 (2016).
10. Wolinsky, J. B., Colson, Y. L. & Grinstaff, M. W. Local drug delivery strategies for cancer treatment: Gels, nanoparticles, polymeric films, rods, and wafers. *J. Controlled Release* **159**, 14–26 (2012).
11. Mazumder, V., Lee, Y. & Sun, S. Recent Development of Active Nanoparticle Catalysts for Fuel Cell Reactions. *Adv. Funct. Mater.* **20**, 1224–1231 (2010).
12. When size matters: Nanotechnology for energy efficiency. *ScienceDaily* https://www.sciencedaily.com/releases/2011/06/110615080217.htm.
13. Mizushima, K., Jones, P., Wiseman, P. & Goodenough, J. LixCoO2 (0<x⩽1): A new cathode material for batteries of high energy density. *Solid State Ion.* **3–4**, 171–174 (1981).

14. Tkaczyk, A. H., Bartl, A., Amato, A., Lapkovskis, V. & Petranikova, M. Sustainability evaluation of essential critical raw materials: cobalt, niobium, tungsten and rare earth elements. *J. Phys. Appl. Phys.* **51**, 203001 (2018).
15. Institute, C. Human Health Science. https://www.cobaltinstitute.org/human-health.html (2020).
16. Towards an artificial leaf. *A-Leaf Project.* http://www.a-leaf.eu/.
17. *Organic Electronic Materials: Conjugated Polymers and Low Molecular Weight Organic Solids*. (Springer-Verlag, 2001).
18. Avouris, P., Chen, Z. & Perebeinos, V. Carbon-based electronics. in *Nanoscience and Technology* 174–184 (2009).
19. Heeger, A. J. Semiconducting and Metallic Polymers: The Fourth Generation of Polymeric Materials (Nobel Lecture). *Angew. Chem. Int. Ed Engl.* **40**, 2591–2611 (2001).
20. Cirera, B. *et al.* Tailoring topological order and π- conjugation to engineer quasi-metallic polymers. *Nat. Nanotechnol.* **15**, 437–443 (2020).
21. Wiesendanger, R. & Roland, W. *Scanning Probe Microscopy and Spectroscopy: Methods and Applications*. (Cambridge University Press, 1994).
22. Wiesendanger, R. *Scanning Probe Microscopy: Analytical Methods*. (Springer Science & Business Media, 2013).
23. Morita, S., Wiesendanger, R. & Meyer, E. *Noncontact Atomic Force Microscopy*. (Springer-Verlag, 2002).
24. Kittel, C. *Introduction to Solid State Physics*. (Wiley, 2004).
25. Ibach, H. & Lüth, H. *Solid-State Physics: An Introduction to Principles of Materials Science*. (Springer-Verlag, 2009).
26. Moore, J. E. The birth of topological insulators. *Nature* **464**, 194–198 (2010).
27. Kane, C. L. & Mele, E. J. Z2 Topological Order and the Quantum Spin Hall Effect. *Phys. Rev. Lett.* **95**, 146802 (2005).
28. Kosterlitz, J. M. Nobel Lecture: Topological defects and phase transitions. *Rev. Mod. Phys.* **89**, 040501 (2017).
29. Rizzo, D. J. *et al.* Topological band engineering of graphene nanoribbons. *Nature* **560**, 204–208 (2018).

30. Gröning, O. *et al.* Engineering of robust topological quantum phases in graphene nanoribbons. *Nature* **560**, 209–213 (2018).
31. Kou, L., Ma, Y., Sun, Z., Heine, T. & Chen, C. Two-Dimensional Topological Insulators: Progress and Prospects. *J. Phys. Chem. Lett.* **8**, 1905–1919 (2017).
32. Hsieh, D. *et al.* A topological Dirac insulator in a quantum spin Hall phase. *Nature* **452**, 970–974 (2008).
33. Harrison, W. A. *Electronic Structure and the Properties of Solids: The Physics of the Chemical Bond*. (Courier Corporation, 2012).
34. Asbóth, J. K., Oroszlány, L. & Pályi, A. *A Short Course on Topological Insulators: Band Structure and Edge States in One and Two Dimensions*. (Springer International Publishing, 2016).
35. Munoz, F., Pinilla, F., Mella, J. & Molina, M. I. Topological properties of a bipartite lattice of domain wall states. *Sci. Rep.* **8**, 17330 (2018).
36. Batra, N. & Sheet, G. Understanding Basic Concepts of Topological Insulators Through Su-Schrieffer-Heeger (SSH) Model. *ArXiv190608435 Cond-Mat* (2019).
37. Pendás, A. M. *et al.* A chemical theory of topological insulators. *Chem. Commun.* **55**, 12281–12287 (2019).
38. Shirakawa, H., Ito, T. & Ikeda, S. Electrical Properties of Polyacetylene with Various Cis-Trans Composites. *Makromol. Chem.* **179**, 1565–1573 (1978).
39. Wang, Y. & Mak, C. H. Transferable tight-bonding potential for hydrocarbons. *Chem. Phys. Lett.* **235**, 37–46 (1995).
40. Cao, T., Zhao, F. & Louie, S. G. Topological Phases in Graphene Nanoribbons: Junction States, Spin Centers, and Quantum Spin Chains. *Phys. Rev. Lett.* **119**, 076401 (2017).
41. Binnig, G., Rohrer, H., Gerber, Ch. & Weibel, E. 7 x 7 Reconstruction on Si(111) Resolved in Real Space. *Phys. Rev. Lett.* **50**, 120–123 (1983).
42. Bartels, L., Meyer, G. & Rieder, K.-H. Controlled vertical manipulation of single CO molecules with the scanning tunneling microscope: A route to chemical contrast. *Appl. Phys. Lett.* **71**, 213 (1998).
43. Binnig, G. & Rohrer, H. In touch with atoms. *Rev. Mod. Phys.* **71**, S324–S330 (1999).

44. Custance, O., Perez, R. & Morita, S. Atomic force microscopy as a tool for atom manipulation. *Nat. Nanotechnol.* **4**, 803–810 (2009).
45. Gross, L., Mohn, F., Moll, N., Liljeroth, P. & Meyer, G. The Chemical Structure of a Molecule Resolved by Atomic Force Microscopy. *Science* **325**, 1110–1114 (2009).
46. Chen, C. J. *Introduction to Scanning Tunneling Microscopy*. (Oxford University Press, 1993).
47. Tipler, P. & Mosca, G. *Physics for scientists and engineers*. vol. 3 (Macmillan, 2007).
48. Blokhintsev, D. I. *Quantum Mechanics*. (Springer Science & Business Media, 2012).
49. Bardeen, J. Tunnelling from a Many-Particle Point of View. *Phys. Rev. Lett.* **6**, 57–59 (1961).
50. Tersoff, J. & Hamann, D. R. Theory and Application for the Scanning Tunneling Microscope. *Phys. Rev. Lett.* **50**, 1998–2001 (1983).
51. Hamers, R. J. Atomic-Resolution Surface Spectroscopy with the Scanning Tunneling Microscope. *Annu. Rev. Phys. Chem.* **40**, 531–559 (1989).
52. Tersoff, J. & Hamann, D. R. Theory of the scanning tunneling microscope. *Phys. Rev. B* **31**, 805–813 (1985).
53. Li, B., Li, Z., Yang, J. & Hou, J. G. STM studies of single molecules: molecular orbital aspects. *Chem. Commun.* **47**, 2747 (2011).
54. Chen, Y.-C. *et al.* Tuning the Band Gap of Graphene Nanoribbons Synthesized from Molecular Precursors. *ACS Nano* **7**, 6123–6128 (2013).
55. Garnica, M. *et al.* Long-range magnetic order in a purely organic 2D layer adsorbed on epitaxial graphene. *Nat. Phys.* **9**, 368–374 (2013).
56. Jalili, N. & Laxminarayana, K. A review of atomic force microscopy imaging systems: application to molecular metrology and biological sciences. *Mechatronics* **14**, 907–945 (2004).
57. Gross, L. *et al.* Atomic Force Microscopy for Molecular Structure Elucidation. *Angew. Chem. Int. Ed.* **57**, 3888–3908 (2018).
58. Lee, M. & Jhe, W. General Theory of Amplitude-Modulation Atomic Force Microscopy. *Phys. Rev. Lett.* **97**, 036104 (2006).

59. Albrecht, T. R., Grütter, P., Horne, D. & Rugar, D. Frequency modulation detection using high-Q cantilevers for enhanced force microscope sensitivity. *J. Appl. Phys.* **69**, 668 (1998).
60. Giessibl, F. J. Atomic Resolution of the Silicon (111)-(7x7) Surface by Atomic Force Microscopy. *Science* **267**, 68–71 (1995).
61. Giessibl, F. J. Forces and frequency shifts in atomic-resolution dynamic-force microscopy. *Phys. Rev. B* **56**, 16010–16015 (1997).
62. Tsukada, M., Sasaki, N., Gauthier, M., Tagami, K. & Watanabe, S. *Theory of Non-Contact Atomic Force Microscopy*. (Springer, 2002).
63. Pérez, R., Štich, I., Payne, M. C. & Terakura, K. Surface-tip interactions in noncontact atomic-force microscopy on reactive surfaces: Si(111). *Phys. Rev. B* **58**, 10835–10849 (1998).
64. Guggisberg, M. *et al.* Separation of interactions by noncontact force microscopy. *Phys. Rev. B* **61**, 11151–11155 (2000).
65. Sugimoto, Y. *et al.* Chemical identification of individual surface atoms by atomic force microscopy. *Nature* **446**, 64–67 (2007).
66. Haugstad, G. *Atomic Force Microscopy: Understanding Basic Modes and Advanced Applications*. (John Wiley & Sons, 2012).
67. Cochrane, K. Single Molecule Perspective of Model Organic Semiconductors: Energy Level Mapping by High Resolution Scanning Probe Microscopy. (The University of British Columbia, 2017).
68. Lantz, M. A. *et al.* Quantitative Measurement of Short-Range Chemical Bonding Forces. *Science* **291**, 2580–2583 (2001).
69. Welker, J., Weymouth, A. J. & Giessibl, F. J. The Influence of Chemical Bonding Configuration on Atomic Identification by Force Spectroscopy. *ACS Nano* **7**, 7377–7382 (2013).
70. Kawai, S. *et al.* Multiple heteroatom substitution to graphene nanoribbon. *Sci. Adv.* **4**, 7181 (2018).
71. Urban, C. Structural and chemical effects of charge transfer across metal organic interfaces. (Universidad Autónoma de Madrid, 2012).

72. Rodríguez Fernández, J. Donor and acceptor molecules on metal surfaces: supramolecular self-assembly, metal-organic coordination networks, and charge-transfer complexes. (Universidad Autónoma de Madrid, 2014).
73. Cirera, B. On-Surface Design of Lanthanide Based Nanoarchitectures. (Universidad Autónoma de Madrid, 2017).
74. Martín Jiménez, A. Electronic and optical properties at the nanoscale studied by STM. (Universidad Autónoma de Madrid, 2018).
75. Kolasinski, K. W. *Surface Science: Foundations of Catalysis and Nanoscience*. (John Wiley & Sons, 2012).
76. Giessibl, F. J. The qPlus sensor, a powerful core for the atomic force microscope. *Rev. Sci. Instrum.* **90**, 011101 (2019).
77. Seh, Z. W. *et al.* Combining theory and experiment in electrocatalysis: Insights into materials design. *Science* **355**, 4998 (2017).
78. Gust, D., Moore, T. A. & Moore, A. L. Solar Fuels via Artificial Photosynthesis. *Acc. Chem. Res.* **42**, 1890–1898 (2009).
79. Berg, J. M., Tymoczko, J. L. & Stryer, L. *Biochemistry, Fifth Edition*. (W.H. Freeman, 2002).
80. Alfaifi, B., Ullah, H., Alfaifi, S., Tahir, A. & Mallick, T. Photoelectrochemical solar water splitting: From basic principles to advanced devices. *Veruscript Funct. Nanomater.* **2**, BDJOC3 (2018).
81. Galan-Mascaros, J. R. Photoelectrochemical solar fuels from carbon dioxide, water and sunlight. *Catal. Sci. Technol.* **10**, 1967–1974 (2020).
82. Viswanathan, V., Hansen, H. A., Rossmeisl, J. & Nørskov, J. K. Universality in Oxygen Reduction Electrocatalysis on Metal Surfaces. *ACS Catal.* **2**, 1654–1660 (2012).
83. Vojvodic, A. & Nørskov, J. K. New design paradigm for heterogeneous catalysts. *Natl. Sci. Rev.* **2**, 140–143 (2015).
84. Centi, G. & Perathoner, S. Opportunities and prospects in the chemical recycling of carbon dioxide to fuels. *Catal. Today* **148**, 191–205 (2009).
85. Olah, G. A., Goeppert, A. & Prakash, G. K. S. Chemical Recycling of Carbon Dioxide to Methanol and Dimethyl Ether: From Greenhouse Gas to Renewable,

Environmentally Carbon Neutral Fuels and Synthetic Hydrocarbons. *J. Org. Chem.* **74**, 487–498 (2009).

86. Morales-Guio, C. G., Liardet, L. & Hu, X. Oxidatively Electrodeposited Thin-Film Transition Metal (Oxy)hydroxides as Oxygen Evolution Catalysts. *J. Am. Chem. Soc.* **138**, 8946–8957 (2016).
87. Over, H. Atomic-Scale Structure and Catalytic Reactivity of the RuO2(110) Surface. *Science* **287**, 1474–1476 (2000).
88. R. Rao, R. *et al.* Towards identifying the active sites on RuO2 (110) in catalyzing oxygen evolution. *Energy Environ. Sci.* **10**, 2626–2637 (2017).
89. Pfeifer, V. *et al.* Reactive oxygen species in iridium-based OER catalysts. *Chem. Sci.* **7**, 6791–6795 (2016).
90. Nguyen, T.-T. H., Lee, J., Bae, J. & Lim, B. Binary FeCo Oxyhydroxide Nanosheets as Highly Efficient Bifunctional Electrocatalysts for Overall Water Splitting. *Chem. – Eur. J.* **24**, 4724–4728 (2018).
91. de Araújo, M. A., Coelho, D., Mascaro, L. H. & Pereira, E. C. The iron oxyhydroxide role in the mediation of charge transfer for water splitting using bismuth vanadate photoanodes. *J. Solid State Electrochem.* **22**, 1539–1548 (2018).
92. McCrory, C. C. L., Jung, S., Peters, J. C. & Jaramillo, T. F. Benchmarking Heterogeneous Electrocatalysts for the Oxygen Evolution Reaction. *J. Am. Chem. Soc.* **135**, 16977–16987 (2013).
93. Hapke, M. & Hilt, G. *Cobalt Catalysis in Organic Synthesis: Methods and Reactions*. (Wiley, 2019).
94. Kandalkar, S. G., Gunjakar, J. L. & Lokhande, C. D. Preparation of cobalt oxide thin films and its use in supercapacitor application. *Appl. Surf. Sci.* **254**, 5540–5544 (2008).
95. Kong, F.-C., Li, Y.-F., Shang, C. & Liu, Z.-P. Stability and Phase Transition of Cobalt Oxide Phases by Machine Learning Global Potential Energy Surface. *J. Phys. Chem. C* **123**, 17539–17547 (2019).
96. Chen, J., Wu, X. & Selloni, A. Electronic structure and bonding properties of cobalt oxide in the spinel structure. *Phys. Rev. B* **83**, 245204 (2011).

97. Meyer, W. *et al.* Coexistence of Rocksalt and Wurtzite Structure in Nanosized CoO Films. *Phys. Rev. Lett.* **101**, 016103 (2008).
98. Motohashi, T. *et al.* Synthesis and Properties of CoO2, the x = 0 End Member of the LixCoO2 and NaxCoO2 Systems. *Chem. Mater.* **19**, 5063–5066 (2007).
99. Lamirand, A. D. *et al.* Robust perpendicular exchange coupling in an ultrathin CoO/PtFe double layer: Strain and spin orientation. *Phys. Rev. B* **88**, 140401 (2013).
100. Fester, J., Walton, A., Li, Z. & Lauritsen, J. V. Gold-supported two-dimensional cobalt oxyhydroxide (CoOOH) and multilayer cobalt oxide islands. *Phys. Chem. Chem. Phys.* **19**, 2425–2433 (2017).
101. Fester, J., Sun, Z., Rodríguez-Fernández, J., Walton, A. & Lauritsen, J. V. Phase Transitions of Cobalt Oxide Bilayers on Au(111) and Pt(111): The Role of Edge Sites and Substrate Interactions. *J. Phys. Chem. B* **122**, 561–571 (2018).
102. Garces, L. J., Hincapie, B., Zerger, R. & Suib, S. L. The Effect of Temperature and Support on the Reduction of Cobalt Oxide: An in Situ X-ray Diffraction Study. *J. Phys. Chem. C* **119**, 5484–5490 (2015).
103. Walton, A. S. *et al.* Interface Controlled Oxidation States in Layered Cobalt Oxide Nanoislands on Gold. *ACS Nano* **9**, 2445–2453 (2015).
104. Borod'ko, Yu. G., Vetchinkin, S. I., Zimont, S. L., Ivleva, I. N. & Shul'ga, Yu. M. Nature of satellites in x-ray photoelectron spectra XPS of paramagnetic cobalt (II) compounds. *Chem. Phys. Lett.* **42**, 264–267 (1976).
105. Schmid, S., Hausbrand, R. & Jaegermann, W. Cobalt oxide thin film low pressure metal-organic chemical vapor deposition. *Thin Solid Films* **567**, 8–13 (2014).
106. Fester, J. *et al.* Comparative Analysis of Cobalt Oxide Nanoisland Stability and Edge Structures on Three Related Noble Metal Surfaces: Au(111), Pt(111) and Ag(111). *Top. Catal.* **60**, 503–512 (2017).
107. Park, K.-W. & Kolpak, A. M. Understanding photocatalytic overall water splitting on CoO nanoparticles: Effects of facets, surface stoichiometry, and the CoO/water interface. *J. Catal.* **365**, 115–124 (2018).
108. Yeo, B. S. & Bell, A. T. Enhanced Activity of Gold-Supported Cobalt Oxide for the Electrochemical Evolution of Oxygen. *J. Am. Chem. Soc.* **133**, 5587–5593 (2011).

109. Lu, X., Ng, Y. H. & Zhao, C. Gold Nanoparticles Embedded within Mesoporous Cobalt Oxide Enhance Electrochemical Oxygen Evolution. *ChemSusChem* **7**, 82–86 (2014).
110. Merte, L. R. *et al.* Correlating STM contrast and atomic-scale structure by chemical modification: Vacancy dislocation loops on FeO/Pt(111). *Surf. Sci.* **603**, L15–L18 (2009).
111. Lauritsen, J. V. & Reichling, M. Atomic resolution non-contact atomic force microscopy of clean metal oxide surfaces. *J. Phys. Condens. Matter* **22**, 263001 (2010).
112. Khan, N. A. & Matranga, C. Nucleation and growth of Fe and FeO nanoparticles and films on Au(111). *Surf. Sci.* **602**, 932–942 (2008).
113. Shiotari, A. *et al.* Local Characterization of Ultrathin ZnO Layers on Ag(111) by Scanning Tunneling Microscopy and Atomic Force Microscopy. *J. Phys. Chem. C* **118**, 27428–27435 (2014).
114. Diaye, A. T., Coraux, J., Plasa, T. N., Busse, C. & Michely, T. Structure of epitaxial graphene on Ir(111). *New J. Phys.* **10**, 043033 (2008).
115. Li, M. & Altman, E. I. Cluster-size dependent phase transition of Co oxides on Au(111). *Surf. Sci.* **619**, L6–L10 (2014).
116. Pletikosić, I. *et al.* Dirac Cones and Minigaps for Graphene on Ir(111). *Phys. Rev. Lett.* **102**, 056808 (2009).
117. Stradi, D. *et al.* Electron localization in epitaxial graphene on Ru(0001) determined by moiré corrugation. *Phys. Rev. B* **85**, 121404 (2012).
118. van der Heijden, N. J. *et al.* Characteristic Contrast in $\Delta f_{\min}$ Maps of Organic Molecules Using Atomic Force Microscopy. *ACS Nano* **10**, 8517–8525 (2016).
119. van der Heijden, N. J. *et al.* Recognizing nitrogen dopant atoms in graphene using atomic force microscopy. *Phys. Rev. B* **93**, 245430 (2016).
120. Schwarz, M. *et al.* Corrugation in the Weakly Interacting Hexagonal-BN/Cu(111) System: Structure Determination by Combining Noncontact Atomic Force Microscopy and X-ray Standing Waves. *ACS Nano* **11**, 9151–9161 (2017).
121. Krane, N., Lotze, C. & Franke, K. J. Moiré structure of MoS2 on Au(111): Local structural and electronic properties. *Surf. Sci.* **678**, 136–142 (2018).

122. Shin, H.-J. *et al.* State-selective dissociation of a single water molecule on an ultrathin MgO film. *Nat. Mater.* **9**, 442–447 (2010).
123. Zhang, J., Liu, J., Huang, J. L., Kim, P. & Lieber, C. M. Creation of Nanocrystals Through a Solid-Solid Phase Transition Induced by an STM Tip. *Science* **274**, 757–760 (1996).
124. Setvín, M., Wagner, M., Schmid, M., S. Parkinson, G. & Diebold, U. Surface point defects on bulk oxides: atomically-resolved scanning probe microscopy. *Chem. Soc. Rev.* **46**, 1772–1784 (2017).
125. Wang, Z. *et al.* Surface-Limited Superconducting Phase Transition on 1T-TaS2. *ACS Nano* **12**, 12619–12628 (2018).
126. Stroscio, J. A. & Eigler, D. M. Atomic and Molecular Manipulation with the Scanning Tunneling Microscope. *Science* **254**, 1319–1326 (1991).
127. Martel, R., Avouris, P. & Lyo, I.-W. Molecularly Adsorbed Oxygen Species on Si(111)-(7×7): STM-Induced Dissociative Attachment Studies. *Science* **272**, 385–388 (1996).
128. Fester, J. *et al.* Edge reactivity and water-assisted dissociation on cobalt oxide nanoislands. *Nat. Commun.* **8**, 1–8 (2017).
129. Fester, J. *et al.* The Structure of the Cobalt Oxide/Au Catalyst Interface in Electrochemical Water Splitting. *Angew. Chem.* **130**, 12069–12073 (2018).
130. Zhao, D. *et al.* Atomic site electrocatalysts for water splitting, oxygen reduction and selective oxidation. *Chem. Soc. Rev.* **49**, 2215–2264 (2020).
131. Merte, L. R. *et al.* Water-Mediated Proton Hopping on an Iron Oxide Surface. *Science* **336**, 889–893 (2012).
132. Michaelides, A., Alavi, A. & King, D. A. Different Surface Chemistries of Water on Ru{0001}: From Monomer Adsorption to Partially Dissociated Bilayers. *J. Am. Chem. Soc.* **125**, 2746–2755 (2003).
133. Andersson, K. *et al.* Autocatalytic Water Dissociation on Cu(110) at Near Ambient Conditions. *J. Am. Chem. Soc.* **130**, 2793–2797 (2008).
134. Sánchez-Grande, A. *et al.* On-Surface Synthesis of Ethynylene-Bridged Anthracene Polymers. *Angew. Chem. Int. Ed.* **58**, 6559–6563 (2019).

135. Sánchez-Grande, A. *et al.* Diradical Organic One-Dimensional Polymers Synthesized on a Metallic Surface. *Angew. Chem. Int. Ed.* **n/a**,.
136. Roncali, J. Synthetic Principles for Bandgap Control in Linear π-Conjugated Systems. *Chem. Rev.* **97**, 173–206 (1997).
137. Kertesz, M., Choi, C. H. & Yang, S. Conjugated Polymers and Aromaticity. *Chem. Rev.* **105**, 3448–3481 (2005).
138. Longuet-Higgins, H. C. & Salem, L. The alternation of bond lengths in long conjugated chain molecules. *Proc. R. Soc. Lond. Ser. Math. Phys. Sci.* **251**, 172–185 (1959).
139. Brédas, J. L. Relationship between band gap and bond length alternation in organic conjugated polymers. *J. Chem. Phys.* **82**, 3808–3811 (1985).
140. Roncali, J. Molecular Engineering of the Band Gap of π-Conjugated Systems: Facing Technological Applications. *Macromol. Rapid Commun.* **28**, 1761–1775 (2007).
141. Chiang, C. K. *et al.* Electrical Conductivity in Doped Polyacetylene. *Phys. Rev. Lett.* **39**, 1098–1101 (1977).
142. Correa, D., Medeiros, E., Oliveira, J., Paterno, L. & Mattoso, L. Nanostructured Conjugated Polymers in Chemical Sensors: Synthesis, Properties and Applications. *J. Nanosci. Nanotechnol.* **14**, (2014).
143. Méndez, J., Francisca López, M. & A. Martín-Gago, J. On-surface synthesis of cyclic organic molecules. *Chem. Soc. Rev.* **40**, 4578–4590 (2011).
144. Shen, Q., Gao, H.-Y. & Fuchs, H. Frontiers of on-surface synthesis: From principles to applications. *Nano Today* **13**, 77–96 (2017).
145. Wang, S. *et al.* On-surface synthesis and characterization of individual polyacetylene chains. *Nat. Chem.* **11**, 924–930 (2019).
146. Mondal, R., Tönshoff, C., Khon, D., Neckers, D. C. & Bettinger, H. F. Synthesis, Stability, and Photochemistry of Pentacene, Hexacene, and Heptacene: A Matrix Isolation Study. *J. Am. Chem. Soc.* **131**, 14281–14289 (2009).
147. Shen, B., Tatchen, J., Sanchez-Garcia, E. & Bettinger, H. F. Evolution of the Optical Gap in the Acene Series: Undecacene. *Angew. Chem. Int. Ed.* **57**, 10506–10509 (2018).

148. Houk, K. N., Lee, P. S. & Nendel, M. Polyacene and Cyclacene Geometries and Electronic Structures: Bond Equalization, Vanishing Band Gaps, and Triplet Ground States Contrast with Polyacetylene. *J. Org. Chem.* **66**, 5517–5521 (2001).
149. Moscardó, F. & San-Fabián, E. On the existence of a spin-polarized state in the n-periacene molecules. *Chem. Phys. Lett.* **480**, 26–30 (2009).
150. Mizukami, W., Kurashige, Y. & Yanai, T. More π Electrons Make a Difference: Emergence of Many Radicals on Graphene Nanoribbons Studied by *Ab Initio* DMRG Theory. *J. Chem. Theory Comput.* **9**, 401–407 (2013).
151. dos Santos, M. C. Electronic properties of acenes: Oligomer to polymer structure. *Phys. Rev. B* **74**, 045426 (2006).
152. Bendikov, M. *et al.* Oligoacenes: Theoretical Prediction of Open-Shell Singlet Diradical Ground States. *J. Am. Chem. Soc.* **126**, 7416–7417 (2004).
153. Anthony, J. E. The Larger Acenes: Versatile Organic Semiconductors. *Angew. Chem. Int. Ed.* **47**, 452–483 (2008).
154. Ajayakumar, M. R. *et al.* Toward Full Zigzag-Edged Nanographenes: peri-Tetracene and Its Corresponding Circumanthracene. *J. Am. Chem. Soc.* **140**, 6240–6244 (2018).
155. Urgel, J. I. *et al.* On-Surface Synthesis of Heptacene Organometallic Complexes. *J. Am. Chem. Soc.* **139**, 11658–11661 (2017).
156. Zuzak, R. *et al.* Higher Acenes by On-Surface Dehydrogenation: From Heptacene to Undecacene. *Angew. Chem. Int. Ed.* **57**, 10500–10505 (2018).
157. Urgel, J. I. *et al.* On-surface light-induced generation of higher acenes and elucidation of their open-shell character. *Nat. Commun.* **10**, 861 (2019).
158. Eisenhut, F. *et al.* Dodecacene Generated on Surface: Reopening of the Energy Gap. *ACS Nano* **14**, 1011–1017 (2020).
159. Das, S. & Wu, J. Polycyclic Hydrocarbons with an Open-Shell Ground State. *Phys. Sci. Rev.* **2**, (2017).
160. Jiang, D., Sumpter, B. G. & Dai, S. First principles study of magnetism in nanographenes. *J. Chem. Phys.* **127**, 124703 (2007).
161. Jiang, D. & Dai, S. Electronic Ground State of Higher Acenes. *J. Phys. Chem. A* **112**, 332–335 (2008).

162. Konishi, A. & Kubo, T. Benzenoid Quinodimethanes. in *Physical Organic Chemistry of Quinodimethanes* (eds. Tobe, Y. & Kubo, T.) 69–105 (Springer International Publishing, 2018).
163. Solà, M. Forty years of Clar's aromatic π-sextet rule. *Front. Chem.* **1**, (2013).
164. Yeh, C.-N. & Chai, J.-D. Role of Kekulé and Non-Kekulé Structures in the Radical Character of Alternant Polycyclic Aromatic Hydrocarbons: A TAO-DFT Study. *Sci. Rep.* **6**, 30562 (2016).
165. Shimizu, A. *et al.* Theoretical consideration of singlet open-shell character of polyperiacenes using Clar's aromatic sextet valence bond model and quantum chemical calculations. *AIP Conf. Proc.* **1504**, 399–405 (2012).
166. Jiang, D. & Dai, S. Circumacenes versus periacenes: HOMO–LUMO gap and transition from nonmagnetic to magnetic ground state with size. *Chem. Phys. Lett.* **466**, 72–75 (2008).
167. Ni, Y. *et al.* A Peri-tetracene Diradicaloid: Synthesis and Properties. *Angew. Chem. Int. Ed.* **57**, 9697–9701 (2018).
168. Mishra, S. *et al.* Tailoring Bond Topologies in Open-Shell Graphene Nanostructures. *ACS Nano* **12**, 11917–11927 (2018).
169. Plasser, F. *et al.* The Multiradical Character of One- and Two-Dimensional Graphene Nanoribbons. *Angew. Chem. Int. Ed.* **52**, 2581–2584 (2013).
170. Cai, J. *et al.* Atomically precise bottom-up fabrication of graphene nanoribbons. *Nature* **466**, 470–473 (2010).
171. Ruffieux, P. *et al.* On-surface synthesis of graphene nanoribbons with zigzag edge topology. *Nature* **531**, 489–492 (2016).
172. Weigelt, S. *et al.* Surface Synthesis of 2D Branched Polymer Nanostructures. *Angew. Chem. Int. Ed.* **47**, 4406–4410 (2008).
173. Moreno, C. *et al.* Bottom-up synthesis of multifunctional nanoporous graphene. *Science* **360**, 199–203 (2018).
174. Simonov, K. A. *et al.* From Graphene Nanoribbons on Cu(111) to Nanographene on Cu(110): Critical Role of Substrate Structure in the Bottom-Up Fabrication Strategy. *ACS Nano* **9**, 8997–9011 (2015).

175. Lafferentz, L. *et al.* Controlling on-surface polymerization by hierarchical and substrate-directed growth. *Nat. Chem.* **4**, 215–220 (2012).
176. Judd, C. J., Haddow, S. L., Champness, N. R. & Saywell, A. Ullmann Coupling Reactions on Ag(111) and Ag(110); Substrate Influence on the Formation of Covalently Coupled Products and Intermediate Metal-Organic Structures. *Sci. Rep.* **7**, 14541 (2017).
177. Lewis, E. A., Murphy, C. J., Liriano, M. L. & Sykes, E. C. H. Atomic-scale insight into the formation, mobility and reaction of Ullmann coupling intermediates. *Chem. Commun.* **50**, 1006–1008 (2013).
178. Cai, J. *et al.* Graphene nanoribbon heterojunctions. *Nat. Nanotechnol.* **9**, 896–900 (2014).
179. Zhang, H. *et al.* On-Surface Synthesis of Rylene-Type Graphene Nanoribbons. *J. Am. Chem. Soc.* **137**, 4022–4025 (2015).
180. Chen, M. *et al.* Combined Photoemission and Scanning Tunneling Microscopy Study of the Surface-Assisted Ullmann Coupling Reaction. *J. Phys. Chem. C* **118**, 6820–6830 (2014).
181. Pham, T. A. *et al.* Comparing Ullmann Coupling on Noble Metal Surfaces: On-Surface Polymerization of 1,3,6,8-Tetrabromopyrene on Cu(111) and Au(111). *Chem. – Eur. J.* **22**, 5937–5944 (2016).
182. Eichhorn, J. *et al.* On-Surface Ullmann Coupling: The Influence of Kinetic Reaction Parameters on the Morphology and Quality of Covalent Networks. *ACS Nano* **8**, 7880–7889 (2014).
183. Sun, K. *et al.* Synthesis of Regioisomeric Graphene Nanoribbon Junctions via Heteroprecursors. *J. Phys. Chem. C* **123**, 17632–17638 (2019).
184. Chung, K.-H. *et al.* Electronic structures of one-dimensional metal–molecule hybrid chains studied using scanning tunneling microscopy and density functional theory. *Phys. Chem. Chem. Phys.* **14**, 7304 (2012).
185. Di Giovannantonio, M. *et al.* Insight into Organometallic Intermediate and Its Evolution to Covalent Bonding in Surface-Confined Ullmann Polymerization. *ACS Nano* **7**, 8190–8198 (2013).

186. Sun, Q., Cai, L., Ma, H., Yuan, C. & Xu, W. The stereoselective synthesis of dienes through dehalogenative homocoupling of terminal alkenyl bromides on Cu(110). *Chem. Commun.* **52**, 6009–6012 (2016).
187. Sun, Q. *et al.* On-Surface Formation of Cumulene by Dehalogenative Homocoupling of Alkenyl gem-Dibromides. *Angew. Chem. Int. Ed.* **56**, 12165–12169 (2017).
188. Björk, J., Hanke, F. & Stafström, S. Mechanisms of Halogen-Based Covalent Self-Assembly on Metal Surfaces. *J. Am. Chem. Soc.* **135**, 5768–5775 (2013).
189. de Oteyza, D. G. *et al.* Direct Imaging of Covalent Bond Structure in Single-Molecule Chemical Reactions. *Science* **340**, 1434–1437 (2013).
190. Sun, Q. *et al.* Direct Formation of C–C Triple-Bonded Structural Motifs by On-Surface Dehalogenative Homocouplings of Tribromomethyl-Substituted Arenes. *Angew. Chem. Int. Ed.* **57**, 4035–4038 (2018).
191. Kawai, S. *et al.* Diacetylene Linked Anthracene Oligomers Synthesized by One-Shot Homocoupling of Trimethylsilyl on Cu(111). *ACS Nano* **12**, 8791–8797 (2018).
192. Hapala, P. *et al.* Mechanism of high-resolution STM/AFM imaging with functionalized tips. *Phys. Rev. B* **90**, 085421 (2014).
193. Piquero-Zulaica, I. *et al.* Electronic Structure Tunability by Periodic *meta* -Ligand Spacing in One-Dimensional Organic Semiconductors. *ACS Nano* **12**, 10537–10544 (2018).
194. Merino-Díez, N. *et al.* Width-Dependent Band Gap in Armchair Graphene Nanoribbons Reveals Fermi Level Pinning on Au(111). *ACS Nano* **11**, 11661–11668 (2017).
195. Amy, F., Chan, C. & Kahn, A. Polarization at the gold/pentacene interface. *Org. Electron.* **6**, 85–91 (2005).
196. Neaton, J. B., Hybertsen, M. S. & Louie, S. G. Renormalization of Molecular Electronic Levels at Metal-Molecule Interfaces. *Phys. Rev. Lett.* **97**, 216405 (2006).
197. Cohen, A. J., Mori-Sánchez, P. & Yang, W. Insights into Current Limitations of Density Functional Theory. *Science* **321**, 792–794 (2008).
198. Yamanaka, S., Okumura, M., Nakano, M. & Yamaguchi, K. EHF theory of chemical reactions Part 4. UNO CASSCF, UNO CASPT2 and R(U)HF coupled-cluster (CC) wavefunctions. *J. Mol. Struct. THEOCHEM* **310**, 205–218 (1994).

199. Yamaguchi, K. *et al.* Analytical and ab initio studies of effective exchange interactions, polyradical character, unpaired electron density, and information entropy in radical clusters (R)N: Allyl radical cluster (N=2–10) and hydrogen radical cluster (N=50). *Int. J. Quantum Chem.* **90**, 370–385 (2002).
200. Urgel, J. I. *et al.* On-Surface Synthesis of Cumulene-Containing Polymers via Two-Step Dehalogenative Homocoupling of Dibromomethylene-Functionalized Tribenzoazulene. *Angew. Chem.* **132**, 13383–13389 (2020).
201. Moll, N., Gross, L., Mohn, F., Curioni, A. & Meyer, G. The mechanisms underlying the enhanced resolution of atomic force microscopy with functionalized tips. *New J. Phys.* **12**, 125020 (2010).
202. Jelínek, P. High resolution SPM imaging of organic molecules with functionalized tips. *J. Phys. Condens. Matter* **29**, 343002 (2017).
203. Garcia-Lastra, J. M., Rostgaard, C., Rubio, A. & Thygesen, K. S. Polarization-induced renormalization of molecular levels at metallic and semiconducting surfaces. *Phys. Rev. B* **80**, 245427 (2009).
204. Rizzo, D. J. *et al.* Topological band engineering of graphene nanoribbons. *Nature* **560**, 204–208 (2018).
205. Karpfen, A. Ab initio studies on polymers. IV. Polydiacetylenes. *J. Phys. C Solid State Phys.* **13**, 5673–5689 (1980).
206. Hernandez, V., Castiglioni, C., Del Zoppo, M. & Zerbi, G. Confinement potential and pi-electron delocalization in polyconjugated organic materials. *Phys. Rev. B* **50**, 9815–9823 (1994).
207. Lawrence, J. *et al.* Probing the Magnetism of Topological End States in 5-Armchair Graphene Nanoribbons. *ACS Nano* **14**, 4499–4508 (2020).
208. Alcón, I., Viñes, F., Moreira, I. de P. R. & Bromley, S. T. Existence of multi-radical and closed-shell semiconducting states in post-graphene organic Dirac materials. *Nat. Commun.* **8**, (2017).
209. Rogers, C. *et al.* Closing the Nanographene Gap: Surface-Assisted Synthesis of Peripentacene from 6,6′-Bipentacene Precursors. *Angew. Chem. Int. Ed.* **54**, 15143–15146 (2015).

210. Januszewski, J. A. & Tykwinski, R. R. Synthesis and properties of long [n]cumulenes (n ≥ 5). *Chem. Soc. Rev.* **43**, 3184–3203 (2014).
211. Garner, M. H., Bro-Jørgensen, W., Pedersen, P. D. & Solomon, G. C. Reverse Bond-Length Alternation in Cumulenes: Candidates for Increasing Electronic Transmission with Length. *J. Phys. Chem. C* **122**, 26777–26789 (2018).
212. Wendinger, D. & Tykwinski, R. R. Odd [n]Cumulenes (n = 3, 5, 7, 9): Synthesis, Characterization, and Reactivity. *Acc. Chem. Res.* **50**, 1468–1479 (2017).
213. Kondo, J. Resistance Minimum in Dilute Magnetic Alloys. *Prog. Theor. Phys.* **32**, 37–49 (1964).
214. Mora, C., Moca, C. P., von Delft, J. & Zaránd, G. Fermi-liquid theory for the single-impurity Anderson model. *Phys. Rev. B* **92**, 075120 (2015).
215. Nagaoka, K., Jamneala, T., Grobis, M. & Crommie, M. F. Temperature Dependence of a Single Kondo Impurity. *Phys. Rev. Lett.* **88**, 077205 (2002).
216. Zhang, Y. *et al.* Temperature and magnetic field dependence of a Kondo system in the weak coupling regime. *Nat. Commun.* **4**, 2110 (2013).
217. Gruber, M., Weismann, A. & Berndt, R. The Kondo resonance line shape in scanning tunnelling spectroscopy: instrumental aspects. *J. Phys. Condens. Matter* **30**, 424001 (2018).
218. Mishra, S. *et al.* Topological Defect-Induced Magnetism in a Nanographene. *J. Am. Chem. Soc.* **142**, 1147–1152 (2020).
219. Ternes, M., Heinrich, A. J. & Schneider, W.-D. Spectroscopic manifestations of the Kondo effect on single adatoms. *J. Phys. Condens. Matter* **21**, 053001 (2008).
220. Ortiz, R. *et al.* Exchange Rules for Diradical π-Conjugated Hydrocarbons. *Nano Lett.* **19**, 5991–5997 (2019).
221. Mishra, S. *et al.* Topological frustration induces unconventional magnetism in a nanographene. *Nat. Nanotechnol.* **15**, 22–28 (2020).
222. Li, J. *et al.* Single spin localization and manipulation in graphene open-shell nanostructures. *Nat. Commun.* **10**, 200 (2019).
223. Patera, L. L. *et al.* Resolving the Unpaired-Electron Orbital Distribution in a Stable Organic Radical by Kondo Resonance Mapping. *Angew. Chem. Int. Ed.* **58**, 11063–11067 (2019).

224. Kurotobi, K., Kim, K. S., Noh, S. B., Kim, D. & Osuka, A. A Quadruply Azulene-Fused Porphyrin with Intense Near-IR Absorption and a Large Two-Photon Absorption Cross Section. *Angew. Chem. Int. Ed.* **45**, 3944–3947 (2006).
225. Das, S. & Wu, J. Toward Singlet–Triplet Bistable Nonalternant Kekulé Hydrocarbons: Azulene-to-Naphthalene Rearrangement. *Org. Lett.* **17**, 5854–5857 (2015).
226. Han, Y. *et al.* Formation of Azulene-Embedded Nanographene: Naphthalene to Azulene Rearrangement During the Scholl Reaction. *Angew. Chem. Int. Ed.* **59**, 9026–9031 (2020).
227. Liu, J. *et al.* Open-Shell Nonbenzenoid Nanographenes Containing Two Pairs of Pentagonal and Heptagonal Rings. *J. Am. Chem. Soc.* **141**, 12011–12020 (2019).
228. de la Torre, B. *et al.* Tailoring \pi-conjugation and vibrational modes to steer on-surface synthesis of pentalene-bridged ladder polymers. *ArXiv200404918 Cond-Mat* (2020).
229. Lee, J., Kalin, A. J., Yuan, T., Al-Hashimi, M. & Fang, L. Fully conjugated ladder polymers. *Chem. Sci.* **8**, 2503–2521 (2017).
230. Zeng, Z. *et al.* Pro-aromatic and anti-aromatic π-conjugated molecules: an irresistible wish to be diradicals. *Chem. Soc. Rev.* **44**, 6578–6596 (2015).
231. Frederickson, C. K., Rose, B. D. & Haley, M. M. Explorations of the Indenofluorenes and Expanded Quinoidal Analogues. *Acc. Chem. Res.* **50**, 977–987 (2017).
232. Di Giovannantonio, M. *et al.* On-Surface Synthesis of Indenofluorene Polymers by Oxidative Five-Membered Ring Formation. *J. Am. Chem. Soc.* **140**, 3532–3536 (2018).
233. Vineyard, G. H. Frequency factors and isotope effects in solid state rate processes. *J. Phys. Chem. Solids* **3**, 121–127 (1957).
234. Crim, F. F. Chemical dynamics of vibrationally excited molecules: Controlling reactions in gases and on surfaces. *Proc. Natl. Acad. Sci.* **105**, 12654–12661 (2008).
235. Guo, H. & Liu, K. Control of chemical reactivity by transition-state and beyond. *Chem. Sci.* **7**, 3992–4003 (2016).
236. Glidewell, C. & Lloyd, D. Mndo study of bond orders in some conjugated BI- and tri-cyclic hydrocarbons. *Tetrahedron* **40**, 4455–4472 (1984).

237. El Bakouri, O., Poater, J., Feixas, F. & Solà, M. Exploring the validity of the Glidewell–Lloyd extension of Clar's π-sextet rule: assessment from polycyclic conjugated hydrocarbons. *Theor. Chem. Acc.* **135**, 205 (2016).
238. Gross, L. *et al.* Bond-Order Discrimination by Atomic Force Microscopy. *Science* **337**, 1326–1329 (2012).